

111-447
20609
P111

NASA Technical Memorandum

NASA TM - 103539

ANALYSIS OF LIGHTNING FIELD CHANGES PRODUCED BY FLORIDA THUNDERSTORMS

By William J. Koshak

Space Science Laboratory
Science and Engineering Directorate

April 1991

(NASA-TM-103539) ANALYSIS OF LIGHTNING
FIELD CHANGES PRODUCED BY FLORIDA
THUNDERSTORMS (NASA) 171 P CSCL 04B

N91-25555

Unclas
G3/47 0020609



National Aeronautics and
Space Administration

George C. Marshall Space Flight Center



Report Documentation Page

1. Report No. NASA TM - 103539		2. Government Accession No.		3. Recipient's Catalog No.	
4. Title and Subtitle Analysis of Lightning Field Changes Produced by Florida Thunderstorms				5. Report Date April 1991	
				6. Performing Organization Code ES43	
7. Author(s) William John Koshak				8. Performing Organization Report No.	
				10. Work Unit No.	
9. Performing Organization Name and Address George C. Marshall Space Flight Center Marshall Space Flight Center, AL 35812				11. Contract or Grant No.	
				13. Type of Report and Period Covered Technical Memorandum	
12. Sponsoring Agency Name and Address National Aeronautics and Space Administration Washington, D.C. 20546				14. Sponsoring Agency Code	
				15. Supplementary Notes Prepared by Space Science Laboratory, Science and Engineering Directorate.	
16. Abstract <p>A new method is introduced for inferring the charges deposited in a lightning flash. Previous nonlinear least-squares methods have used simple point charge (Q) and point dipole (P) models to describe ground-based observations of lightning-caused field changes (ΔE's). In the new approach, the ΔE's are described by a more general volume charge distribution that is defined on a large cartesian grid system centered above the measuring network. We show that a linear system of equations can be used to relate the ΔE's at the ground to the values of charge on this grid. With this approach, it is possible to apply more general physical constraints to the charge solutions, and it is possible to access the information content of the ΔE data. Computer-simulated ΔE inversions show that the location and symmetry of the charge retrievals are usually consistent with the known test sources. Analyses of three natural lightning events show that the linear method provides source distributions that are in reasonable agreement with Q- and P-model results.</p>					
17. Key Words (Suggested by Author(s)) Lightning, Charge Inversions			18. Distribution Statement Unclassified--Unlimited		
19. Security Classif. (of this report) Unclassified		20. Security Classif. (of this page) Unclassified		21. No. of pages 171	22. Price NTIS

ACKNOWLEDGMENTS

Many thanks are given to Prof. E. Philip Krider and Prof. Sean Twomey of the University of Arizona for their guidance and support during this research. I am also indebted to computer specialists: Mr. Lincoln Thomas and Mr. Michael Leuthold for their help with computer graphics, and to Mr. William Jafferis, the NASA Kennedy Space Center, and the USAF Cape Canaveral Air Force Station for providing the field mill data used in this study. For help in the editing of the final manuscript I am thankful to Tauna Moorehead, Shelby Morris, and Susan Burrer.

TABLE OF CONTENTS

	Page
1. INTRODUCTION	1
2. MEASUREMENTS	8
2.1 Electric field measurements	8
2.2 Computation of lightning-caused field changes	9
2.2.1 Identifying lightning in field mill data	10
2.2.2 Obtaining initial and final fields	11
2.2.3 The time-varying background field	11
2.2.4 L- and F-changes	12
2.2.5 Detection of poor field mill data	13
2.2.6 Interactive algorithm	14
2.3 Errors	15
3. FIELD CHANGE ANALYSES	17
3.1 Nonlinear least-squares optimization	17
3.1.1 The Marquardt algorithm	18
3.1.2 The Q- and P-models	20
3.1.3 Limitations of model fits	21
3.2 Fredholm integral formulation	23
3.2.1 Gradient-constrained linear inversion algorithm	29
3.2.2 Twomey-Chahine algorithm	32
3.2.3 Method of steepest descent	33
3.2.4 Landweber iterations	35
4. EXTERNAL CONSTRAINTS	37
4.1 The need for external constraints	37
4.2 The Marquardt algorithm as a constrained linear inversion result	41
4.3 Constraints used in the method of steepest descent	44
4.3.1 Scaling constraint	44
4.3.2 Maximum charge density constraint	46
4.3.3 Smoothing constraint	47
4.3.4 Focusing constraint	48
4.3.5 Conservation of charge constraint	49
4.3.6 Other constraints	50

TABLE OF CONTENTS (CONCLUDED)

	Page
5. SOLUTION ERROR	52
5.1 Information content	53
5.1.1 The eigenanalysis test for independence	53
5.1.2 Eigenanalyses of the KSC field mill network	58
5.2 Simulated lightning sources over the network	62
5.3 Simulated point sources off the network	67
6. STORM ANALYSIS	69
6.1 Flashing rate histograms	69
6.2 Q- and P-model results	70
6.2.1 Storm on July 5, 1978	73
6.2.2 Storm on July 6, 1978	74
6.2.3 Storm on July 11, 1978	75
6.2.4 Storm on July 17, 1978	75
6.2.5 Storm on July 19, 1978	76
6.2.6 Storm on July 31, 1978	76
6.2.7 Storms on July 14 and August 13, 1978	77
6.3 Linear method results and comparisons	77
6.4 Future work	79
7. SUMMARY	83
APPENDIX: UNIQUENESS OF THE SOLUTION LYING IN THE ROW SPACE OF K	86
REFERENCES	88

LIST OF ILLUSTRATIONS

Figure	Page
2.1 Map of the NASA Kennedy Space Center and Cape Canaveral Air Force Station. Numbers indicate the 25 electric field mills operated in 1978	92
2.2 The electric field mill sensor used to measure the vertical component of the atmospheric electric field	93
2.3 An example of the digital field mill data from three mills on July 6, 1978	94
2.4 A more time-resolved graph of a field change shown previously in Figure 2.3 that contains a final change structure	95
2.5 Another example of a (more complicated) final change structure	96
3.1 Illustration of the geometry associated with the Q- and P-models	97
3.2 Geometry associated with the Fredholm integral formulation	98
3.3 Kernel function (times $2\pi\epsilon_0$) versus distance from field mill, for various altitudes .	99
3.4 Kernel function (times $2\pi\epsilon_0$) versus altitude, for various distances from field mill .	100
3.5 Illustration of the method of steepest descent	101
5.1- 5.15 Linear method results derived for various known source geometries and locations	102
6.1 Flashing rate histograms for July 5 and July 6, 1978	132
6.2 Flashing rate histograms for July 11 and July 14, 1978	133
6.3 Flashing rate histograms for July 17 and July 19, 1978	134

LIST OF ILLUSTRATIONS (CONCLUDED)

Figure	Page
6.4 Flashing rate histograms for July 31 and August 13, 1978	135
6.5 Height vs. time, plan view, and cross section plots of Q- and P-solutions for July 5, 1978, storm	136
6.6 Height vs. time, plan view, and cross section plots of Q- and P-solutions for July 6, 1978, storm	138
6.7 Height vs. time, plan view, and cross section plots of Q- and P-solutions for July 11, 1978, storm	140
6.8 Height vs. time, plan view, and cross section plots of Q- and P-solutions for July 17, 1978, storm	142
6.9 Height vs. time, plan view, and cross section plots of Q- and P-solutions for July 19, 1978, storm	144
6.10 Height vs. time, plan view, and cross section plots of Q- and P-solutions for July 31, 1978, storm	146
6.11 Height vs. time and plan view plots of Q- and P-solutions for two distant storms on July 14 and August 13, 1978	148
6.12 Results of linear method for lightning event occurring at 201521.4 GMT on July 6, 1978	150
6.13 Results of linear method for lightning event occurring at 202210.4 GMT on July 6, 1978	152
6.14 Results of linear method for lightning event occurring at 201611.9 GMT on July 6, 1978	154

LIST OF TABLES

Table	Page
5.1 Information content of a centrally located grid system for various grid resolutions	156
5.2 Information content of a centrally located grid system for various grid dimensions	157
5.3 Information content of a small cubical grid system (dimension 10 km, resolution 1 km) for various distances from the measuring network	158
5.4 Information content for four different field mill networks	159
5.5 Summary of solution error for various lightning source geometries and locations ..	160
6.1 Statistics on the number of flashes from each storm and the number of optimum solutions they ultimately produce	161
6.2 Summary of the Q- and P-solutions derived using the Chi-square minimization procedure	162

TECHNICAL MEMORANDUM
ANALYSIS OF LIGHTNING FIELD CHANGES PRODUCED
BY FLORIDA THUNDERSTORMS

CHAPTER 1
INTRODUCTION

Thunderclouds produce electric fields at the ground that can approach several kilovolts per meter, and are usually directed upward. Pointed objects near the ground distort and intensify these fields, and ensuing corona currents lead to the formation of a space charge shielding layer. Because of this shielding layer, ground observations of the electric field no longer contain enough information about the details of the thundercloud charges aloft. Fortunately, a great deal can still be learned about the electrical structure of thunderclouds by analyzing ground-based measurements of the *changes* in the electric field that are caused by lightning. Since the space charges cannot rearrange quickly enough during a lightning event (typically 0.3 to 0.4 seconds), the effect of shielding can usually be ignored.

C.T.R. Wilson undertook the first systematic study of lightning field changes [Wilson, 1916]. He measured ΔE 's at various distances from thunderstorms and showed that distant cloud discharges produced field changes that were usually reversed in polarity from closer discharges. From these observations, Wilson [1920] deduced the classic bipolar model for thundercloud charges, i.e., positive charge at high altitudes and negative charge at lower altitudes [Wilson, 1929].

Unfortunately, Wilson's measurements were limited to a single station and could not provide a detailed picture of the charges that were involved in lightning. In order to obtain

more information about how lightning altered the cloud charge distribution, Workman and Holzer [1942], Workman, Holzer, and Pelsor [1942], Reynolds and Neill [1955], and later Krehbiel [1979] made multiple station measurements of electric field changes in New Mexico. Krehbiel [1981] has recently reviewed the measurement techniques, the methods of data analysis, and the results. These authors found that many flashes could be described by simple charge models, and the resulting solutions were interesting not only because they provided quantitative estimates of the lightning charge transfers, but also because they provided an estimate of the altitudes of the charges (and corresponding temperatures) and the charge locations relative to radar echoes. The New Mexico results showed that lightning charges were located at temperatures that were below freezing, a result that has been verified by more recent work [Barnard, 1951; Hacking, 1954; Tamura, 1958; Hatakeyama, 1958; Takeuti, 1966; Ogawa and Brook, 1969]. This result in turn has motivated several important laboratory experiments on the role of ice particles in cloud electrification processes [Workman and Reynolds, 1949; Reynolds, Brook, and Gourley, 1957; and more recently Caranti and Illingworth, 1980; Jayaratne, Hallet, and Saunders, 1980; Latham, 1981; Illingworth, 1985; Baker et al., 1987; and Saunders and Zhang, 1987].

In the early 1970's, the NASA Kennedy Space Center (KSC) installed a large network of electric field mills to identify atmospheric electrical hazards that might threaten the launches of spacecraft or ground operations. This network, located in the maritime tropical climate on the Florida peninsula, contained 21 ground-based sensors and covered a total area of approximately 15 x 25 km².

Jacobson and Krider [1976] used the KSC network to study thunderstorm fields and developed a nonlinear least-squares minimization procedure (that will be described in detail below), to analyze lightning field changes. They found that discharges to ground effectively deposit positive charge (or, equivalently, remove negative charge) at altitudes of 6 to 9 km where corresponding ambient air temperatures are between $-10\text{ }^{\circ}\text{C}$ and $-34\text{ }^{\circ}\text{C}$. Although these charge altitudes are somewhat higher than in New Mexico, the corresponding air temperatures were typical of other regions. Jacobson and Krider [1976] also found that a significant fraction of the discharges to ground produced field changes that were small or even reverse polarity within 3 km of the strike point. An analysis of these events showed that a small volume of positive charge, 0.4 to 5 C, was often neutralized at altitudes between 1 and 3 km, together with the main negative charge.

Maier and Krider [1986] analyzed KSC field mill data taken during the summer months of 1976-1978 that was similar to the data used by Jacobson and Krider [1976]. These authors used a computer algorithm to identify lightning and compute values of ΔE , rather than manual methods used by Jacobson and Krider [1976]. The results indicated that the negative charge centers remained at constant altitude throughout the life cycle of the thunderstorm. The mean charge altitude depended somewhat on the storm, but the values ranged from 6.9 km ($-14\text{ }^{\circ}\text{C}$) to 8.8 km ($-26\text{ }^{\circ}\text{C}$), with total charge transfers ranging from $11\text{ }^{\circ}\text{C}$ to $44\text{ }^{\circ}\text{C}$.

A few years later, Koshak and Krider [1989] developed an improved computer method for computing accurate field change values and extended the work of Maier and Krider [1986] to active thunderstorms. Koshak and Krider [1989] also analyzed intracloud lightning and showed that a typical cloud discharge produced moment changes of $113\text{ }^{\circ}\text{C km}$ to $343\text{ }^{\circ}\text{C km}$

and that high altitude cloud flashes were systematically larger than lower altitude flashes. Ground discharges in active storms were found to deposit charges at altitudes and ambient temperatures that were comparable to those in small storms, and the total charge values were also similar. Krider [1989] later pointed out that the apparent separation between the positive and negative charge centers depended on the storm size.

One of the more interesting results of Koshak and Krider [1989] is the high degree of symmetry in the directions of cloud discharges. High altitude cloud discharges effectively transported positive charge in a downward direction toward the negative charge region, while low altitude discharges transported charge in an upward direction. Cloud discharges that occurred at the same altitude as the negative charge region tended to transport positive charge in a horizontal direction. These results are consistent with the classic bipolar charge structure proposed by Wilson [1929] and with the extended tripolar structure that is reviewed in Williams [1989].

Although least-squares analyses of the KSC field mill data have greatly improved our knowledge of lightning charges, these studies have several limitations and inherent biases associated with them. First, the computer methods for detecting and computing lightning ΔE 's from field mill data are not perfect. Subsequent least-squares analyses of erroneous ΔE data can lead to nonphysical charge solutions. Second, since very small field change values have proportionately larger errors (see comments in Chapter 2 on digitization errors in KSC field data), only large lightning events have been analyzed, i.e., those that produce a $\Delta E \geq 1$ kV/m at three or more field mill sites. Hence, the solution statistics are biased because the smaller events have not been included. Finally, there are biases because complex lightning events can

not be described with the simple charge models used. More complicated charge models have not been used because a finite set of measurements do not, by themselves, provide enough information to uniquely describe complex events. With a normal uncertainty in the ΔE values, there will always be an uncertainty in the charge solutions. Even without measurement error, the nature of Coulomb's Law is such that there will always be an infinite number of charge distributions that will produce exactly the same set of field values. In order to determine a "correct" solution to an inherently non-unique problem, we will need to add extra physical constraints so that the number of our choices are reduced. Such constraints should be based on our knowledge about the physics of lightning and the thunderstorm environment.

In the following chapters, we will describe an interactive computer program that combines manual and automatic analysis techniques to improve lightning identification and the computation of ΔE values (regardless of their amplitude). This new program has been applied to eight Florida thunderstorms and the resulting sets of ΔE values have been analyzed using the standard least-squares approach and point charge (Q) and point dipole (P) models. To reduce biases from a ΔE threshold requirement, we have analyzed all flashes that produced a field change of 1 kV/m at two or more sites (rather than three or more sites as described above). Since we have analyzed the entire life cycle of each storm (some lasting 2 - 3 hours), and since the interactive program has allowed us to compute improved ΔE values and has given us confidence in reducing our ΔE -threshold requirement, we have obtained improved Q- and P-statistics over previous studies.

The inability to describe complex lightning events with simple charge models is a far more fundamental problem. Because of this, we have also developed an entirely different

approach for analyzing lightning field changes. This new method can be used to describe very complicated lightning charge distributions and provides an easier way of adding arbitrary external constraints to the solution process. Solutions are no longer the parameters of simple charge models, but are volume distributions of charge that are defined on a grid of finite dimension and resolution. In order to describe lightning events having a variety of locations, the grid is centered above the KSC network and has a large detection volume. In addition, our method provides a framework where we can use a standard eigenanalysis to determine the information content of the field change measurements, and assess the effects of measurement errors, network geometry, and solution grid geometry on the accuracy of the solution.

The chapters below are organized in the following way. All details of the KSC measuring network, examples of thunderstorm fields, and a discussion of the interactive ΔE program are provided in Chapter 2. In Chapter 3 we review the least-squares approach of Jacobson and Krider [1976] for analyzing ΔE 's, and describe in greater detail some limitations in the method. We next introduce our new analysis method by showing that we can describe field changes in terms of a linear system of equations. Various algorithms for solving this system will be discussed near the end of Chapter 3, and we will note that the most appropriate algorithm is the "method of steepest descent". This algorithm allows arbitrary external constraints to be added to the solution process and the importance of these constraints will be stressed in Chapter 4, where we give several examples.

As a check of our new method, we analyze the fields produced by known lightning sources in Chapter 5 and discuss solution errors. We show that a particular form of the method of steepest descent, a Landweber iteration, is most useful in obtaining accurate solutions. We

give a theoretical description of solution errors and we also explore the information content of the data using an eigenanalysis approach. In Chapter 6, we give all of our Q- and P-model results for eight Florida storms. We also analyze three lightning events from one of these storms using the Landweber iterative technique and then compare the results with the associated Q- and P-model results. Chapter 6 ends with some suggestions for future work, and Chapter 7 summarizes our results.

CHAPTER 2

MEASUREMENTS

This chapter describes our measurements of thunderstorm electric fields and a computer algorithm that has been used to determine the values of lightning-caused changes in these fields. The finite set of derived field changes will loosely be referred to as "measurements" in later chapters. The net errors in the field change values are important in determining the accuracy of our solutions (see Chapter 5 on solution error). Accordingly, this chapter also reviews various difficulties associated with computing accurate ΔE 's from the electric field data and concludes by giving reasonable estimates of our overall error.

2.1 Electric field measurements

The electric field data have been obtained at the NASA Kennedy Space Center (KSC) and the Cape Canaveral Air Force Station (CCAFS). These facilities are located on the east-central coast of the Florida peninsula. During the summer months, thermally driven sea-breeze circulations develop in this area, interact with the Westerlies, and produce lines of convection that often produce heavy precipitation and lightning. In order to identify atmospheric electrical hazards, KSC and CCAFS operate and maintain a large ground-based network of electric field mills at the sites shown in Figure 2.1.

Figure 2.2 shows a photograph of a typical field mill site. Note that each sensor is placed on a level, paved surface that is free from grass and other protruding obstacles, such as trees, buildings, etc., that might distort the local field. The sensors are cleaned at monthly

intervals so any adverse effects from the elements (e.g., sea spray salt deposits, insects, etc.) are minimized.

Each field mill measures the vertical component of the atmospheric electric field, and during normal operation, the data are sent to a central recording station, where they are digitized at a rate of 10 samples per second and stored on nine-track magnetic tape. The digitization accuracy is about 30 V/m and each field mill has a dynamic range of -15 kV/m to +15 kV/m. In order to remove 60 cycle fields, the sensors operate with a low pass filter that has a time constant of about 0.1 seconds. Although this constant is too slow to time-resolve the individual components of a multiple stroke flash, it is more than adequate to resolve the entire discharge (a typical discharge has a duration of about 0.5 seconds). Absolute calibration of each sensor has been estimated to be accurate to within about 10% [Jacobson and Krider, 1976]. All of the field mill data that are analyzed in this study were obtained in 1978 as part of the Florida Thunderstorm Research International Project (TRIP) [Pierce, 1976].

2.2 Computation of lightning-caused field changes

Computer methods for identifying lightning and computing values of lightning-caused changes in the electric field have been described by Maier and Krider [1986] and Koshak and Krider [1989]. In this section, we will review these methods and discuss their deficiencies. With these deficiencies in mind, we will then introduce an improved interactive ΔE program.

2.2.1 Identifying lightning in field mill data

Figure 2.3 is an example of the electric field records that were obtained simultaneously at three different field mill sites. These data were obtained at the NASA Kennedy Space Center during a fairly active thunderstorm on July 6, 1978. In this figure, a positive potential gradient is the polarity that would be produced by a positive charge aloft, or equivalently, a negative charge aloft will produce an upward directed field. The abrupt field discontinuities throughout the record are produced by lightning flashes, and it is these field changes that need to be identified and computed.

Since individual Florida thunderstorms can produce thousands of discharges [Livingston and Krider, 1978], manual detection and analysis of each individual lightning event is not a practical procedure. The most obvious characteristic that distinguishes a lightning event from other variations in the field is the simultaneous occurrence of a large field derivative of either plus or minus polarity that lasts a few tenths of a second at two or more field mill sites. Accordingly, the computer algorithms developed by Jacobson and Krider [1976], Maier and Krider [1986], and Koshak and Krider [1989] have used this characteristic for lightning identification. Jacobson and Krider [1976] used an algorithm that began by arranging the field mill data into consecutive 1-second time blocks. The averages of the first two field values in each adjacent block were used to extrapolate a field value to the end of the third time block. If the actual field at the end of the third time block differed by more than 600 V/m from the extrapolated field at two or more sites, a lightning was assumed to have occurred. The time of the flash was taken to be the time at which the majority of sites experienced their maximum field derivative.

2.2.2 Obtaining initial and final fields

Once a lightning event has been found, the time the discharge began (t_i) and the time that it ended (t_f) need to be determined in order to compute a field change. Examples of these times are shown in Figure 2.3 for a large flash that occurred near field mill site 2 just prior to 190700 GMT. Maier and Krider [1986] found the beginning and ending times by calculating the field derivative before and after the flash time and then assigning t_i and t_f to be the times when most sites had field derivatives that were consistently below 1750 V/m/s. Because the shapes of the field changes are often very different from site to site for a particular lightning event, Koshak and Krider [1989] improved this procedure by using a pattern recognition algorithm to move time markers to the proper times t_i and t_f .

2.2.3 The time-varying background field

Since the background electric field is often changing when a discharge occurs, one cannot simply subtract the initial field $E(t_i)$ from the final field $E(t_f)$ to obtain an accurate value of ΔE . Note in Figure 2.3 that the flash just before 190700 GMT at field mill site 2, is preceded by a large field derivative just before t_i and just after t_f , and a similar behavior can be seen for many other flashes in Figure 2.3. These field variations are caused by currents within and near the thundercloud, and the associated displacement current densities (i.e., $\epsilon_0 dE/dt$) can approach tens of nanoamperes per square meter [Krider and Blakeslee, 1985; Koshak and Krider, 1989; Deaver and Krider, 1990]. More accurate field change values can be found using:

$$\Delta E = \left[E_f - \frac{dE}{dt} \Big|_f (\Delta t/2) \right] - \left[E_i + \frac{dE}{dt} \Big|_i (\Delta t/2) \right]. \quad (2.1)$$

In this procedure, about six field values before t_i and after t_f were used to calculate the field derivatives, and $\Delta t = t_f - t_i$ was the duration of the lightning event. Koshak and Krider [1989] have shown that the correction term, $(-dE/dt|_f - dE/dt|_i) \Delta t/2$, can be as large as 40% of the uncorrected field change during active thunderstorms.

The pattern recognition algorithm used by Koshak and Krider [1989] helped to determine a more accurate t_i and t_f for each flash. This procedure also provided more accurate field projections. If for example, t_i and t_f were only approximated, then the interval, Δt , and the field values used to calculate $dE/dt|_i$ and $dE/dt|_f$ could be in error. In a worst case scenario, if two lightning events are very close to one another in time, a slight error in t_i and t_f could produce a background correction that, in reality, is associated with another lightning event.

2.2.4 L- and F-changes

Another factor that needs to be considered in the computation of field changes is the possible presence of a leader L- (leader) or F- (final) change structure in the shape of ΔE [Pierce, 1955]. In Figure 2.3, site 2 contains a F-change structure at about 190516 GMT. In order to show this more clearly, Figure 2.4 gives an expanded view of the flash of interest. Note the initial sharp discontinuity that defines the start of the flash, and then the large positive

peak. After the peak there is a substantial negative field transition (or F-change) lasting about 0.2 seconds. After the F-change, the field returns to a slowly varying background level. Since, we are interested only in the total change in the background level, we must ignore any L- or F-changes in ΔE . To detect these changes, Koshak and Krider [1989] check for large changes in the field derivative before and after the main field discontinuity. Again, the success of this approach depends on the success of pattern recognition iterations in finding the times directly before and after the main field discontinuity defining the flash.

2.2.5 Detection of poor field mill data

Unfortunately, the algorithm discussed by Koshak and Krider [1989] cannot be used to analyze poor field mill data. Examples of poor data are given in Figure 2.5, an expanded portion of the data given previously in Figure 2.3. Note how the output from mill 25 is being affected by a 1 Hz background noise signal, although it does still detect lightning events. Mill 18 has spurious field variations that could be due to a local rain shower. In both cases, the lightning field variations, such as is recorded "cleanly" at site 2, is being distorted.

At least two problems are caused by noise in the field mill data. The first is that the noise can satisfy the lightning detection criteria and produce a false event. As discussed above, a lightning signature is distinguished by a large field change at two or more field mill sites; thus two noisy sites can create a false event. The second problem arises when noisy data are used to compute the time varying background field. Koshak and Krider [1989] have minimized this problem by extrapolating only those fields that exhibit a high degree of linearity, but this method is not perfect.

The records in Figure 2.3 show that data are missing at about 190930 GMT (see the long straight lines connecting the field values) probably due to a short power interruption. Automatic analyses of these records could result in erroneous ΔE values.

2.2.6 Interactive algorithm

In order to improve the detection and ΔE computation of lightning flashes and to eliminate bad field data, we have developed an interactive computer algorithm. The procedure starts by plotting the data on a high resolution CRT display and then making a visual examination to eliminate all poor field mill data. Typically, the computer displays about 10 minutes of data for five field mill sites, with a temporal resolution of 10 samples per second. When searching for bad data, the operator can examine the next 10 minutes of data by simply pushing a mouse key. By scrolling through the data in this fashion, most noise and data drop outs can be detected and then eliminated from further analysis.

After the bad data are eliminated, the operator returns to the beginning of the data file and then scrolls through the good data in order to identify individual lightning events. To do this, the operator selects three or more field mill sites that are spatially separated and then scrolls through the records and marks the times of sharp discontinuities that define each flash using the mouse. The amplitude of the field is automatically normalized on each data frame. After the operator identifies a flash time, the algorithm automatically calculates the values of ΔE using the pattern recognition iterations, L- and F-change checks, and the time varying field corrections that were described above. Within a few seconds, the initial and final times of the flash are plotted on the screen together with dotted lines that show the time-varying field slope

corrections. After the field changes have been computed, the flash times and ΔE values are stored on the computer hard disk.

With this interactive program, the operator can make a decision as to how well a particular ΔE has been analyzed or if in fact the event should be analyzed manually. Figure 2.5 shows a flash at about 190745 GMT (mill 2) that has a very complicated F-change structure. In this case, the interactive algorithm would not be able to obtain an accurate ΔE value with the normal F-change checks, so a manual analysis would be used. The algorithm helps the operator to carry out the ΔE computations, stores the values, and other housekeeping activities that would otherwise be very time-consuming.

2.3 Errors

Since ultimately we will use the ΔE values to compute the locations and magnitudes of changes in the cloud charge distribution, it is important to determine what effect errors in ΔE have on our final charge solution. Intuitively, we might expect that large uncertainties in the ΔE values will produce large uncertainties in the inferred solution, and as shown in section 5.1, this is a correct statement. What is less obvious, however, is that solution error does not necessarily increase in a one-to-one sense with measurement error. Depending on the location of field sensors for instance, even very small amounts of error in ΔE can result in huge solution errors. The effects of ΔE error on solution error are discussed more thoroughly in Chapters 4 and 5.

For the current discussion, we only need an estimate of the total error in ΔE . In our particular problem, the author feels confident that a reasonable upper bound to the ΔE error is

about 10% or 30 V/m, whichever is larger. This estimation includes all sources, e.g., random error in the field measurements, digitization error, inaccuracies in time-varying field and pattern recognition calculations, etc..

CHAPTER 3

FIELD CHANGE ANALYSES

In this chapter, we will review the least-squares optimization procedure that has previously been used to analyze lightning field changes, and we will point out some basic limitations in the method. We will also introduce a new, linear method that can provide new opportunities and new insights.

The primary aim of both analyses is the same. When a lightning discharge occurs, the original charge distribution in and around the cloud is altered, and we would like to describe the location and magnitude of this change. According to Coulomb's Law, any change in the thundercloud charge will produce a change in the field at the ground. In textbook problems, one is usually asked to find the field that is produced by a given charge distribution in the presence of various conductors and/or dielectrics. Here we are interested in the inverse problem, i.e., we want to find the changes in the cloud charge distribution when we are given the values of ΔE . We have previously pointed out that this inverse problem is fundamentally non-unique. In Chapter 4, we will show how external constraints can be used to reduce the solution ambiguities.

3.1 Nonlinear least-squares optimization

Least-squares optimization methods were first applied to the analysis of lightning field changes by Jacobson and Krider [1976]. The analysis begins by assuming that the measured field changes, ΔE_i , can all be described by a simple charge model. The parameters of the model (e.g., charge location and magnitude) are then inferred from the measurements by

minimizing a (reduced) Chi-square function of the form:

$$C_r^2 = \frac{1}{N_f} \sum_{i=1}^m \left(\frac{\Delta E_i - M_i}{\sigma_i} \right)^2 = \frac{C^2}{N_f}, \quad (3.1)$$

where $M_i = M_i(a_k)$, $k=1, \dots, p$, is the model field change value at the i^{th} field mill site; there are p model parameters a_k ; σ_i is the rms measurement error; and $N_f = m - p$ is the number of degrees of freedom (i.e., number of measurements minus the number of unknown model parameters). In practice, the model M_i is nonlinear so nonlinear methods are used to search for the model parameters that minimize C_r^2 .

Because of measurement errors, the minimum values of C^2 for different events are not unique numbers, but are a set of numbers that are distributed according to the C^2 distribution. The expectation value of this distribution is simply the number of degrees of freedom in the solution (i.e., $\langle C^2 \rangle = N_f$). When N_f is increased, the standard deviation of the C^2 distribution decreases so that large values of C^2 become more improbable [Bevington, 1969]. In general, Jacobson and Krider [1976], Maier and Krider [1986], and Koshak and Krider [1989] have found that a value of $C_r^2 < 10$ usually corresponds to a suitable solution when $\sigma_i = 0.05$.

3.1.1 The Marquardt algorithm

The nonlinear search for the optimum parameters has usually been an iterative algorithm first proposed by Marquardt [1963] and subsequently described by Bevington [1969]. In this algorithm, the model function M_i is linearized by expanding it in a Taylor series

and dropping all higher order terms. If we insert the linearized model function back into Eq. (3.1), C_r^2 can now be regarded a function of the model parameter increments, Δa_k :

$$C_r^2(\Delta a_k) = \frac{1}{N_f} \sum_{i=1}^m \frac{1}{\sigma_i^2} \left(\Delta E_i - \left[M_{i0} + \sum_{k=1}^p \frac{\partial M_i}{\partial a_k} \Big|_0 \Delta a_k \right] \right)^2. \quad (3.2)$$

In order to find the optimum values of the increments, i.e. the values that minimize C_r^2 , we take derivatives of C_r^2 with respect to each Δa_k and set the results equal to zero. This produces p equations with p unknowns (parameter increments) that are of the form:

$$\sum_{i=1}^m \frac{1}{\sigma_i^2} (\Delta E_i - M_{i0}) \frac{\partial M_i}{\partial a_k} \Big|_0 = \sum_{l=1}^p A'_{kl} \Delta a_l, \quad (3.3)$$

where A'_{kl} are the elements of an approximative curvature matrix ($p \times p$) given by:

$$A'_{kl} = \sum_{i=1}^m \frac{1}{\sigma_i^2} \frac{\partial M_i}{\partial a_k} \Big|_0 \frac{\partial M_i}{\partial a_l} \Big|_0. \quad (3.4)$$

Thus, we can start with an initial guess of the model parameters and then iterate to find better values by solving Eq. (3.3). The procedure is repeated until a suitably small value of C_r^2 is obtained.

Solving Eq. (3.3) for the parameter increments is known as the expansion method; and this approach is particularly efficient when we are close to a minimum in the C_r^2 function, but slow when we are far from a minimum. The Marquardt algorithm overcomes this deficiency by replacing the matrix A' with $A = A' + \lambda I$, where λ is a positive scalar and I is the identity

matrix. Now, the iteration formula can be written as:

$$\Delta \mathbf{a} = (\mathbf{A}' + \lambda \mathbf{I})^{-1} \mathbf{V}, \quad (3.5)$$

where \mathbf{V} is a k -dimensional vector whose components are given by the terms that are summed on the left side of Eq. (3.3). At the start of the search, λ is made large so that the diagonal elements of \mathbf{A} dominate. The parameter increments in this case are in a direction nearly down the gradient of the C_r^2 hypersurface and the minimum is approached quite rapidly. Since the gradient tends toward zero, and frequently changes direction as a minimum is approached, the value of λ is decreased to favor the expansion method.

3.1.2 The Q- and P-models

The simplest charge model and one that can be used to describe a spherically symmetric lightning event is the point charge or simply the "Q-model" [Jacobson and Krider, 1976; Maier and Krider, 1986]. This model contains four unknown parameters, the charge location (X, Y, H) and magnitude ΔQ . With the Q-model, the field change at the i^{th} field mill site is:

$$M_i = \frac{2\Delta Q H}{4\pi\epsilon_0(H^2 + D_i^2)^{\frac{3}{2}}}, \quad (3.6)$$

where $D_i^2 = (X_i - X)^2 + (Y_i - Y)^2$ and (X_i, Y_i) is the location of the i^{th} field mill site. This model assumes that the field sensors are located on flat, perfectly conducting ground. The factor of 2

in the numerator of Eq. (3.6) comes from an image charge that satisfies the boundary condition at the ground.

A model that is often used to describe a cloud discharge [Koshak and Krider, 1989; Krider, 1989] is a six-parameter point dipole or "P-model." Here, the discharge is assumed to produce field changes on the ground that are described by:

$$M_i = -\frac{1}{2\pi\epsilon_0 R_i^3} \left[\frac{3H(\Delta\mathbf{P}\cdot\mathbf{R}_i)}{R_i^2} - \Delta P_z \right], \quad (3.7)$$

where the point dipole vector $\Delta\mathbf{P}$ has the components $(\Delta P_x, \Delta P_y, \Delta P_z)$, and is located at (X, Y, H) . The position vector, \mathbf{R}_i , points from the i^{th} field mill site to the point dipole. Figure 3.1 shows the geometrical aspects of both the Q- and P-models. In practice, each model is run on the same lightning event and the model that produces the lowest value of C_r^2 is assumed to be correct (provided, of course, that $C_r^2 < 10$) [Maier and Krider, 1986].

3.1.3 Limitations of model fits

A large fraction of lightning discharges alter the cloud charge in ways that produce complex field change patterns, e.g., multi-branched air discharges. Under these circumstances, it is usually not possible to describe the event using a simple Q- or P-model (Koshak and Krider [1989] could describe only about 50% of all large lightning events using Q- and P-models). A reasonable response to such a problem might be to invent more complicated charge models that have several model parameters. As will be seen below, and again in Chapter 4, this is not an acceptable course of action.

In the studies done by Workman, Holzer, and Pelsor [1942] and Krehbiel [1981], it was suggested that the number of measurements sets an upper limit to the complexity of the charge model used. In effect, it was asserted that a solution could not be found because the number of measurements (m) were fewer than the number of model parameters (p).

On the contrary this is not the reason for being restricted to simple models. For instance, one can find the minimum $C^2(\mathbf{a})$ when $m < p$ by simply checking all reasonable values of the parameters until the minimum is found. This can be accomplished on the computer by using nested DO-LOOPS with adequate resolution for parameter increments. Furthermore, the reader is urged to note that the Marquardt algorithm, as it stands, can also be used to find the minimum when $m < p$. Note that for $m < p$, the approximative curvature matrix A' given above is singular (i.e., noninvertible). However, as pointed out by Marquardt [1963], the addition of the term λI to A' removes this singularity so that the minimum can be approached (i.e., $A = (A' + \lambda I)$ is invertible). Bevington [1969] does not mention this point, and in fact, Marquardt [1963] devoted only one sentence to it in his original discussion (see Marquardt [1970] for a full discussion). Thus, even when $m < p$ the measurements allow one to find a solution; this solution is, as always, non-unique.

With these comments in mind, the primary reason for avoiding many parameter models is due to the difficulties associated with adequately constraining the parameters so that physically reasonable solutions are obtained. Unfortunately, the measurements alone do not always provide enough constraint to the model parameters so that more than one solution may be deemed acceptable. In effect, there exist multiple minima in the C^2 hypersurface; if additional

(or "external") constraints are not added to the problem, no clear cut determination of the "proper" solution can be made.

In all least-squares analyses to date (regardless of the algorithm used to find the minimum C_r^2), few constraints, if any have been applied to model parameters. The Marquardt algorithm, most often used, is no exception and this is clearly demonstrated in section 4.2 below. Note that there is the possibility of redefining the error function to be C_r^2 [given in Eq. (3.1)] plus some additional terms that directly constrain the model parameters, however a more desirable approach will be described in section 3.2.

Another limitation of the least-squares methods used to date is that there is no practical way to determine the information content of the measurements. We will now introduce a new analysis method that allows a standard eigenanalysis to be used to determine information content and which provides other advantages as well.

3.2 Fredholm integral formulation

In order to overcome some of the limitations of the least-squares model approach, we will reformulate our inversion problem in terms of a linear system of equations. This is a new and fundamentally different approach to the analysis of lightning field changes.

Many inversion problems have previously been put into the form of a linear Fredholm integral equation of the first kind [Twomey, 1977]:

$$g(u) = \int K(u,v)f(v)dv , \quad (3.8)$$

where $g(u)$ represents measurements, $f(v)$ is an unknown distribution that is to be inferred, and $K(u,v)$ is a kernel function relating the measurements to the unknown distribution. Several examples of physical problems having this general form are given by Twomey [1977]. For instance, an atmospheric temperature profile $T(z)$ [= $f(v)$] can be inferred from measurements of the radiation intensity $I(\lambda)$ [which, apart from a few constants, is $g(u)$] at different wavelengths λ [= u], the kernel being a derivative of an optical transmissivity function. In this case Eq. (3.8) becomes a modified form of the equation of radiative transfer. We will soon see that Coulomb's Law can also be written in the form of Eq. (3.8).

The formal redevelopment of the problem begins with an integral description of the electrostatic potential due to a known volume distribution of charge (see Jackson [1975]). Starting with the well-known divergence theorem:

$$\int_{V'} \nabla' \cdot \mathbf{A} dV' = \oint_{s'} \mathbf{A} \cdot \hat{n} da' \quad (3.9)$$

if we let $\mathbf{A} = \phi \nabla' G - G \nabla' \phi$, where ϕ and G are arbitrary functions of space, we get:

$$\int_{V'} (\phi \nabla'^2 G - G \nabla'^2 \phi) dV' = \oint_{s'} (\phi \nabla' G - G \nabla' \phi) \cdot \hat{n} da' \quad (3.10)$$

which is Green's second identity or Green's theorem. If we identify ϕ and G as the scalar potential and a Green function, respectively, we have the following constraints:

$$\nabla'^2 \phi(\mathbf{r}') = -\rho(\mathbf{r}')/\epsilon_0 \quad (3.11)$$

$$\nabla'^2 G(\mathbf{r}, \mathbf{r}') = -\delta(\mathbf{r}-\mathbf{r}')/\epsilon_0 \quad (3.12)$$

$$G(\mathbf{r}, \mathbf{r}') = \frac{1}{4\pi\epsilon_0|\mathbf{r}-\mathbf{r}'|} + F(\mathbf{r}, \mathbf{r}'). \quad (3.13)$$

Here, the Green function is simply the potential of a unit point charge at \mathbf{r}' plus the potential $F(\mathbf{r}, \mathbf{r}')$ due to a system of image charges outside V' . Substituting Eqs. (3.11) and (3.12) into (3.10) and carrying out the volume integration over the delta function, we obtain an integral relation for the potential:

$$\phi(\mathbf{r}) = \int_{V'} G(\mathbf{r}, \mathbf{r}') \rho(\mathbf{r}') dV' - \epsilon_0 \oint_{S'} \left(\phi \frac{\partial G}{\partial n'} - G \frac{\partial \phi}{\partial n'} \right) da'. \quad (3.14)$$

To solve Eq. (3.14) for the potential, we can pick $F(\mathbf{r}, \mathbf{r}')$ so that either Dirichlet [$G(\mathbf{r}, \mathbf{r}') = 0$ on S'] or Neumann [$\partial G(\mathbf{r}, \mathbf{r}')/\partial n' = 0$ on S'] boundary conditions are satisfied depending on whether we know the value of $\phi(\mathbf{r}')$ or $\partial\phi/\partial n'$ on S' , respectively. For our purposes, the upper half space is the volume of interest, V' , and we require that the potential be zero everywhere on S' as shown in Figure 3.2. In this Dirichlet problem, the integral relation for the potential reduces to:

$$\phi(\mathbf{r}) = \int_{V'} G(\mathbf{r}, \mathbf{r}') \rho(\mathbf{r}') dV'. \quad (3.15)$$

Using the method of images, the appropriate form of $F(\mathbf{r}, \mathbf{r}')$ can be found so that the boundary conditions are satisfied. The potential in V' due to a unit charge in V' and its image below the conducting plane is:

$$G(\mathbf{r}, \mathbf{r}') = \frac{1}{4\pi\epsilon_0} \left(\frac{1}{R} - \frac{1}{\Gamma} \right), \quad (3.16)$$

where $R = [(x-x')^2 + (y-y')^2 + (z-z')^2]^{1/2}$ and $\Gamma = [(x-x')^2 + (y-y')^2 + (z+z')^2]^{1/2}$. Substituting (3.16) into (3.15) gives:

$$\phi(\mathbf{r}) = \frac{1}{4\pi\epsilon_0} \int_{V'} \left(\frac{1}{R} - \frac{1}{\Gamma} \right) \rho(\mathbf{r}') dV'. \quad (3.17)$$

At this point, we can take the gradient of Eq. (3.17) to determine the electric field at all points within V' ; if a lightning discharge alters $\rho(\mathbf{r}')$, we can calculate the temporal change in the field (or potential gradient) at the ground using:

$$\Delta(\nabla\phi(\mathbf{r}) \Big|_{z=0}) = \frac{\hat{z}}{4\pi\epsilon_0} \int_{V'} \frac{2z' \Delta\rho(\mathbf{r}')}{[(x-x')^2 + (y-y')^2 + z'^2]^{3/2}} dV', \quad (3.18)$$

where $\Delta\rho(\mathbf{r}')$ describes the change in the cloud charge distribution that was produced by the lightning discharge.

Adopting the notation of Twomey [1977] we may denote:

$$g(x,y) \equiv \Delta(\nabla\phi(\mathbf{r}) \Big|_{z=0}) \cdot \hat{z} \quad (3.19)$$

$$K(x,y,r') \equiv z'/(2\pi\epsilon_0 [(x-x')^2 + (y-y')^2 + z'^2]^{3/2}) \quad (3.20)$$

$$f(r') \equiv \Delta\rho(r') . \quad (3.21)$$

With these changes in the variables, equation (3.18) becomes:

$$g(x,y) = \int_{V'} K(x,y,r') f(r') dV' \quad (3.22)$$

which is essentially the same as the Fredholm integral equation given previously in Eq. (3.8), with $(x,y) \rightarrow u$ and $r' \rightarrow v$. Here, $g(x,y)$ describes the changes in field anywhere on the ground, $f(r')$ is an unknown charge density distribution, and $K(x,y,r')$ is a geometrical kernel function relating the two. Given a particular (x,y) field mill location on the ground, the magnitude of the kernel function $K(x,y,r')$ can be plotted for arbitrary points in space r' . Figures 3.3 and 3.4 show such plots for representative distances $D = [(x-x')^2 + (y-y')^2]^{1/2}$ from, and altitudes z' above, an arbitrary field mill site location (x,y) .

Before proceeding any further, it will be worthwhile to express Eq. (3.22) in matrix form. We can write the unknown source function as a series of (arbitrary) discrete charges at known locations on a grid as

$$f(r') = \sum_{j=1}^n f_j \delta(r' - r_j) , \quad (3.23)$$

where r_j is the position of the j^{th} grid point and f_j is the value of the change in charge at that point. The field changes at position (x,y) on the ground can then be described by:

$$g(x,y) = \sum_{j=1}^n K(x,y,r_j) f_j . \quad (3.24)$$

Since our measurements are made at a finite number of discrete points on the x-y plane, we can also write (3.24) as:

$$g_i = \sum_{j=1}^n K_{ij} f_j \quad i = 1, \dots, m , \quad (3.25)$$

where m is the number of field mill sites, and n is the number of grid points in the upper half space. The matrix form of Eq. (3.25) is simply:

$$g = Kf , \quad (3.26)$$

where g is now a $(m \times 1)$ column vector of m field change measurements, f is a $(n \times 1)$ column vector of the changes in charge at n grid points in the upper half space, and K is a $(m \times n)$ kernel matrix relating fields to charges.

Thus, by using only Coulomb's Law and the divergence theorem, we are now able to describe our measurements in terms of a linear system of equations. The nonlinearity is present only in the kernel functions as seen in Figures (3.3) and (3.4). Note that these functions are determined by simply evaluating the gradient of the Green function at the ground. Equation (3.26) is completely analogous to the temperature inversion problem that we

mentioned in section 3.1.3 and should not be confused with the linear system given previously in Eq. (3.3).

A number of methods have been developed to solve linear systems such as Eq. (3.26), and many have been discussed by Twomey [1977]. Depending on the particular physical problem at hand, some of the methods of solution are undoubtedly more appropriate than others.

An important and unavoidable characteristic of our approach is the fact that we now have a large number of grid points in the upper half space to consider and we must find a charge value at each of these points. In the temperature inversion discussed above, $T(z)$ is described by using a single column of grid points, but we have the problem of finding $f(\mathbf{r}') = f(x', y', z')$ on a cubical (or cylindrical, etc.) volume of grid points. Since the number of columns in the kernel matrix K is equal to the total number of grid points in the volume, we can expect the size of the kernel matrix to be rather large. Methods of solving Eq. (3.26) that avoid the need to store and invert a large K matrix are described below.

3.2.1 Gradient-constrained linear inversion algorithm

A standard procedure for solving a matrix equation like Eq. (3.26) is the method of constrained linear inversion [Twomey, 1977]. In this procedure, one starts with an error function of the form

$$e(f) = (g - Kf)^2 + \gamma \tilde{f} H f, \quad (3.27)$$

where the tilde symbol denotes transposition, H is a constraint matrix, and γ is a factor that weights the constraint term $\tilde{f}Hf$. If we now take the derivative of e with respect to each of the unknown charge values, f_j ($j = 1, \dots, n$) and set the result equal to zero, we obtain n equations in n unknowns that have the solution:

$$\mathbf{f} = (\tilde{K}K + \gamma H)^{-1} \tilde{K} \mathbf{g}. \quad (3.28)$$

Basically, this inversion formula provides values of \mathbf{f} that minimize the error function, e .

As noted above, we would like to have a procedure that avoids the need for storing or inverting a large kernel matrix. In Eq. (3.28), the matrix to be inverted is intolerably large, because it has dimension $(n \times n)$, where n is the total number of points in our volume grid. One alternative is to select only a few source points (i.e., limit n to 1 or 2 or 3, etc.) and then use an iterative procedure to move the sources around until an acceptable value of e is obtained. This procedure is conceptually similar to the nonlinear search procedure discussed in section 3.1.2, except that now we have an error function with constraints on the charge parameters, \mathbf{f} .

In order to find an optimum charge solution we will introduce an n -dimensional vector, $\mathbf{p} = (x_1, y_1, z_1, \dots, x_n, y_n, z_n)$, that describes the locations of n grid points above the conducting plane with respect to an arbitrary origin. An iterative procedure that can reduce the error function to acceptable levels is to use the following steps:

- (a) choose a starting \mathbf{p} ,
- (b) find the optimum \mathbf{f} using Eq. (3.28),

(c) form a new $\mathbf{p}' = \mathbf{p} - t\nabla e$ (\mathbf{f} fixed), (3.29)

(d) return to step (b),

where the gradient operator $\nabla \equiv (\partial/\partial x_1, \dots, \partial/\partial z_n)$, and t is an adjustable parameter. In practice, we have obtained satisfactory results using this procedure by choosing $t = |\Delta \mathbf{p}|/|\nabla e| = (\Delta r_1^2 + \dots + \Delta r_n^2)^{1/2}/|\nabla e| \equiv (nd^2)^{1/2}/|\Delta e|$, where $\Delta r_j^2 = \Delta x_j^2 + \Delta y_j^2 + \Delta z_j^2$ and $d = 100$ meters.

Basically, one starts with an initial guess of the grid point locations, finds \mathbf{f} by matrix inversion, and then further decreases the error function by moving the grid points down the gradient of e (holding \mathbf{f} fixed). When the new grid point locations are found, the process is repeated. After a few hundred iterations, a much improved value of e is obtained. Since this process is fairly fast, and since the hypersurface $e(\mathbf{p})$ may contain many local minima, we normally choose 1000 or more initial grid point configurations at random, followed by steps (b) through (d) until a suitable value of e is obtained. If all these randomized grid point configurations do not produce a sufficiently small value of e , the value of n is increased by one and the whole procedure is repeated.

Note that because the term γH will dominate small eigenvalues in $\tilde{K} K$ (see section 4.1), the value of n can, in principle, be larger than the number of measurements. In addition, since e and \mathbf{f} are only functions of \mathbf{p} , the constraints we have imposed on \mathbf{f} (through H and n) reduce the entire problem to one of finding the optimum vector \mathbf{p} .

In principle, the above iteration could be done starting with any initial charge configuration. Intuitively, however, one might expect to obtain better results if the first guess

places the source points fairly close to the lightning discharge. To achieve this, we first assume that the discharge is localized about some point \mathbf{r} above the ground. Equation (3.26) then becomes: $\mathbf{g} = \mathbf{Kf} = f_1 \mathbf{K}_1(\mathbf{r}_1) + \dots + f_n \mathbf{K}_n(\mathbf{r}_n)$, where the vectors $\mathbf{K}_1(\mathbf{r}_1)$ are the column vectors of the kernel matrix. Since the flash is localized, $\mathbf{r}_1 \cong \dots \cong \mathbf{r}_n \cong \mathbf{r}$, so that $\mathbf{K}_1(\mathbf{r}_1) \cong \dots \cong \mathbf{K}_n(\mathbf{r}_n) \cong \mathbf{K}(\mathbf{r})$. With this approximation,

$$\mathbf{g} \cong (f_1 + \dots + f_n) \mathbf{K}(\mathbf{r}) \equiv Q \mathbf{K}(\mathbf{r}) \quad (3.30)$$

which is identical to the classic Q-model result given in Eq. (3.6). Now, to obtain an optimum value of $Q(\mathbf{r})$ that is not too large, we can construct an error function of the form: $e = [\mathbf{g} - Q \mathbf{K}(\mathbf{r})]^2 + \gamma Q^2$ which is a degenerate form of Eq. (3.27) with $H = I$ (identity matrix) and $n = 1$. The optimum value of Q at \mathbf{r} is then given, in analogy to the constrained inversion result given in Eq. (3.28) as: $Q_{\text{opt}} = \Sigma[\mathbf{K}_i(\mathbf{r})g_i]/[\Sigma_i(\mathbf{K}_i^2(\mathbf{r})) + \gamma]$. Substituting this into our expression for e gives the minimum error $e_{\text{opt}}(\mathbf{r})$ at any point above the ground. By scanning the upper half space on a grid with 2 km resolution, we can find the value of \mathbf{r} for which $e_{\text{opt}}(\mathbf{r})$ is a minimum, and then this value of \mathbf{r} (denoted by \mathbf{r}_{min}) becomes an optimum starting point (in the least squares sense). In practice, we can obtain a final solution by selecting initial charge configurations that are confined to a cube whose dimensions are 10 km on a side, and whose center point is at \mathbf{r}_{min} . The advantages of the gradient constrained linear inversion over the original Marquardt procedure are discussed in Chapter 4.

3.2.2 Twomey-Chahine algorithm

This method, originally proposed by Chahine [1970] and later modified by Twomey [1975], is an iterative procedure that can be used to solve a matrix equation like (3.26) when the number of unknowns is large. As in any iterative approach, we start with an initial guess of the unknown distribution f^0 , and this guess is thereafter improved until the residual $(g - Kf)^2$ is sufficiently small. In tomographic approaches to solving two-dimensional remote sensing problems, Twomey [1987] reports successful reconstructions of up to 40,000 unknown quantities. The iteration scheme used to solve these highly underdetermined systems is given by:

$$f_j^{N+1} = f_j^N (1 + \zeta_i^N K_{ij}^S), \quad (3.31)$$

where $K_{ij}^S = K_{ij}/(K_{ij})_{\max}$ is a scaled kernel element and $\zeta_i^N = (g/\int K_i(\mathbf{r}')f^N(\mathbf{r}')dV' - 1)$, though other forms of ζ_i^N are possible. Twomey [1975] has shown that successive iterations by Eq. (3.31) lead to a solution that is constrained to the space spanned by the kernel functions, i.e., f is a linear combination of the kernel functions in the form $f(\mathbf{r}') = \sum \alpha_i K_i(\mathbf{r}')$. Note that all portions of $f(\mathbf{r}')$ that are orthogonal to $K_i(\mathbf{r}')$ are not "seen" by the measurements and therefore are not constrained by the measurements. Since $f(\mathbf{r}')$ is forced to be nonorthogonal to the kernel functions, the solution is usually sufficiently constrained by the measurements so that a stable (nonoscillatory) solution results. We have verified that the results are stable when the source is a single point charge lying above the field mill network.

3.2.3 Method of steepest descent

Unfortunately, the Twomey-Chahine iteration was designed to retrieve unknown distributions that are only one polarity (usually positive). We do not need this "polarity constraint" in our problem, since lightning can obviously involve both positive and negative charges. In addition, since the solution is confined to the space spanned by the kernel functions, it is difficult to add other constraints to the solution. In order to overcome these difficulties, we have devised a more general iterative procedure that allows the unknown distribution to take on positive, negative, and zero values, and that also allows for arbitrary external constraints.

We define an error function to be of the form:

$$e(f) = (g - Kf)^2 + \gamma_1 C_1(f) + \gamma_2 C_2(f) + \dots, \quad (3.32)$$

where $C_1(f)$, $C_2(f)$... are the constraint terms, and $\gamma_1, \gamma_2, \dots$ are the associated weighting factors.

The iteration then becomes:

$$f' = f - t \nabla e, \quad (3.33)$$

where t is an adjustable parameter that determines how far one steps down the gradient of the hypersurface $e(f)$, and where the gradient operator $\nabla = \hat{f}_1 (\partial/\partial f_1) + \dots + \hat{f}_n (\partial/\partial f_n)$. In essence, Eq. (3.33) is nothing more than a method of steepest descent applied to a constrained least-squares problem. Fig. 3.5 illustrates the basic idea behind this method. For clarity, the

illustration is for the simple case $n = 2$, i.e. the column vector \mathbf{f} has only two components.

With one iteration by Eq. (3.33), the initial guess \mathbf{f} is updated to the value \mathbf{f}' , and the error function e is decreased.

To find the optimum value of t , we solve the equation:

$$\frac{de(\mathbf{f}')}{dt} = 0. \quad (3.34)$$

For example, if $e(\mathbf{f}) = (\mathbf{g} - \mathbf{Kf})^2 + \gamma \Sigma f_j^2$, the optimum value of t becomes:

$$t = \frac{\gamma \sum_j f_j \frac{\partial e}{\partial f_j} - \sum_i \left(g_i - \sum_j K_{ij} f_j \right) \left(\sum_j K_{ij} \frac{\partial e}{\partial f_j} \right)}{\sum_i \left(\sum_j K_{ij} \frac{\partial e}{\partial f_j} \right)^2 + \gamma \sum_j \left(\frac{\partial e}{\partial f_j} \right)^2}. \quad (3.35)$$

The physical significance of the $\gamma \Sigma f_j^2$ constraint will be discussed in the next chapter.

3.2.4 Landweber iterations

Landweber [1950] has proposed another iteration formula for solving Fredholm integral equations of the first kind:

$$\mathbf{f}^N = \mathbf{f}^{N-1} + \tilde{K} (\mathbf{g} - \mathbf{Kf}). \quad (3.36)$$

Landweber has shown that if the kernel functions satisfy the constraint: $\iint K^2(x,y,\mathbf{r}') dx dy dV' \leq 2$, then the residual $e = (\mathbf{g} - \mathbf{Kf})^2$ must converge to zero and that the solution can be written as:

$$\mathbf{f}^N = (\tilde{K}K)^{-1} [I - (I - \tilde{K}K)^{N+1}] \tilde{K} \mathbf{g} \quad (3.37)$$

(see Chapter 7 of Twomey [1977] for a derivation of this result). In this expression, we have assumed that the initial guess $\mathbf{f}^0 = 0$. Note that the constraint imposed on the kernels poses no additional problem, since we can always divide the system $\mathbf{g} = \mathbf{Kf}$ by an appropriate scaling factor that is incorporated into the kernel elements.

If $N \rightarrow \infty$, Eq. (3.37) approaches an unstable result, $\mathbf{f} = (\tilde{\mathbf{K}}\mathbf{K})^{-1}\mathbf{Kg}$ (see section 4.1 for more on the unstable nature of this solution in the context of error magnification). Twomey [1977] has shown that if the number of iterations is kept small, however, some stability in the solution is retained. In fact, if N is not too large, Eq. (3.37) will filter small eigenvalues in much the same way as the constrained linear inversion technique with $\mathbf{H} = \mathbf{I}$ (see section 3.2.1). Thus, a properly truncated Landweber iterative technique is a valid way of solving our problem.

At this point, we can ask what is the relationship between the Landweber iteration method and the method of steepest descent? The connection can be made clear by simply letting $t = 1/2$ and all γ 's = 0 in the method of steepest descent [see Eq. (3.33)]; the resulting iteration formula is then completely equivalent to the Landweber method [Eq. (3.36)]. [Note also that when $e = (\mathbf{g} - \mathbf{Kf})^2$, the gradient of e becomes: $\nabla e = -2\tilde{\mathbf{K}}(\mathbf{g} - \mathbf{Kf})$].

Hence, the Landweber iterative method is a special case of the method of steepest descent. The benefit of the Landweber method, however, is that it converges to the absolute minimum of $(\mathbf{g} - \mathbf{Kf})^2$ when the kernel magnitudes are properly scaled. This is a powerful result, especially in view of the fact that the Landweber iteration is basically equivalent to a gradient search procedure. By contrast, convergence to the absolute minimum of the error function given in Eq. (3.32) using the iteration formula given in Eq. (3.33), is not assured.

CHAPTER 4

EXTERNAL CONSTRAINTS

The primary concern of this chapter is to describe possible constraint functions, $C_1(\mathbf{f})$, $C_2(\mathbf{f})$, etc., that can be used in the method of steepest descent (see section 3.2.3). Since constraints tend to bias the solution toward specific types of distributions, it is important that the constraints be based on sound physical principles. The effects of some of the constraints presented here will be tested later on, in Chapter 5. We will also show that it is necessary to overcome biases in our charge solutions that are produced from variations in the kernel functions (see Figures 3.3 and 3.4). A kernel scaling procedure that is designed to remove such "kernel biases" will be discussed in detail. Later, in Chapter 5, it will be found that this procedure is needed to obtain acceptable solutions when the method of steepest descent, or Landweber algorithms are used.

Before discussing these main points, however, we first examine in a more general context, why external constraints are necessary in solving our problem. In addition, since we will present Q- and P-model results in Chapter 6, we have also included a discussion of the constraining process involved in the Marquardt algorithm.

4.1 The need for external constraints

In Chapter 3, we introduced a linear procedure for inverting field changes to find an unknown volume source distribution. Our unknown distribution, \mathbf{f} , is a $(n \times 1)$ column vector of source charges that produce m field change values on the ground. We store these field change values in a $(m \times 1)$ column vector \mathbf{g} , and a $(m \times n)$ kernel matrix \mathbf{K} relates \mathbf{f} to \mathbf{g} , i.e., \mathbf{g}

$= Kf$. Of course, in any real problem there are errors in the measurements, so we may more accurately describe our problem by writing $g + \epsilon = Kf$, where ϵ is a column vector of measurement errors. With this system of equations, there are three basic reasons for applying external constraints: (1) to reduce possible magnifications of error in ΔE , (2) to reduce solution ambiguities (i.e., to avoid nonphysical solutions), and (3) to remove kernel biases.

The idea of error magnification has already been discussed briefly in section 2.3. In general (i.e., for arbitrary values of m and n), we see where error magnification arises by looking at a straight-forward "solution" to our linear system: $f = (\tilde{K}K)^{-1}\tilde{K}(g + \epsilon)$ [Twomey, 1977]. If $\tilde{K}K$ has small eigenvalues (i.e., if $\tilde{K}K$ is ill-conditioned), then the solution error given by $(\tilde{K}K)^{-1}\epsilon = \text{adj}(\tilde{K}K)\tilde{K}\epsilon/\det(\tilde{K}K) = \text{adj}(\tilde{K}K)\tilde{K}\epsilon/\prod\lambda_i$ becomes very large. Here, $\text{adj}(\)$ and $\det(\)$ are the standard adjoint and determinant operators, respectively, and the λ_i 's are the eigenvalues of $\tilde{K}K$.

The only way to prevent such an error magnification is to effectively increase the small eigenvalues of $\tilde{K}K$. One can see from Eq. (3.31), that this is achieved by adding the constraint matrix γH to $\tilde{K}K$. This adds to each eigenvalue of $\tilde{K}K$ a reasonably large number so that the new set of eigenvalues corresponding to the matrix $(\tilde{K}K + \gamma H)$ are all sufficiently large. The filtering of small eigenvalues is particularly obvious for the case $H = I$. Adding the eigen-equation for $\tilde{K}K$ to the eigen-equation for I gives:

$$\begin{aligned}
& \tilde{K}Kx = \lambda x \\
& + \frac{\gamma Ix = \gamma x}{(\tilde{K}K + \gamma I)x = (\lambda + \gamma)x} \tag{4.1}
\end{aligned}$$

The inversion of $(\tilde{K}K + \gamma I)$ involves new eigenvalues $(\lambda + \gamma)$ that are all larger than λ in magnitude and do not produce a large error magnification.

The charge ambiguities that are inherent in this problem have been briefly discussed in Chapter 1 and Chapter 3. Again, one can uniquely determine the fields from a given set of charges, but to find the charges from a finite number of field observations is fundamentally ambiguous. For example, any spherically symmetric charge distribution with an outer radius R and total charge Q , will produce the same field at $r > R$, i.e., $\mathbf{E} = (Q/r^2)\hat{r}$. If a cloud-to-ground lightning changes the cloud charge distribution in a spherically symmetric way, we will have difficulty in determining the true radial dimension R and charge distribution deposited.

To remedy the situation, we can impose certain restrictions on our solution that are physically reasonable and are based on our knowledge of lightning phenomena. For instance, we might require that the charge density $\rho(r)$ inside the thundercloud does not exceed some maximum limit; or we might restrict the radial dimensions of the charge distribution to be within, say, 4-5 km.

The fact that more than one charge configuration can produce exactly the same field pattern on the ground can be demonstrated in a formal manner. If we split \mathbf{f} into two parts, one part that is orthogonal to the row vectors of the kernel matrix K (defined by \mathbf{f}_o , where $K\mathbf{f}_o \equiv 0$) and one part that lies in the space spanned by the row vectors of K (i.e., a nonorthogonal part

\mathbf{f}_n) we then have: $\mathbf{g} = \mathbf{Kf} = \mathbf{K}(\mathbf{f}_o + \mathbf{f}_n) = \mathbf{Kf}_n$ (note that we are neglecting any measurement errors for this discussion). It can be shown (see Appendix) that the portion of the solution that lies in the row vector space of \mathbf{K} , given by \mathbf{f}_n , is unique, i.e., this portion is totally constrained by the measurements. Conversely, the measurements are "blind" to variations in \mathbf{f}_o (i.e., \mathbf{f}_o is completely unconstrained by the measurements since $\mathbf{Kf}_o = 0$). The infinity of possible solutions is then a result of the infinity of possible choices for \mathbf{f}_o when $m < n$. The only way to constrain \mathbf{f}_o is to add external constraints (i.e., constraints other than the measurements). In general, these external constraints can be used to remove physically meaningless portions of both the orthogonal and nonorthogonal parts of the solution.

Note also that there will be solution ambiguities due to measurement errors, since infinitely many solutions can be found to satisfy: $g_i - \epsilon_i < \sum K_{ij}f_j < g_i + \epsilon_i$. Note that this type of ambiguity is a common property of all linear inversion problems and is independent of the ambiguity described in the previous paragraph; the reader is urged not to confuse the two. The inequality above could also be written, with no loss in generality, by replacing f_j with the nonorthogonal portion of the solution $(f_j)_n$; this tells us that there is indeed a need to constrain \mathbf{f}_n as well as \mathbf{f}_o .

Finally, we can add constraints to remove certain biases that are inherent in our kernel functions. If we examine Figures (3.3) and (3.4), we see that the method of steepest descent and Landweber algorithm will always tend to place more charge in regions where the magnitude of the kernel functions are large (see section 4.3.1). For instance, the $1/D^3$

dependence in the kernels (D is the horizontal distance from a field mill site) tends to produce solutions that have greater amounts of charge over the network (i.e., at small D). There will also be a tendency to place more charge at lower altitudes when the source is over the network and more charge at higher altitudes when off the network, i.e., the kernel functions have maxima at altitudes $z_{\max} = D/\sqrt{2}$.

4.2 The Marquardt algorithm as a constrained linear inversion result

In Chapter 3 we have seen that the Marquardt algorithm is basically a combination of a gradient search and an expansion method for finding the minimum of a C^2 hypersurface. In order to illustrate the constraints that are inherent in this algorithm, we will show that it is, in fact, a form of a constrained linear inversion discussed in section 3.2.1 and in Chapter 6 of Twomey [1977]. The reader is also referred to Hoerl and Kennard [1970] and Marquardt [1970] for more detailed discussions of this point. Note that in these earlier publications, the term "ridge regression" is used instead of "constrained linear inversion." Once the constraining process is clearly understood, the advantages of the gradient-constrained linear inversion method over the Marquardt algorithm will become evident.

We begin by defining a sensitivity matrix S of the form:

$$S \equiv \tilde{\nabla} M' = \begin{bmatrix} \frac{\partial M'_1}{\partial a_1} & \cdots & \frac{\partial M'_1}{\partial a_p} \\ \vdots & \ddots & \vdots \\ \frac{\partial M'_m}{\partial a_1} & \cdots & \frac{\partial M'_m}{\partial a_p} \end{bmatrix}, \quad (4.2)$$

where $M'_i \equiv M_i/\sigma_i$ [note that a_1, \dots, a_p , σ_i and M_i have all been defined in section 3.1.1 in the discussion of the Marquardt algorithm]. The change in each M'_i due to small changes in the parameters is:

$$\Delta \mathbf{M}' = \mathbf{S} \Delta \mathbf{a} . \quad (4.3)$$

Obviously, we would like our model field changes to approach the lightning field change measurements $\Delta \mathbf{E}$. To do this, we choose $\Delta \mathbf{M}' = \Delta \mathbf{E}' - \mathbf{M}'$. Since Eq. (4.3) is exactly of the form $\mathbf{g} = \mathbf{Kf}$, we can immediately write down an iteration formula to determine the parameter increments in a way that is analogous to the constrained linear inversion formula given in Eq. (3.31):

$$\Delta \mathbf{a} = (\tilde{\mathbf{S}}\mathbf{S} + \gamma \mathbf{H})^{-1} \tilde{\mathbf{S}} \Delta \mathbf{M}' . \quad (4.4)$$

But Eq. (4.4) is just the iteration formula for the Marquardt algorithm [Eq. (3.5)] when we let $\gamma = \lambda$ and $\mathbf{H} = \mathbf{I}$ (note here that $\tilde{\mathbf{S}}\Delta \mathbf{M}' = \tilde{\mathbf{S}}(\Delta \mathbf{E}' - \mathbf{M}') = \mathbf{V}$, and $\tilde{\mathbf{S}}\mathbf{S} = \mathbf{A}'$).

We conclude that the Marquardt algorithm is basically an iterative procedure for finding the minimum of an error function, e , of the form:

$$e = (\Delta \mathbf{M}' - \mathbf{S}\Delta \mathbf{a})^2 + \gamma(\Delta \mathbf{a})^2, \quad (4.5)$$

where $\Delta \mathbf{M}' = \Delta \mathbf{E}' - \mathbf{M}'$. Hence, only the model increments $\Delta \mathbf{a}$ are being (externally) constrained in the Marquardt algorithm (i.e., the term $\gamma \Delta \mathbf{a}^2$ forces the parameter increments to be small when γ is large). Without directly constraining the model parameters, anomolous results are possible; this important point should be kept in mind when the Q- and P-results of Chapter 6 are reviewed. Note that in the gradient constrained linear inversion algorithm discussed in section 3.2.1, the model parameters are, in fact, directly constrained. In contrast, most investigators to date have only placed "weak" constraints on the range of model parameter values (e.g., charge altitudes were constrained to be positive for Q-model analyses [Jacobson and Krider, 1976]).

Furthermore, if we consider a lightning source that is far from the field mill network, iterations by Eq. (3.5) will tend to make the (X,Y) model parameters large in magnitude (i.e., the model charges will become horizontally displaced from the network in the direction of the lightning source). This results in the elements of $\mathbf{A}' (= \tilde{\mathbf{S}}\mathbf{S})$ getting smaller and smaller so that \mathbf{A}' becomes increasingly ill-conditioned with each iteration of Eq. (3.5). We have previously shown that the addition of the term $\gamma \mathbf{I}$ will remove this ill-conditioned nature. Unfortunately, the Marquardt algorithm decreases γ while approaching the minimum in the C_r^2 surface (i.e., upon locating the source with the model charges). Since $(\mathbf{A}' + \gamma \mathbf{I})$ will also be ill-conditioned when γ is small, and since illconditioned matrices are slow to invert, the net result is that there will be slow convergence toward sources lying well off the network. The large elements of $(\mathbf{A}' + \gamma \mathbf{I})^{-1}$ will also amplify the errors in $\Delta \mathbf{E}_i$, and possibly produce large parameter errors in the absence of sufficient external constraints.

4.3 Constraints used in the method of steepest descent

We will now examine the constraints that we use in the method of steepest descent. We will also comment on the possible choices of the H matrix in the gradient constrained linear inversion method.

4.3.1 Scaling constraint

In section 4.1 we mentioned that the kernel functions can introduce biases into the solution. This can be seen more clearly by writing out one component of the gradient term in Eq. (3.33):

$$\frac{\partial e}{\partial f_k} = -2 \sum_i (g_i - \sum_j K_{ij} f_j) K_{ik} + \gamma_i \frac{\partial C_1}{\partial f_k} + \dots \quad (4.6)$$

Since f_k is updated in proportion to $\partial e / \partial f_k$ [see Eq. (3.33)] which is, in turn, proportional to K_{ik} , variations in K_{ik} will give similar variations in f_k . One way to reduce such biases is to scale the elements of the kernel matrix so that the new set of kernel elements no longer have large variations.

In order to scale our problem, we can pre- and post-multiply K by square diagonal matrices A and B. Now, Eq. (3.26) becomes:

$$\begin{aligned}
\mathbf{g} &= \mathbf{Kf} \\
\mathbf{g} &= \mathbf{KBf}' \\
\mathbf{Ag} &= \mathbf{AKBf}' \\
\mathbf{g}' &= \mathbf{K}'\mathbf{f}'
\end{aligned} \tag{4.7}$$

where $\mathbf{g}' = \mathbf{Ag}$, $\mathbf{K}' = \mathbf{AKB}$, and $\mathbf{f}' = \mathbf{Bf}'$. Equation (4.7) is now a new set of linear equations to be solved.

The scaled kernel matrix elements can now be written as: $K'_{ij} = A_{ii}K_{ij}B_{jj}$, but we still must find the m scalars $A_{ii} \equiv \alpha_i$, $i = 1, \dots, m$ and the n scalars $B_{jj} \equiv \beta_j$, $j = 1, \dots, n$ that optimally reduce the variability in the elements of \mathbf{K}' . Initially, we selected α 's and β 's that minimized a variance function of the form:

$$F(\alpha_i, \beta_j) = \sum_i \sum_j (K'_{ij} - 1)^2 . \tag{4.8}$$

The critical points of this function are given by:

$$\begin{aligned}
\alpha_i &= (\sum_j \beta_j K_{ij}) / (\sum_j \beta_j K_{ij})^2 \\
\beta_j &= (\sum_i \alpha_i K_{ij}) / (\sum_i \alpha_i K_{ij})^2 .
\end{aligned} \tag{4.9}$$

The optimum scalars are then found by the following iterative technique:

- (1) Assume an initial guess of all α_i ,
- (2) Use Eq. (4.9) to find the optimum β_j ,
- (3) $\alpha_{\text{updated}} = \alpha_{\text{previous}} - t\nabla F$; $\{\nabla = \hat{\alpha}_1(\partial/\partial\alpha_1) + \dots + \hat{\alpha}_m(\partial/\partial\alpha_m)\}$,
- (4) Return to step (2) until F is sufficiently small.

With this technique we were able to reduce F by several orders of magnitude to a final value of 5.623E+04 for $m = 25$ and $n = 4851$. Unfortunately, the new set of scaled kernels still possessed undesirable biases.

A better kernel scaling procedure is to set all $\alpha_i = 1$, and iterate each β_j using $\beta' - t\nabla\Psi$ $\{\nabla = \beta_1(\partial/\partial\hat{\beta}_1) + \dots + \hat{\beta}_n(\partial/\partial\beta_n)\}$, where the kernel smoothing function Ψ is given by:

$$\begin{aligned} \Psi(\beta) = \sum_i \sum_j & [(\beta_j K_{ij} - \beta_{j-1} K_{i,j-1})^2 + (\beta_j K_{ij} - \beta_{j+1} K_{i,j+1})^2 \\ & + (\beta_j K_{ij} - \beta_{j-\eta} K_{i,j-\eta})^2 + (\beta_j K_{ij} - \beta_{j+\eta} K_{i,j+\eta})^2] \\ & + (\beta_j K_{ij} - \beta_{j-\eta^2} K_{i,j-\eta^2})^2 + (\beta_j K_{ij} - \beta_{j+\eta^2} K_{i,j+\eta^2})^2] . \end{aligned} \quad (4.10)$$

Here we assume that there is a rectangular grid system with η grid points in both the \hat{x} and \hat{y} directions (the number of grid points in the vertical is not important in the present discussion. In addition, the summations in Eq. (4.10) are performed only over the inner points of the grid system. The set of β_j 's that minimize Ψ produces a new set of kernels that are smooth, i.e., $\beta_j K_{ij} \cong \beta_{j-1} K_{i,j-1}$ (or equivalently $K'_{ij} \cong K'_{i,j-1} \ni (\beta_j K_{ij} - \beta_{j-1} K_{i,j-1})^2$ is small; similar statements can be made for the other terms in Ψ).

4.3.2 Maximum charge density constraint

We have previously mentioned that one possible physical constraint is to set an upper limit on the charge density or the charge value at each grid point. Krehbiel [1986] has recently

reviewed the electrical structure of thunderclouds and reports charge densities that are between 1 and 10 C/km³; and larger charge densities might exist in certain localized regions of the cloud [Winn, Schwede, and Moore, 1974]. We can assume that comparable (order-of-magnitude) values of charge density might be the upper limits of those involved in lightning.

To implement this constraint, we define a constraint function C_1 (see section 3.2.3) as:

$$\gamma_1 C_1(\mathbf{f}) = \gamma_1 \sum_j f_j^2. \quad (4.11)$$

Note that the addition of each constraint term to the residual $(\mathbf{g} - \mathbf{Kf})^2$ in Eq. (3.32) has the effect of changing the shape of our hypersurface $e(\mathbf{f})$, and, in general, will change $\nabla e(\mathbf{f})$.

The effect of this constraint is to minimize the amount of charge it places at each grid point, and/or to spread out existing charge more evenly among the grid points. In the extreme case, $\gamma_1 = \infty$, no charge will be allowed on the grid system. The details of how strongly a particular constraint should be weighted (i.e., what value of γ should be used) are discussed by Hoerl and Kennard [1970] and Twomey [1977]. The values of γ we have used are given in Chapter 5.

The constraint (4.11) can be easily included in the gradient constrained linear inversion method by setting the constraint matrix $\mathbf{H} = \mathbf{I}$ (the identity matrix). (This is the same choice of \mathbf{H} that was used in the Marquardt algorithm as discussed in section 4.2.)

4.3.3 Smoothing constraint

A three-dimensional smoothing constraint that has a form similar to Eq. (4.10) can be written as:

$$\begin{aligned} \gamma_2 C_2(f) = \gamma_2 \sum_j [(f_j - f_{j-1})^2 + (f_j - f_{j+1})^2 \\ (f_j - f_{j-\eta})^2 + (f_j - f_{j+\eta})^2 \\ (f_j - f_{j-\eta^2})^2 + (f_j - f_{j+\eta^2})^2]. \end{aligned} \quad (4.12)$$

This constraint prohibits large variations in the charge values between adjacent grid points. It is a three-dimensional analog of the first differencing constraint commonly used to smooth temperature profiles in satellite inversion problems [Twomey, 1977].

4.3.4 Focusing constraint

This constraint, still being explored by the author at the time of this writing, is closely allied to the form of $C_1(f)$. In this constraint, an attempt is made to minimize the number of grid points that can have a significant amount of charge. We attempt to find solutions with as simple a charge structure as possible without becoming oversimplified. To implement this, we minimize a function that counts the number of grid points that have a significant charge. The constraint is:

$$\gamma_3 C_3(f) = \gamma_3 \sum_j C_j = \gamma_3 \sum_j \left(\frac{f_j^2}{f_j^2 + \delta} \right), \quad (4.13)$$

where δ is a small positive constant. The magnitude of δ determines the sensitivity of the counting procedure. For small values of δ , a small charge on the j^{th} grid point will be counted because $C_j \cong 1$. If δ is chosen large, $C_j \cong 0$, and the grid point will not be counted. Thus, with small values of δ , the constraint inhibits the placement of charge on all grid points so that a huge increase in the error function given by $\gamma_3 \sum C_j = \gamma_3 \sum 1 = \gamma_3 n$ does not result.

4.3.5 Conservation of charge constraint

Conservation of charge is a fundamental law of physics that can be applied to our problem. Note that a cloud discharge, for example, can only move existing charge from one place to another or perhaps separate charges that previously existed in a neutral region. Overall, the discharge cannot create or destroy net charge. Hence, if we add up all changes in charge that were involved in a cloud discharge, the sum must be zero. Note here that we do not need to worry about charge transfers associated with convective or precipitation charging mechanisms that occur during the discharge process, since these effects have already been accounted for by using the time-varying field correction described in Chapter 2. With this in mind, a conservation of charge constraint can be written as:

$$\gamma_4 C_4 (f) = \gamma_4 \left(\sum_j f_j \right)^2 . \quad (4.14)$$

Ideally, if the cloud discharge was completely contained within our grid system and we had infinite grid resolution, the value of γ_4 should, in theory, be set to infinity in order to avoid

disobeying the law of charge conservation. However, as is the case with most inversion problems of this kind, it is generally not preferred to force the solution to a specific result using large weighting factors [Twomey, 1977].

A conservation of charge constraint can only be applied to cloud discharges because ground discharges remove net charge from the grid system in the U.H.S.. In the future, it may be possible to use this constraint to discriminate between ground and cloud discharges. For example, if we start with γ_4 reasonably large and find a small residual $(g - Kf)^2$, then the source was probably a cloud discharge.

The conservation of charge constraint can be implemented by setting $H = 1$ (the "one" matrix having as every element unity) into the gradient constrained linear inversion method. However, the inability of the (singular) one-matrix to remove small eigenvalues may lead to problems of error magnification.

4.3.6 Other constraints

There are many other constraints that could be used with our methods depending on the information that is available. For example, one could use weather radar data to help position the solution grid, and one could make high reflectivity regions within the grid more likely locations for lightning charge. Similarly, at the microphysical level, one could use measurements of cloud temperature, pressure, and moisture content to help position the solution grid, and to pre-bias regions within the grid that might be preferred locations for lightning initiation.

In summary, since there are an infinity of possible solutions to choose from, the addition of carefully selected constraints will allow us to find those solutions that are the most physically reasonable. If a constraint makes the residual $(\mathbf{g} - \mathbf{Kf})^2$ large, one should re-examine how realistic the constraint is, or the values of γ used.

CHAPTER 5

SOLUTION ERROR

The problem of inferring the charge distributions that are deposited by a lightning, solely from ground-based measurements of ΔE has been reduced to solving a linear system of equations $\mathbf{g} = \mathbf{Kf}$. We have developed methods for solving this system, such as the method of steepest descent, and have found that a special case of this method, a Landweber iteration, has a number of advantages. Since there are inherent ambiguities in our solutions that arise from: (1) the non-uniqueness of charge and (2) errors in the values of ΔE , we have stressed the need for adding external constraints and have given some examples in Chapter 4.

In this chapter, we will test the the method of steepest descent and Landweber algorithms using computer generated ΔE data. In these simulations, we first compute the fields from known lightning sources, add realistic measurement errors, and then apply the algorithms to find a charge solution. By comparing the results with the known lightning source, we compute solution error.

Before presenting these simulations, however, we will first describe what a solution error is, how such an error is produced, and how the error is related to the independence of our measurements. The independence analysis will be given in the form of an eigenanalysis as described by Twomey [1977], Chapter 8. When we apply these methods to lightning data obtained at KSC, we will see that the geometry of the field mill network, the geometry and resolution of our source grid, the error in the ΔE values, and the number of measurements of ΔE ϵ all play a role in determining the information content of the field mill network.

5.1 Information content

As a general rule, we expect that if we have more information in our measurements, we will obtain more accurate solutions for the lightning charge distribution. One can view the measurements as the primary or "internal" constraints and any added constraint functions as "external". If the measurements are nearly redundant, our solution will not be clearly defined; in this case, we would say our internal constraint is "weak" or that there is "little information" in the measurements. For example, if all 25 of the KSC field mill sensors were placed very close to one another, each sensor would detect almost the same field change, and the entire network would be roughly equivalent to a single measurement. In this case we would have very little information about the lightning events, and there would be little chance of finding accurate source distributions.

5.1.1 The eigenanalysis test for independence

The eigenanalysis test that we will use to determine the number of independent pieces of information that are contained in m measurements has been discussed by Twomey [1974] and Twomey [1977, Chapter 8]. Starting with our linear system, $\mathbf{g} = \mathbf{K}\mathbf{f}$, we write the unknown charge distribution in terms of a linear combination of orthonormal functions $v_i(\mathbf{r})$ (written discretely as v_i) so that we have:

$$\mathbf{f} = \sum_{i=1}^m a_i v_i = \tilde{\Phi}\mathbf{a} . \quad (5.1)$$

Here, $\tilde{\Phi}$ is a (nxm) matrix whose m column vectors are \mathbf{v}_i , $i = 1, \dots, m$, and $\tilde{\Phi}\tilde{\Phi} = \mathbf{I}$.

Orthonormality can be assured if we let $\tilde{\Phi} = \tilde{\mathbf{K}}\mathbf{U}\Lambda^{-1/2}$ where \mathbf{U} is a (mxm) orthonormal matrix having as columns the m eigenvectors of the covariance matrix $\mathbf{C} \equiv \mathbf{K}\tilde{\mathbf{K}}$, and where Λ is a (mxm) diagonal matrix having as diagonal elements the m eigenvalues of \mathbf{C} . Since any real symmetric matrix (such as \mathbf{C}) can be written in terms of its eigenvalues and eigenvectors, i.e., $\mathbf{C} = \mathbf{U}\Lambda\tilde{\mathbf{U}}$, we may verify the orthonormality of as follows:

$$\begin{aligned}
 \tilde{\Phi}\tilde{\Phi} &= (\Lambda^{-1/2} \tilde{\mathbf{U}}\mathbf{K}) (\tilde{\mathbf{K}}\mathbf{U}\Lambda^{-1/2}) \\
 &= \Lambda^{-1/2} \tilde{\mathbf{U}}(\mathbf{K}\tilde{\mathbf{K}})\mathbf{U}\Lambda^{-1/2} \\
 &= \Lambda^{-1/2} (\tilde{\mathbf{U}}\mathbf{C}\mathbf{U})\Lambda^{-1/2} \\
 &= \Lambda^{-1/2} \Lambda\Lambda^{-1/2} \\
 &= \mathbf{I}.
 \end{aligned} \tag{5.2}$$

We can now write \mathbf{g} and \mathbf{f} as follows:

$$\begin{aligned}
 \mathbf{g} &= \mathbf{K}\mathbf{f} = \mathbf{K}\tilde{\Phi}\mathbf{a} = \mathbf{K}\tilde{\mathbf{K}}\mathbf{U}\Lambda^{-1/2}\mathbf{a} \\
 &= \mathbf{C}\mathbf{U}\Lambda^{-1/2}\mathbf{a} = \mathbf{U}\Lambda\Lambda^{-1/2}\mathbf{a} = \mathbf{U}\Lambda^{1/2}\mathbf{a} \\
 \Rightarrow \mathbf{a} &= \Lambda^{-1/2}\tilde{\mathbf{U}}\mathbf{g} \\
 \therefore \mathbf{f} &= \tilde{\mathbf{K}}\mathbf{U}\Lambda^{-1}\tilde{\mathbf{U}}\mathbf{g}.
 \end{aligned} \tag{5.3}$$

The last line in Eq. (5.3) shows that if the measurements, \mathbf{g} , have an error, $\boldsymbol{\epsilon}$, a solution error, $\mathbf{s} = \tilde{\mathbf{K}}\mathbf{U}\Lambda^{-1}\tilde{\mathbf{U}}\boldsymbol{\epsilon}$ will result.

The square magnitudes of \mathbf{f} , \mathbf{g} , $\boldsymbol{\epsilon}$, and \mathbf{s} are now:

$$\begin{aligned}
f^2 &= \sum_i a_i^2 \\
g^2 &= \sum_i \lambda_i a_i^2 \\
\epsilon^2 &\equiv r^2 g^2 \\
s^2 &= \sum_i \frac{\epsilon_i^2}{\lambda_i}, \quad \epsilon' = \tilde{U}\epsilon,
\end{aligned} \tag{5.4}$$

where r is a fractional number that is arbitrarily chosen to estimate the overall measurement error (i.e., $r \equiv \epsilon^2/g^2$). In the discussion preceding Eq. (4.1), we saw that large solution errors are generated when the measurement errors are divided by small eigenvalues. This result is apparent in the last line of Eq. (5.4). The eigenvalues depend solely on the geometry of the field mill network and on the geometry of the solution grid that is used to describe the lightning charge distribution. It is interesting to note that, given a particular network and grid geometry, each error component ϵ_i is amplified by a distinctly different eigenvalue. Thus the overall solution error is also sensitive to how the measurement errors are distributed across the network.

Typical square magnitudes of the four vectors in (30) can be found by letting $a_i = a_{rms} = 1/\sqrt{m}$ (i.e., by scaling the problem so that $f^2 = 1$). This gives:

$$f^2 = 1$$

$$g^2 = \sum_i \lambda_i (1/m) = \langle \lambda_i \rangle \quad (5.5)$$

$$\varepsilon^2 = r^2 \langle \lambda_i \rangle$$

$$s^2 \simeq \frac{\varepsilon^2}{m} \sum_i \frac{1}{\lambda_i} = \varepsilon^2 \langle 1/\lambda_i \rangle = r^2 \langle \lambda_i \rangle \langle 1/\lambda_i \rangle,$$

where the brackets $\langle \rangle$ denote averages.

We will now write down several criteria that we can use to determine the independence of m measurements. For a scaled problem with $\langle \lambda_i \rangle \simeq \lambda_{\max}/m$ and $\langle 1/\lambda_i \rangle \simeq 1/(m\lambda_{\min})$, we may

write:

FORM 1

If $s^2 \ll f^2 \equiv 1$ (i.e., if $\lambda_{\min} \gg \varepsilon^2/m$)
then the independence of m measurements is assured.

(F.1)

or, equivalently:

FORM 2

If $\lambda_{\min}/\lambda_{\max} \gg (r/m)^2$
then the independence of m measurements is assured.

(F.2)

In general, the β^{th} measurement within a set of m measurements will consist of three parts: (1) a predictable portion that is based on a linear combination of the other $(m-1)$ measurements, (2) an unpredictable part that provides new information about the unknown distribution f_j , and (3) an error term that is proportional to a linear combination of the measurement errors.

These contributions can be summarized as follows:

$$g_\beta = \sum_{i \neq \beta} b_i g_i + \sum_j k_j f_j - \sum_i b_i e_i, \quad (5.6)$$

predictable
information
error
term
term
term

where k_j (or $k(\mathbf{r}')$) is the error in predicting the β^{th} kernel function from all other kernels, i.e.,

$$K_\beta(\mathbf{r}') = \sum_{i \neq \beta} b_i K_i(\mathbf{r}') + k(\mathbf{r}').$$

If the error term is large and/or if the kernel functions are highly dependent such that $k_j \approx 0$, the error term will tend to dominate the information term. In this case, the β^{th} measurement is essentially dependent on the other $(m-1)$ measurements (plus some error) and provides us with no new information about f_j . From the standpoint of our inversions, the β^{th} measurement is not worthwhile. With this thought in mind, we can write down another test for information content:

FORM 3

<p>If $(\sum k_j f_j)^2 \gg (\sum b_i \epsilon_i)^2$ then the independence of m measurements is assured.</p>	(F.3)
---	-------

The equivalence of FORM 3 with FORM 1 and FORM 2 is given in Twomey [1977, Chapter 8].

In the eigenanalyses that we will give below, we will use FORM 2 of the eigentest.

It should be noted that any set of m measurements are dependent if, and only if, $(\sum k_j f_j - \sum b_i \epsilon_i) = 0$. If each measurement within a given set provides new information about f_j , then we can regard each of these measurements as being independent. If, however, each measurement does not provide new information about f_j (i.e., if $(\sum b_i \epsilon_i)^2 \gg (\sum k_j f_j)^2$), then we will say that these measurements are "dependent" even though $(\sum k_j f_j - \sum b_i \epsilon_i) \neq 0$.

5.1.2 Eigenanalyses of the KSC field mill network

Before we can do an eigenanalysis of the KSC field mill network (see Figure 2.1), we must first select a grid system for the source. This is because the eigenvalues are derived from the covariance matrix C , whose elements depend on both the geometry of the field mill network, and the geometry of the grid in V' . (Note, a general discussion of the grid system has been given in section 3.2 and the volume V' is illustrated in Figure 3.2.)

Obviously, we would like to have a large, high resolution grid system so that we can describe every discharge that occurs near the network. We would also like to have a grid that produces large eigenvalues so that we have small solution errors [see the last line in Eq. (5.4)]. To find an optimum grid, and to understand more about how the information content varies with different grid types, we have analyzed several grids with various grid sizes, resolutions, and locations (see below).

To find the eigenvalues of C , we have used a standard Jacobi transformation technique that has been described in Chapter 4 of Twomey [1977]. For each grid, the number of Jacobi transformations was typically 1400-1500. All eigenvalues and eigenvectors were checked by determining how closely $U\Lambda\tilde{U}$ approximated C ; we required agreement to 6 or more significant figures.

In order to have a space-filling grid, we will begin with a horizontal grid dimension of 40 x 40 km², and a vertical dimension of 20 km. With these dimensions, we will try grid resolutions of 1, 2, and 4 km. Table 5.1 shows that the largest eigenvalues are obtained when the grid resolution is high, i.e., 1 km. Hence, there is a trade-off between improved resolution (reduced solution error) and computing time. However, the payoff in reducing the solution error by improving the grid resolution from 2 to 1 km is negligible (i.e., the relative error magnification, s^2/f^2 , is on the order of 10^{-2} in each case). (Note that the values of s^2 given here, and below, are directly comparable since all solution errors are relative to an f^2 value of unity.)

To estimate the number of independent measurements that we have in the KSC network, we can assume a 10% random error in the values of ΔE (see section 2.3). This corresponds to a value of $r = 0.1$ in FORM 2 of the eigentest, or a critical value of $(r/m)^2 = 0.16E-04$, for $m = 25$. Many authors use a more conservative test (see Twomey [1977, Chapter 8]) and let $m = 1$, even though there are still 25 measurements. In this case, the critical value becomes $(r/m)^2 = 0.1E-01$. Now, if we require the scaled eigenvalues, $\lambda_i^s \equiv \lambda_i/\lambda_{\max}$, to be one order of magnitude larger than this conservative test value, we can see in Table 5.1 that we have 25, 10, and 5 independent pieces of information for the grids with 1, 2, and 4 km resolutions, respectively.

Table 5.2 shows the eigenvalues of grids that do not fill the entire space but that preserve a one kilometer spatial resolution. Note here that there is more information content when the grid is large. In effect, it is more difficult to extract independent pieces of information about our unknown source distribution when this source is confined to a small volume of space.

We will now examine the information content of the data as a function of grid location. To do this, we have computed the eigenvalues for a small cubic grid (dimension = 10 km, resolution = 1 km) at different grid locations. The results are summarized in Table 5.3. Note in this table that when the grid is located far from the network, less information is obtained. This expresses the fact that higher order moments of the unknown charge distribution are attenuated with distance. Since distant lightning sources produce similar fields at each field mill site, few independent pieces of information about the source are obtained. If the grid is displaced infinitely far away, C becomes singular, and the solution errors go to infinity (a case of zero information content).

Using the above results, we have selected the grid system in column 2 of Table 5.1, i.e., dimensions $40 \times 40 \times 20 \text{ km}^3$, and a resolution of 2 km. This grid has reasonably large eigenvalues and allows us to adequately resolve a large volume of space without invoking large computation times. All analyses that follow (including the linear analyses presented later in this chapter and in Chapter 6) will be based on this grid.

Now that we have selected a grid, we can investigate the effects of network geometry on the information content of the measurements. Generally, we expect that there will be small eigenvalues when the network covers a small area and large eigenvalues when a larger area is covered, provided that the network is not substantially larger than the area of our grid system.

Table 5.4 shows the eigenvalues of five different networks geometries: (1) a small-area network, KSC networks operated in (2) 1978, (3) 1987, (4) 1991, and (5) a large-area network. All networks had 25 field mills, except for the 1987 and 1991 KSC networks that operated 34 and 31 mills, respectively. The small network was a square grid covering 5.76 km^2 (i.e., the X and Y locations of the mills ranged from 17 km to 19.4 km in steps of 0.6 km) and the large network covered 1024 km^2 (X and Y ranged from 1 km to 33 km in steps of 8 km). The smallest eigenvalue, λ_{\min} , for the large and small networks was 0.1721 and $0.8080\text{E-}09$, respectively. If we use the conservative value of $(r/m)^2$ described above, i.e, $r = 0.1$ and $m \equiv 1$, we find that we have 25 independent pieces of information with the large network, and only 1 piece of information with the small network. By comparison, there are about 10, 11, and 11 pieces of information derived in the 1978, 1987, and 1991 KSC networks, respectively. Note that there are 9 additional measurements in the 1987 network over the 1978 network, yet only 1 to 2 more pieces of information are being gained about the lightning charge distribution (similar comments hold when the 1991 network is compared with the 1978 network). As discussed above in relation to Eq. (5.6), it is not always assured that each additional measurement will provide additional information.

Note that the inversion error magnification is greater with the 1987/1991 networks than with the 1978 network (i.e., the relative error magnification, $s^2/f^2 = s^2/1 = s^2$, for the 1978, 1987, and 1991 networks are $2.322\text{E-}02$, $7.099\text{E-}02$, $2.483\text{E-}02$, respectively). But, the 1987 and 1991 networks have at least one more piece of information than the 1978 network, as described above. This situation is not a contradiction however, since the eigentests described/applied above are

only used to determine the number of independent pieces of information from the total set of measurements. It is up to the inverter to determine which, from the total set, are independent. If this is not done, the mills that produce small eigenvalues will give rise to large error magnifications. In effect, you can get 11 pieces of information from the 1987/1991 networks if and only if you pick the 11 or 12 measurements (of the 31 or 34 present) that are truly independent. If you allow extra (dependent) measurements into the inversion process, the overall information will be decreased due to excessive error magnification. Of course, an alternative to deleting redundant measurements is to filter the small eigenvalues (see section 4.1).

In summary, given the errors in ΔE , not much additional information has been obtained by adding/moving mills (from 1978 to present). Instead, our results show that it is more desirable, albeit less practical, to spread out the 25 mills of the 1978 network into an orthogonal arrangement. Mills placed close to one another clearly give rise to serious error magnification in the absence of small eigenvalue filtering.

5.2 Simulated lightning sources over the network

In order to test how well the method of steepest descent and Landweber algorithms retrieve a volume charge distributions that is directly over the network, we have computed the field changes that would be produced by a known source and then have analyzed these fields with and without simulated measurement errors. We start by examining the Landweber iterative method [Eq. (3.36)] and illustrate the effects of kernel scaling. We have also tested the effects of some of the external constraints discussed in Chapter 4 using the method of steepest descent.

The solution errors that are associated with (point) sources lying off the network will be given in the next section.

For our first test, we inverted the ΔE 's from a 40 C point source at: $X = 18$ km, $Y = 18$ km, $Z = 8$ km. The results of the Landweber iterations are given in Figure 5.1. Note that here and in all solution plots given below, there is a 2 km grid resolution and that X and Y range from -2 km to 38 km and Z ranges from 0 km to 20 km. Contour units are indicated at the top of each plot, and the letters "H" and "L" in the figures designate regions of positive and negative charge, respectively. For our purposes, we are particularly interested in the shape of the inferred solution, the location of the charge centroid, and the total charge.

The volume distribution that is summarized in Figure 5.1 involved 4851 grid points, solutions such as this typically required about 19 minutes of computing time on a VAX computer. In most cases, it took less than 1000 Landweber iterations to insure that the rms relative residual $|\mathbf{g} - \mathbf{Kf}|/\sqrt{m}$ was smaller than the rms relative measurement error $|\epsilon|/\sqrt{m}$. It is important to emphasize that, because there exists errors in \mathbf{g} , we do not try to iterate until each component of the residual vector, $(\mathbf{g} - \mathbf{Kf})$, is equal to zero. Once we know that the vector \mathbf{Kf} is within ϵ of \mathbf{g} , no further improvement in the solution can be guaranteed. In fact, as discussed in section 3.2.4, excessive Landweber iterations that force the residual to zero result in spurious solutions. In the case of the method of steepest descent, the Twomey-Chahine method, or most other iterative methods where absolute convergence is not assured, it is usually difficult to make each component of the residual vector smaller than each component of ϵ . At least one or two components of the residual vector are always found to be too large.

Note in Figure 5.1a, that the contours of iso-charge define almost perfectly concentric circles that are centered on the true (X,Y) source location. The altitude cross-sections in Figure 5.1b, however, show excess charge near the lower boundary. Since the Landweber iteration updates charge at each grid point by an amount that is proportional to the weight of the kernel at that grid point (see section 4.3.1), we believe this excess charge is caused by kernel biasing.

To illustrate the potential benefits of kernel scaling, we have applied Landweber iterations to the same point source as in Figure 5.1, but with a new set of scaled kernels. The values of the original kernels ranged from 0 to 4443, and the scaled values ranged from 0 to 0.02774. The results with the scaled kernels are shown in Figure 5.2. Note in Figure 5.2 that the vertical cross sections have better symmetry and that the maximum charge is closer to the source height of 8 km. (A summary of the errors in these solutions and other results to be discussed below are given in Table 5.5.)

For our next test, we analyzed the same point source as in Figures 5.1 and 5.2, but with a random 10% measurement error and a 30 V/m digitizing error added to each ΔE value (note: all remaining simulations include similar errors). The solution with random errors is summarized in Figure 5.3. Because truncated Landweber iterations effectively remove small eigenvalues (see section 3.2.4), we have avoided large random oscillations that are frequently present in linear solutions. Note that the symmetry of the solution in Figure 5.3 has been preserved. The centroid error is only 1.61 km, and the altitude of maximum charge is close to 8 km. The total charge, however, has been overestimated by 13 Coulombs and this corresponds to a 1.6 km overestimation in the centroid altitude.

Figure 5.4 shows the results that were derived for a centrally located (slanted) discrete dipole source, a typical intracloud discharge. The plan view at $Z = 10$ km shows that the lower positive charge at $(X = 16 \text{ km}, Y = 18 \text{ km})$ has been found; the upper negative charge, however, (Figure 5.4b) is closer to 7 km than to the true source height of 8 km. It appears that the lower positive charge has more influence on the solution than the upper negative charge. The lower positive charge is well pronounced, but the upper negative charge is lower in magnitude and has been "pushed" eastward by the positive charge. Nevertheless, the linear method has detected a substantial charge transfer across the center of the network in the presence of measurement errors.

Figures 5.5 and 5.6 show some extreme cases: (1) a horizontal air discharge, and (2) a vertical intracloud flash, respectively. Figure 5.5 shows that the inversion has done reasonably well in retrieving both the negative and positive charge centers in the horizontal discharge. Since a large spatial gradient of charge is difficult to retrieve with smooth kernels, our results show a horizontal dipole of somewhat greater charge separation, but with a somewhat smaller charge magnitude, so that the charge moment is conserved. Dipole ambiguities of this type have been discussed previously by Kreibiel [1981]. In Figure 5.6 (vertical dipole known source), the lower positive charge dominates the measurements and Landweber iterations produce a solution that looks like a low altitude positive point source. The upper negative charge has been completely ignored in the solution.

Next, we have attempted to retrieve a complex air discharge that is horizontal and is centered over the network. The discharge begins by bringing a total of 40 C from the north to the south, but then splits into two separate branches, one that deposits 20 C to the southeast, and

one that deposits 20 C to the southwest. Figure 5.7 describes the exact known source and provides our retrieval. Apparently the network is unable to resolve fine structure in the lightning source over small distances when the charges are of like sign, because the two charge centers to the south have been merged together into one large volume charge. The overall pattern, however, is reasonably good.

We will now examine the effects of various constraint functions of the form, $C(f)$, that were discussed in Chapter 4. In particular, we will test the effects of limiting the grid point charge, the smoothing constraint, and the conservation of charge constraint. These are preliminary tests, and of course, more work could be done to determine the optimum constraints for various types of lightning sources.

Figure 5.8 shows the effects of limiting the charge density (i.e., of applying the maximum charge density or "max ρ " constraint discussed in section 4.3.2), when the same field changes associated with the known point source in Figure 5.3 are analyzed. Recall from Chapter 4 that the "max ρ " constraint is the constraint that attempts to minimize the charge values at each grid point so that ρ_{\max} is constrained to be small. In Table 5.5, we can see that there are large overestimations of the total charge when point sources were inverted. However, when the constraint $\gamma \sum_j f_j^2$ is used with $\gamma = 1.5 \times 10^8$ (large values of γ are used because the kernels are inversely related to ϵ_0), the total charge in the solution was reduced to 39.9 C, a mere 0.1 C from the known charge of 40 C. Unfortunately, this constraint also tends to spread the total charge out across more grid points. For instance, if there were only 2 grid points, and a total charge of 1 C, placement of all this charge onto one of the grid points would give $\sum f_j^2 = (1)^2 = 1$. However, if

1/2 C was placed at each grid point, we would obtain a smaller value $\sum f_j^2 = (1/2)^2 + (1/2)^2 = 1/4 + 1/4 = 1/2$. This spreading out of charge has distorted the solution, and has resulted in a larger net centroid error equal to 2.30 km.

Figure 5.9 shows that, in the absence of kernel scaling, we can obtain reasonable solutions for point sources by forcing the solution to be smooth. Using $\gamma = 5 \times 10^7$ in the smoothing constraint (see section 4.3.3), the solution has a maximum at the correct charge altitude (8 km). These results are in fair agreement with scaled kernel results given in Figure 5.3.

Finally, Figure 5.10 shows the effect of the conservation of charge constraint (section 4.3.5). Since this constraint should only be used for cloud discharges, we have tested it on the horizontal dipole given previously in Figure 5.5. The results are given in Figure 5.10 with $\gamma = 10^4$. Note that Figure 5.10 has three improvements over the less constrained solution given in Figure 5.5: (1) the location of the positive charge center has been improved; (2) the magnitudes of the positive and negative charges centered at $Z = 10$ km are slightly more equal (i.e., in Figure 5.5a we have $L/H = 249/138 = 1.80$, compared to $273/154 = 1.77$ in Figure 5.10a); and (3) the total charge ($\sum f_j$) is closer to zero [i.e., $(\sum f_j)_{\text{Fig. 5.5}} = 6.45$ C, while $(\sum f_j)_{\text{Fig. 5.10}} = -0.14$ C]. The reader should note in Table 5.5, however, that the overall centroid error has increased from 0.333 km to 0.96 km.

5.3 Simulated point sources off the network

We will now examine the solution errors for (point) source charges that are horizontally displaced from the measuring network. Since most storms occur off the network, these results

will help to determine at what range a discharge can be accurately located.

Figure 5.11 shows the solution for a point source well to the east of the network when no kernel scaling is performed. Because the kernels have a $1/D^3$ dependence, our inversion tends to place more charge closer to the network than far away. The position errors in Table 5.5 show a large error in X ($X_{\text{retrieved}} - X_{\text{true}} = -6.25$ km). When we invert the same source with scaled kernels (Figure 5.12), the error is improved to -3.34 km).

Figures 5.12 through 5.15 show qualitatively similar results but for point sources to the south, west, and north of the network, respectively. All of the retrievals tend to be closer to the network than the true source. The errors in horizontal position are usually improved if kernel scaling is used.

CHAPTER 6

STORM ANALYSIS

In this chapter, we present Q- and P-model results for eight different storms at the NASA Kennedy Space Center in July and August 1978. We will also show the results of our linear inversion for three flashes and will compare these solutions with the associated Q- or P-model results. These comparisons will illustrate the limitations of both inversion methods. We conclude this chapter with a section on future work.

6.1 Flashing rate histograms

Figures 6.1-6.4 show the flashing rate histograms corresponding to all lightning activity that was detected by the field mill network during the storm periods of interest. Each lightning event was identified manually by plotting the digital field mill data onto a high-resolution video monitor as discussed in Chapter 2, sections 2.2.1 and 2.2.6. Previous flashing rate histograms (e.g., Jacobson and Krider, [1976]; Livingston and Krider [1978]; Maier and Krider [1986]; and Koshak and Krider [1989]) were based on an automatic, less accurate method of lightning identification (see section 1). In addition, our manual method also eliminated a threshold criterion in the definition of a lightning event (usually 600 V/m at two or more sites) that tended to produce an underestimation of the true flashing rate.

Figures 6.1 and 6.4 show that the storms on July 5, 6, and 31 are all large with peak flashing rates that exceed 60 flashes over a 5-minute interval. The other storms were small in comparison. In the following, we will compare the Q- and P-results for these small and large storms.

6.2 Q- and P-model results

Figures 6.5-6.11 show Q- and P-model results for all large lightning events, i.e., those lightnings that produced a $\Delta E \geq 1$ kV/m at two or more sites. This selection criterion is somewhat less restrictive than the 1 kV/m at three or more sites used by Maier and Krider [1986], Koshak and Krider [1989], and Krider [1989]. Each figure shows four plots: (1) the altitude of the Q- and P-solutions as a function of time; (2) plan views of the X-Y locations of the Q- and P-solutions relative to the field mill network; (3) projections of the Q- and P-solutions on a vertical plane that is oriented east and west; and (4) projections of the Q- and P-solutions on a vertical plane that is oriented north and south. Only plot types (1) and (2) are given for the storms on July 14 and August 13, 1978, because these storms were considerably off the network and have few optimum solutions.

In each plot, the magnitudes of the Q-solutions are shown as circles with a radius $r = (\Delta Q/E_b)^{1/2}$, where E_b represents an assumed value for the dielectric breakdown of the air [Koshak and Krider, 1989]. In all height vs. time plots, E_b was 0.3 MV/m and in all plan views E_b was 1.0 MV/m, i.e., smaller circles in the plan views provided a less cluttered map.

The P-vectors in all plots show the direction that positive charge has been effectively transferred by the discharge. Since we are analyzing changes in the cloud charge distribution, a P-vector that points from a negative change in charge to a positive change in charge is pointing in the direction of a positive charge flow (or current). In all height vs. time plots, the magnitude of the three-dimensional P-vector is plotted and each vector is rotated clockwise from the vertical

by the zenith angle $\theta = \arccos (\Delta P_z / \Delta P)$. In the plan views and altitude cross sections, the actual projection of the three-dimensional P-vector is shown.

Finally, since Table 5.5 shows solution errors to increase for distant sources and since Koshak and Krider [1989] found anomalous Q- and P-parameters for distant lightning, we have removed Q- and P-results associated with distant lightning from all altitude vs. time, and vertical cross-section plots given in Figures 6.5-6.11. Plan view plots show all solutions that were found within the boundaries of the KSC maps given. This allows the reader to see what solutions have been removed from the other plot orientations.

The region of optimum accuracy of our Q- and P-parameters has been estimated by performing several simulated ΔE -inversions. Obviously, there are an infinity of possible source geometries and locations that could be studied in the simulations. To make things simple yet informative, we have only studied ΔE 's produced from known point charge sources. We expect that the error results will be generally similar to analyses that involve more complicated source distributions.

To determine meaningful statistics of solution error, 100 Q-model inversions were performed at each (X,Y) location of the known point source. Each simulation had different simulated errors, but was always between 0-10%. The errors were also different from field mill to field mill. The known point source was always placed at an altitude of 8 km and was always assigned a charge of 25 C. The values of X and Y ranged from 0 to 35 km in 5 km steps so that a total of 64 source locations were studied for each storm, i.e., for each network geometry encountered. Since 100 inversions were done at each (X,Y) source location, a total of 6400 inversions per network were completed. For known sources located over the network (e.g.,

X = 15 km, Y = 15 km), average position errors were always less than 0.5 km, and average charge errors were typically only a few tenths of Coulombs. Standard deviations were usually less than these average values. For sources located off the network (e.g., X = 30 km, Y = 30 km), position and charge errors were larger (typically 1-2 km and 5-9 C, respectively).

From our simulation results, all Q- and P-solutions that occur within the regions:

STORM (1978)	X RANGE (km)	Y RANGE (km)
July 5	9 - 28	3 - 33
July 6	11 - 29	6 - 33
July 11	9 - 29	3 - 33
July 14	9 - 29	3 - 33
July 17	9 - 28	3 - 33
July 19	9 - 29	3 - 33
July 31	9 - 29	3 - 33
August 13	9 - 28	3 - 33

are assumed to have position errors that are less than 1 km, and, in the case of Q-solutions, charge errors that are less than about 2 C. Any Q- or P-result lying outside their respective region of optimum accuracy given above is not plotted in Figures 6.5-6.11 (except in the plan views). Again, this estimated region of optimum accuracy is based only on point source inversions having Q = 25 C and Z = 8 km, i.e., on typical cloud-to-ground charge parameters

[Koshak and Krider, 1989]. If smaller point charge sources were used in the simulations (e.g., $Q = 1 \text{ C}$ or 5 C) larger position errors, and proportionately larger charge errors would obviously result, thereby changing the optimum region of accuracy.

Table 6.1 summarizes the total number of flashes that were identified in each storm, the number of flashes that were large enough to be analyzed based on our ΔE threshold requirement, the number of solutions that were obtained with a $C_r^2 < 10$, and the number of optimum solutions that were found within the region of optimum accuracy. Note that we have only been able to model a small fraction of all flashes that were identified, and this should be kept in mind when we make inferences about the electrical structure of storms at KSC.

The statistics of our optimum model parameters are summarized in Table 6.2. Note in this table that the two small storms on July 17 and July 19 have average Q-altitudes that are about 1-2 km lower than in the large storms. However, the small storm on July 11 has Q-altitudes that are similar to those found in the large storms. More detailed comparisons will be given later in this document.

6.2.1 Storm on July 5, 1978

As seen from the plan view plot in Figure 6.5, most of the lightning activity in this active storm occurred near the south end of the field mill network. A total of 1209 flashes occurred in 2 hours and 20 minutes.

One feature in the height vs. time plot in Figure 6.5 is the fact that all high-altitude P-vectors point downward, the low-altitude P-vectors point upward, and the mid-altitude

P-vectors tend to point horizontally. The Q-solutions are located within a narrow band from about 6 to 8 km and are co-located with the horizontally pointing P-vectors. This general pattern was found previously by Koshak and Krider [1989] and is a characteristic of all storms that we have analyzed.

The west-east vertical projections in Figure 6.5 show that the low-altitude P-vectors tend to cluster below the Q-region. The high-altitude P-vectors, on the other hand, have a greater horizontal extent and are much more numerous. In addition, the west-east vertical projection shows two separate clusters of events that are separated by about 3 km. The cluster to the west has no low-altitude, upward P-vectors and was not as active as the main cluster to the east.

6.2.2 Storm on July 6, 1978

Figure 6.6 shows that this large storm was located northwest of the field mill network. Koshak and Krider [1989] have previously analyzed a 20-minute portion of this storm that was centered on the time of peak activity, i.e., between about 1935 to 1955 GMT. Here, we have analyzed the entire life-cycle of the thunderstorm. Note that the pattern of Q- and P-solutions that we have obtained is very similar to the July 5 storm.

The storm on July 6 began in the northwest and then moved to the southeast. In the height vs. time plot we show two positive Q-solutions (the hatch-shaded circles) that are systematically higher than most negative Q-solutions. These positive events also occurred on the southeastern fringe of the storm, in the direction of storm movement. The largest positive solution occurred near the end of the storm at about 202230 GMT. All of these features are

reasonably consistent with what we might expect of a positive cloud-to-ground lightning event [Rust, MacGorman, and Arnold, 1981; Brook, Henderson, and Pyle, 1989].

The altitude cross sections on July 6 again show that the low-altitude P-vectors form a compact cluster under the main Q-solutions, and the high altitude P-vectors are more spatially extended. The abrupt termination of solutions to the west marks the westward extent of the region of optimum accuracy.

6.2.3 Storm on July 11, 1978

The height vs. time plots for this small storm (Figure 6.7) shows that the average magnitudes of P-vectors are smaller than those in the larger storms. Note that the scale has been change from the 600 C km in Figures 6.5 and 6.6 to 100 C km in Figure 6.7. It is also interesting to note in Figure 6.7 that there is only one low-altitude upward pointing P-vector and there is not a large separation between the high-altitude P-vectors and the Q-solutions as in the larger storms.

6.2.4 Storm on July 17, 1978

The results for this small storm, given in Figure 6.8, have many of the same characteristics as the storm on July 11. Here, there are no upward pointing P-vectors at low altitude, and there is not a large separation between the high-altitude P-vectors and the Q-solutions. It is interesting to note, however, that there were two positive Q-solutions. The positive altitudes and magnitudes do not appear to be appreciably different than the normal

negative Q-solutions. The negative Q-solution occurring just before 1812 GMT has a very low altitude that may be the result of inadequate area filtering.

6.2.5 Storm on July 19, 1978

Note from Figure 6.9 that this small storm occurred in almost the same region as the large storm on July 5; hence, we can obtain a good comparison between the characteristics of large and small storms from these cases. Here we have far fewer low-altitude P-vectors pointing upward than the July 5 storm and very few optimum Q-solutions. One thing that is clear in Figure 6.9 is that the average magnitudes of the Q- and P-solutions are all smaller than in the July 5 storm.

6.2.6 Storm on July 31, 1978

A portion of this large storm has been analyzed previously by Koshak and Krider [1989], and our new results for the entire storm period are given in Figure 6.10. The distribution in Figure 6.4 shows that this storm had a bimodal flashing rate, and we have been able to extract accurate solutions (i.e., solutions with $C_r^2 < 10$) only for the first portion of the histogram. A detailed analysis of the digital field mill records has shown that many flashes are overlapping in time during the second phase. This has made it very difficult to obtain accurate ΔE 's for individual discharges during this period, and we have obtained only a few acceptable solutions.

In the height vs. time plot and the vertical cross sections in Figure 6.10, the Q-altitudes are much more variable than in Figures 6.5 and 6.6. In fact, many of the high- and low-altitude

P-vectors overlap the Q-solutions. Overall the Q-altitudes vary from just above 4 km to just below 12 km.

6.2.7 Storms on July 14 and August 13, 1978

These storms (shown in Figure 6.11) are included here only to illustrate the difficulties we have with distant storms. Most of the solutions having $C_r^2 < 10$ also had X-Y locations lying outside the region of optimum accuracy. When the region of optimum accuracy was relaxed (i.e., the acceptable area was made larger), the additional solutions obtained were anomalous. Indeed, even with the current area filter used in the August 13 storm, many of the Q- and P-altitudes are anomalous; tightening up the area filter constraint would eventually eliminate all solutions from the plot.

6.3 Linear method results and comparisons

Now that we have seen the Q- and P-results for large and small storms, we will analyze three typical lightning events using the linear method. Two events had successful Q- or P-descriptions, and one event could not be described by Q- or P-models.

Our first flash is taken from the large storm on July 6, 1978. This discharge occurred at 201521.4 GMT and was successfully described by the P-model. The P-parameters were: $X = 14.6$ km, $Y = 23.1$ km, $Z = 10.3$ km and $\Delta P_x = 230$ C km, $\Delta P_y = -55.5$ C km, $\Delta P_z = -123.15$ C km. The linear method produced the distribution that is shown in Figure 6.12. Note that there is

a pronounced dipole-like charge distribution that is in the same general area of the network as our P-result. The centroid of the $|f_j|$ -distribution is located at (19.2 km, 22.4 km, 8.3 km), and $\Sigma f_j = 33.6$ C. However, as we might expect for a complex flash, an extra region of positive charge was effectively deposited toward the southeast. Since asymmetries of this kind do not appear in our computer simulations of dipoles, it is possible that the discharge may have actually deposited positive charge in this region. We probably were able to obtain a satisfactory P-fit only because the positive charge to the southeast is not large.

For our second example, we will analyze a discharge that occurred shortly after the flash discussed above (i.e., at about 202210.4 GMT). This event is of interest because according to our previous Q-results, it was a positive discharge to ground having parameters $X = 17.3$ km, $Y = 17.1$ km, $Z = 10.7$ km, $\Delta Q = -39.1$ C (see Figure 6.6). The results of our linear inversion are shown in Figure 6.13, and are notably more complicated than a spherically symmetric charge distribution. A large amount of negative charge has been effectively deposited just east of the network, and this is consistent with positive charge being transferred to Earth in a positive ground flash. However, an extra amount of positive charge has been deposited to the southwest. The overall centroid of this distribution, (20.7 km, 22.7 km, 8.3 km), is still in fair agreement with the location of the Q-fit. And, the total charge change, $\Sigma f_j = -41.6$ C, is also very close to the Q-fit result given above. Since the negative charge (change) center dominates the solution in Figure 6.13, it is not difficult to understand why an acceptable Q-fit was found for this discharge.

As our last example we will analyze one lightning event from the July 6 storm that we could not fit to either a Q- or a P-model. The results for this flash are shown in Figure 6.14, and

it is clear why neither the Q- or P-model could describe this event. The plan view for $Z = 10$ km shows three prominent charge centers. We saw earlier, in Figure 6.12a, that a point-dipole model could describe three charge centers if one of the three charges is small, but this is not the case here.

6.4 Future work

In the future, we plan to make further analyses of natural lightning with the linear method, and will compare these results with Q- and P-model solutions. Thus far, the linear results are in fair agreement with the Q- and P-model results, and they also have explained why at least one lightning event failed to be described by a Q- or P-model. Further comparisons of this kind will help us to understand the limitations of both inversion procedures, and will eventually lead to a better understanding of thundercloud electricity.

In addition, note that all the work presented here on the new linear technique can be carried over to the study of a fundamentally identical inversion problem, where measurements of $\partial E/\partial t$ are made instead of ΔE , and where retrievals of $\partial p/\partial t$ are found instead of Δp . Specifically, one may write:

$$E(x,y,t) = \int_V K(x,y,r') \rho(r',t) dV' . \quad (6.1)$$

Taking a partial time derivative of this equation gives:

$$\frac{\partial E}{\partial t} (x,y,t) = \int_V K(x,y,r') \frac{\partial \rho(r',t)}{\partial t} dV' . \quad (6.2)$$

This last equation can be solved in much the same way as the field change inversion problem discussed above. In effect, we are dealing with the same linear system $\mathbf{g} = \mathbf{Kf}$, except that the physical meaning of \mathbf{g} ($\partial E/\partial t$ at the ground) and \mathbf{f} (current, $\partial q/\partial t$, in the cloud) have changed. Accordingly, the types of external constraints applied will, in general, be different from those discussed in Chapter 4. Since the kernel function in Eq. (6.2) is the same as before (i.e., the gradient of the Green function evaluated at the ground), all the same kernel scaling techniques discussed above can be applied here. Furthermore, the results of the information content eigenanalyses given above directly apply. Indeed, from a practical standpoint of obtaining reasonable inversion results, most attention is centered around successfully dealing with the kernel functions; the physical meanings of \mathbf{g} and \mathbf{f} are almost rudimentary.

Using a ground-based network of $\partial E/\partial t$ sensors that could also provide values of ΔE , or using field-inferred values of each quantity, our linear method could be used to help improve our understanding of the electrical nature of thunderstorms. Combinations of these inversion results with studies of the Maxwell current density at the ground (e.g., of the type described in Krider and Musser [1982]; Krider and Blakeslee [1985]; and Deaver and Krider [to be published in JGR]) should also be investigated.

We can extend our above comments by noting that any temporal operator (e.g., $\partial/\partial t$, $\partial^2/\partial t^2$, $\int () dt$, etc.) can be applied to Eq. (6.1) and the same linear system $\mathbf{g} = \mathbf{Kf}$ will result. This system, in turn, can be solved by the methods presented in Chapter 3 above. Again, the types of external constraints will generally differ from one inversion problem to the next.

Note that the inversion problem we are considering in Eq. (6.2) should not be confused with an interpolation algorithm discussed in Blakeslee [1984], for contouring current densities.

This algorithm, originally proposed by Dr. Elemer Magaziner (NOAA), cannot reconstruct realistic source distributions, but instead finds a single current pulse a fixed height above each field mill. The main purpose of the algorithm was to interpolate measurements of E (or measurements of ΔE , $\partial E/\partial t$, etc.) for contouring purposes, and as such, is a far more restricted problem than the one we pose above. Furthermore, if more realistic current distributions are found by using the Landweber and/or steepest descent method described in Chapter 3, our methods would also serve as an improved interpolation scheme of E , ∂E , $\partial E/\partial t$, etc. As discussed in Blakeslee [1984], this interpolation is done by simply solving the forward problem after the source distribution is acquired.

Finally, it is of great interest to supplement ground-based measurements of lightning ΔE 's with measurements of ΔE taken above ground with aircraft. Obviously, additional measurement(s) above ground will be highly independent of the ground-based network, so that the information content of the total ground and air measuring system will be much improved. This could ultimately lead to far more accurate lightning charge retrievals.

The reader should note, however, that an aircraft measurement of lightning field change will in general be a vector quantity $\Delta E = (\Delta E_x, \Delta E_y, \Delta E_z)$. The ground-based measurements have, on the other hand, only a z-component value since, under our assumptions, ΔE_x and ΔE_y are always zero on the ground. Hence, before attempting an inversion, our basic Fredholm integral equation [Eq. (3.22)] must be further generalized. Taking the temporal change in the gradient of Eq. (3.17) leads to three linear Fredholm integral equations:

$$\begin{aligned}
g_x(\mathbf{r}) &= \int_{V'} K_x(\mathbf{r}, \mathbf{r}') f(\mathbf{r}') dV' \\
g_y(\mathbf{r}) &= \int_{V'} K_y(\mathbf{r}, \mathbf{r}') f(\mathbf{r}') dV' \\
g_z(\mathbf{r}) &= \int_{V'} K_z(\mathbf{r}, \mathbf{r}') f(\mathbf{r}') dV',
\end{aligned} \tag{6.3}$$

where the g 's are the changes in the x, y, and z-components of the potential gradient vector at location \mathbf{r} , the K 's are the spatial gradients in the x, y, and z directions of the Green function given in Eq. (3.16), and f is the change in the charge density at \mathbf{r}' . These three equations can be added to obtain one Fredholm integral equation:

$$g^*(\mathbf{r}) = \int_{V'} K^*(\mathbf{r}, \mathbf{r}') f(\mathbf{r}') dV'. \tag{6.4}$$

Note that we have used a " g^* " to indicate the sum of the field change components ($g_x + g_y + g_z$), and a " K^* " for the sum of the kernel components ($K_x + K_y + K_z$) to avoid confusion with Eq. (3.22). It is important to emphasize that, since the kernel $K^*(\mathbf{r}, \mathbf{r}')$ is different, and far more complicated than our old kernel $K(x, y, \mathbf{r})$, the feasibility of inverting aircraft ΔE 's along with ground-based measurements is yet to be determined. In particular, the scaling of $K^*(\mathbf{r}, \mathbf{r}')$ is complicated and requires additional investigation. At present, it appears that it is most practical (both mathematically and experimentally) to invert only the last (z-component) equation in (6.3), i.e., to invert ground-based measurements together with any number of aircraft measurements of ΔE_z . Simulated inversions of this equation are currently being investigated by the author.

CHAPTER 7

SUMMARY

We have developed an interactive computer program that plots digital field mill data and can be used to identify and compute the changes in the cloud electric field due to lightning. We have then used this program to compute accurate lightning ΔE -values and flashing rates in eight Florida thunderstorms at the NASA Kennedy Space Center. The lightning field changes have then been analyzed using a nonlinear least-squares minimization procedure to derive the optimum parameters for point charge (Q) and point dipole (P) models.

Three storms analyzed had relatively low flashing rates, while three other storms were considerably more active. We have also illustrated the difficulty in analyzing two distant storms. Because of the long time periods of storm activity studied (e.g., over several hours in most cases), the improved detection and analyses of lightning ΔE 's, and reduced threshold biases, we have been able to make an improved comparison between large and small storms. Even with these differences however, the spatial and temporal development of the Q- and P-solutions were found to be similar to results given in Maier and Krider [1986], Koshak and Krider [1989], and Krider [1989].

We have also developed a new way to analyze lightning field changes. The new approach starts by describing the inversion problem in terms of a linear system of equations given by: $\mathbf{g} = \mathbf{Kf}$, where \mathbf{g} is a column vector of field change measurements, \mathbf{f} is a column vector that specifies the values of lightning charge on a grid system lying above the measuring network, and \mathbf{K} is a kernel matrix relating the two.

We have reviewed some standard linear inversion methods, but because the kernel matrix K is very large, and since positive and negative charges must be retrievable, we have been forced to devise a new technique of inversion. The new (iterative) technique has been strongly motivated by the Twomey-Chahine tomographic inversion method and is essentially based on the method of steepest descent. Each charge value is updated via: $f_j' = f_j - t\partial e/\partial f_j$, where e is an error function of the form: $e(\mathbf{f}) = (\mathbf{g} - K\mathbf{f})^2 + \gamma_1 C_1(\mathbf{f}) + \dots + \gamma_N C_N(\mathbf{f})$, and the C 's are constraint functions. A distinct benefit of this approach is that one can select any type of external constraint(s) desired, i.e., the constraint function are arbitrary.

By letting $t = 1/2$ and removing the constraint terms $C_1(\mathbf{f}), \dots, C_N(\mathbf{f})$, we find that the iterative method produces a stable solution provided the number of iterations is limited (e.g., we have typically used 1000 iterations or less in our analyses presented above). We have shown that this special case of the steepest descent method is equivalent to an iteration technique introduced by Landweber [1950].

Our linear method allows us to determine volume distributions of lightning charge on a grid of any desired resolution. To test the method, we have performed simulated inversions that use computer generated ΔE -values produced from known charge sources. In most cases, both the symmetry and (centroid) location of the retrievals were found to be in fair agreement with the known source. For sources located off the network, systematic errors in source location have been quantified and explained. We feel that the new linear method should be further explored to determine solution errors for source locations and geometries that differ from those presented

here. We also strongly recommend that additional external constraints be explored (see, for instance, section 4.3.4) to further reduce solution ambiguities.

While we were developing the new linear method, we clarified some fundamental problems in field change inversions. We discussed and distinguished the difference between solution ambiguities that result from the nonuniqueness of charge and those that result from measurement error. And, we have clarified how it is possible to find lightning solutions when the number of unknowns is greater than the number of measurements made. We have pointed out that, as early as Workman, Holzer, and Pelsor [1942], the number of charge model parameters used to describe a lightning event have been (incorrectly) limited by the number of measurements. In our work, we have shown that it is possible to obtain valid results of up to $n = 4851$ unknowns using just 25 measurements, provided external constraints are added.

Moreover, even without applying external constraints to the model parameters, we have shown that it is still possible to solve for more unknowns than measurements. In the Marquardt algorithm, we have emphasized that the conditioned approximative curvature matrix $A = A' + \gamma I$ is invertible for fewer measurements than model parameters because the parameter increments are constrained to be small.

APPENDIX

UNIQUENESS OF THE SOLUTION LYING IN THE ROW SPACE OF K

In Chapter 4, we have written the linear system of equations as: $\mathbf{g} = \mathbf{Kf} = \mathbf{Kf}_o + \mathbf{Kf}_n$,

where \mathbf{f}_o and \mathbf{f}_n are the orthogonal and nonorthogonal portions of the solution, respectively.

Methods of inversion that restrict the solution to the space spanned by the row vectors of K are essentially forcing $\mathbf{f}_o = 0$. With this restriction, we will now show that the solution \mathbf{f}_n is unique.

Note that for this discussion we will assume no measurement errors, i.e. the components of \mathbf{g} are known exactly.

Proof (by contradiction):

Given: $\mathbf{g} = \mathbf{Kf}$

Assume that there are solutions of the form $\mathbf{f} = \sum a_i \mathbf{K}_i = \tilde{\mathbf{K}} \mathbf{a}$ where \mathbf{K}_i is the i^{th} row vector of K.

In effect, we assume that $\mathbf{f}_o = 0$. From this set of solutions, pick two distinct solutions:

$$\mathbf{f}_1 = \tilde{\mathbf{K}} \mathbf{a}_1$$

$$\mathbf{f}_2 = \tilde{\mathbf{K}} \mathbf{a}_2 .$$

$$\begin{aligned}
&\Rightarrow K\mathbf{f}_1 = K\mathbf{f}_2 \\
&\Rightarrow K(\mathbf{f}_1 - \mathbf{f}_2) = \mathbf{0} \\
&\Rightarrow K\tilde{K}(\mathbf{a}_1 - \mathbf{a}_2) = \mathbf{0} \\
&\Rightarrow \tilde{\mathbf{b}}K\tilde{K}\mathbf{b} = 0, \text{ where } \mathbf{b} \equiv (\mathbf{a}_1 - \mathbf{a}_2) \\
&\Rightarrow (\tilde{K}\mathbf{b})^2 = 0 \\
&\therefore \tilde{K}\mathbf{b} = \mathbf{0}.
\end{aligned}$$

But since the row vectors of K are assumed to be linearly independent, $\tilde{K}\mathbf{b} = \mathbf{0}$ has only the trivial solution $\mathbf{b} = 0$, so that $\mathbf{f}_1 = \mathbf{f}_2$. Q.E.D.

REFERENCES

- Baker, B., M. B. Baker, E. R. Jayaratne, J. Latham, and C. P. R. Saunders, The influence of diffusional growth rates on the charge transfer accompanying rebounding collisions between ice crystals and hailstones, *Q. J. R. Meteorol. Soc.*, 113, 1193-1218, 1987.
- Barnard, V., The approximate mean height of the thundercloud charges taking part in a flash to ground, *J. Geophys. Res.*, 56, 33-35, 1951.
- Bevington, P. R., Data Reduction and Error Analysis for the Physical Sciences, McGraw-Hill, New York, 1969.
- Blakeslee, R. J., The electric current densities beneath thunderstorms, Ph.D. thesis, University of Arizona, 1984.
- Brook, M., R. W. Henderson and R. B. Pyle, Positive lightningstrokes to ground, *J. Geophys. Res.*, 94, 13,295-13,303, 1989.
- Caranti, J. M., and A. J. Illingworth, Surface potentials of ice and thunderstorm charge separation, *Nature*, 284, 44-46, 1980.
- Chahine, M. T., Inverse problems in radiative transfer: Determination of atmospheric parameters, *J. Atmos. Sci.*, 27, 960-967, 1970.
- Deaver, L. E., and E. P. Krider, Electric fields and current densities under small Florida thunderstorms (to be published in *JGR*), 1991.
- Hacking, C. A., Observations on the negatively charged column in thunderclouds, *J. Geophys. Res.*, 59, 449-453, 1954.
- Hatakeyama, H., The distribution of the sudden change of electric field on the earth's surface due to lightning discharges, in Recent Advances in Atmospheric Electricity, Pergamon, New York, 1958.
- Hoerl, A. E., and R. W. Kennard, Ridge regression: Applications to nonorthogonal problems, *Technometrics*, 12, 69-82, 1970.
- Illingworth, A. J., Charge separation in thunderstorms: Small scale processes, *J. Geophys. Res.*, 90, 6026-6032, 1985.
- Jackson, J. D., Classical Electrodynamics (2nd Edition), John Wiley & Sons, New York, 1975.

- Jacobson, E. A., and E. P. Krider, Electrostatic field changes produced by Florida lightning, *J. Atmos. Sci.*, 33, 103-117, 1976.
- Jayarathne, E. R., J. Hallett, and C. P. R. Saunders, Electrification during riming and ice crystal collisions, *Proc. 6th Int. Conf. Atmos. Elec.*, Paper IX-1, Manchester, 1980.
- Koshak, W. J., and E. P. Krider, Analysis of lightning field changes during active Florida thunderstorms, *J. Geophys. Res.*, 94, 1165-1186, 1989.
- Krehbiel, P. R., An analysis of the charge structure of lightning discharges to ground, *J. Geophys. Res.*, 84, 2432-2456, 1979.
- Krehbiel, P. R., An analysis of the electric field change produced by lightning, Ph.D. thesis, Univ. of Manchester, England, 1981.
- Krehbiel, P. R., The electrical structure of thunderstorms, in The Earth's Electrical Environment, National Academy Press, Washington, D.C., 1986.
- Krider, E. P., and J. A. Musser, Maxwell currents under thunderstorms, *J. Geophys. Res.*, 87, 11,171-11,176, 1982.
- Krider, E. P., and R. J. Blakeslee, The electric currents produced by thunderclouds, *J. Electrostatics*, 16, 369-378, 1985.
- Krider, E. P., Electric field changes and cloud electrical structure, *J. Geophys. Res.*, 94, 13,145-13,149, 1989.
- Landweber, L., An iteration formula for Fredholm integral equations of the first kind, *Am. J. Math.*, 73, 615-624, 1950.
- Latham, J., The electrification of thunderstorms, *Q. J. R. Meteorol. Soc.*, 107, 277-298, 1981.
- Livingston, J. M., and E. P. Krider, Electric fields produced by Florida thunderstorms, *J. Geophys. Res.*, 83, 385-401, 1978.
- Maier, L. M., and E. P. Krider, The charges that are deposited by cloud-to-ground lightning in Florida, *J. Geophys. Res.*, 91, 13,275-13,289, 1986.
- Marquardt, D. W., An algorithm for least-squares estimation of nonlinear parameters, *J. Soc. Indust. Appl. Math.*, 11, 431-441, 1963.
- Marquardt, D. W., Generalized inverses, ridge regression, biased linear estimation, and nonlinear estimation, *Technometrics*, 12, 591-612, 1970.

- Ogawa, T., and M. Brook, Charge distribution in thunderstorm clouds, Q. J. R. Meteorol. Soc., 95, 513-525, 1969.
- Pierce, E. T., Electrostatic field changes due to lightning discharge, Q. J. R. Meteorol. Soc., 81, 211-228, 1955.
- Pierce, E. T., The Thunderstorm Research International Project (TRIP) 1976, Bull. Am. Meteorol. Soc., 57, 1214-1216, 1976.
- Reynolds, S. E., and H. W. Neill, The distribution and discharge of thunderstorm charge centers, J. Meteorol., 12, 1-12, 1955.
- Reynolds, S. E., M. Brook, and M. F. Gourley, Thunderstorm charge separation, J. Meteorol. 14, 426-436, 1957.
- Rust, W. D., D. R. MacGorman, and R. T. Arnold, Positive cloud-to-ground lightning flashes in severe storms, Geophys. Res. Lett., 8, 791-794, 1981.
- Saunders, C. P. R., and C. C. Zhang, Rime density, radial forces and atmospheric electricity, Atmos. Res., 21, 101-111, 1987.
- Schonland, B.F.J., The Flight of Thunderbolts (2nd Edition), Oxford Univ. Press (Clarendon), London and New York, 1964.
- Takeuti, T., Studies on thunderstorm electricity: 2. Ground discharge, J. Geomagn. Geoelec., 18, 13-22, 1966.
- Tamura, Y., Investigations on the electrical structure of thunderstorms, in Recent Advances in Atmospheric Electricity, Pergamon, New York, 1958.
- Twomey, S. A., Comparison of constrained linear inversion and an iterative nonlinear algorithm applied to the indirect estimation of particle size distributions, J. Comput. Phys., 18, 188-200, 1975.
- Twomey, S. A., Introduction to the Mathematics of Inversion in Remote Sensing and Indirect Measurements, Elsevier, New York, 1977.
- Twomey, S. A., Iterative nonlinear inversion methods for tomographic problems, J. Atmos. Sci., 44, 3544-3551, 1987.
- Williams, E. R., The tripole structure of thunderstorms, J. Geophys. Res., 94, 13,151-13,167, 1989.

- Wilson, C. T. R., On some determinations of the sign and magnitude of electric discharges in lightning flashes, Proc. R. Soc., A92, 555-574, 1916.
- Wilson, C. T. R., Investigations on lightning discharges and on the electric field of thunderstorms, Philos. Trans. R. Soc. London, A221, 73-115, 1920.
- Wilson, C. T. R., Some thundercloud problems, J. Franklin Inst., 208, 1-12, 1929.
- Winn, W. P., G. W. Schwede, and C. B. Moore, Measurements of electric fields in thunderclouds, J. Geophys. Res., 79, 1761-1767, 1974.
- Workman, E. J., and R. E. Holzer, A preliminary investigation of the electrical structure of thunderstorms, Aero. Tech. Note 850, Nat. Advan. Comm., Washington, D.C., 1942.
- Workman, E. J., R. E. Holzer, and G. T. Pelsor, The electrical structure of thunderstorms, Aero Tech. Note 864, Nat. Advan. Comm., Washington, D.C., 1942.
- Workman, E. J., and S. E. Reynolds, Electrical phenomena occurring during the freezing of dilute aqueous solutions and their possible relationship to thunderstorm electricity, Phys. Rev., 78, 254-259, 1949.

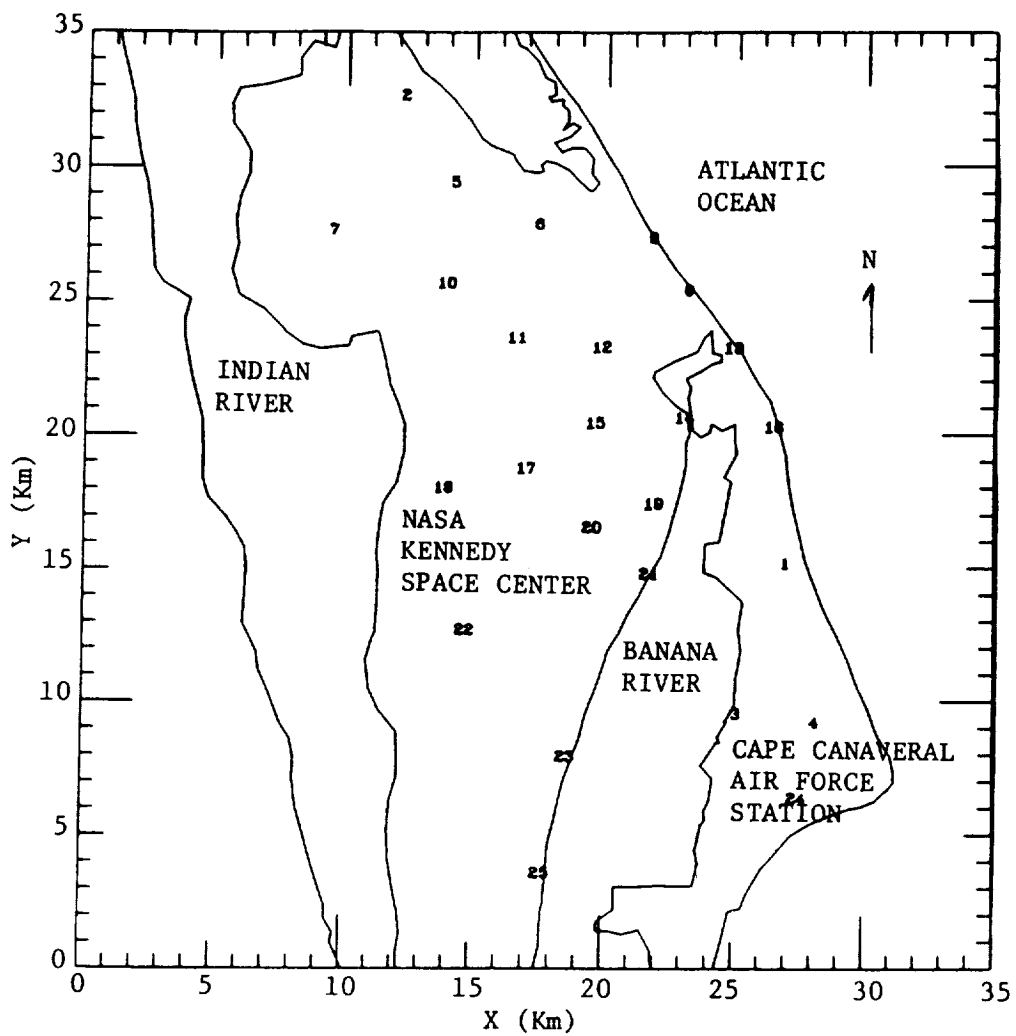


Figure 2.1 Map of the KSC field mill network used in 1978.

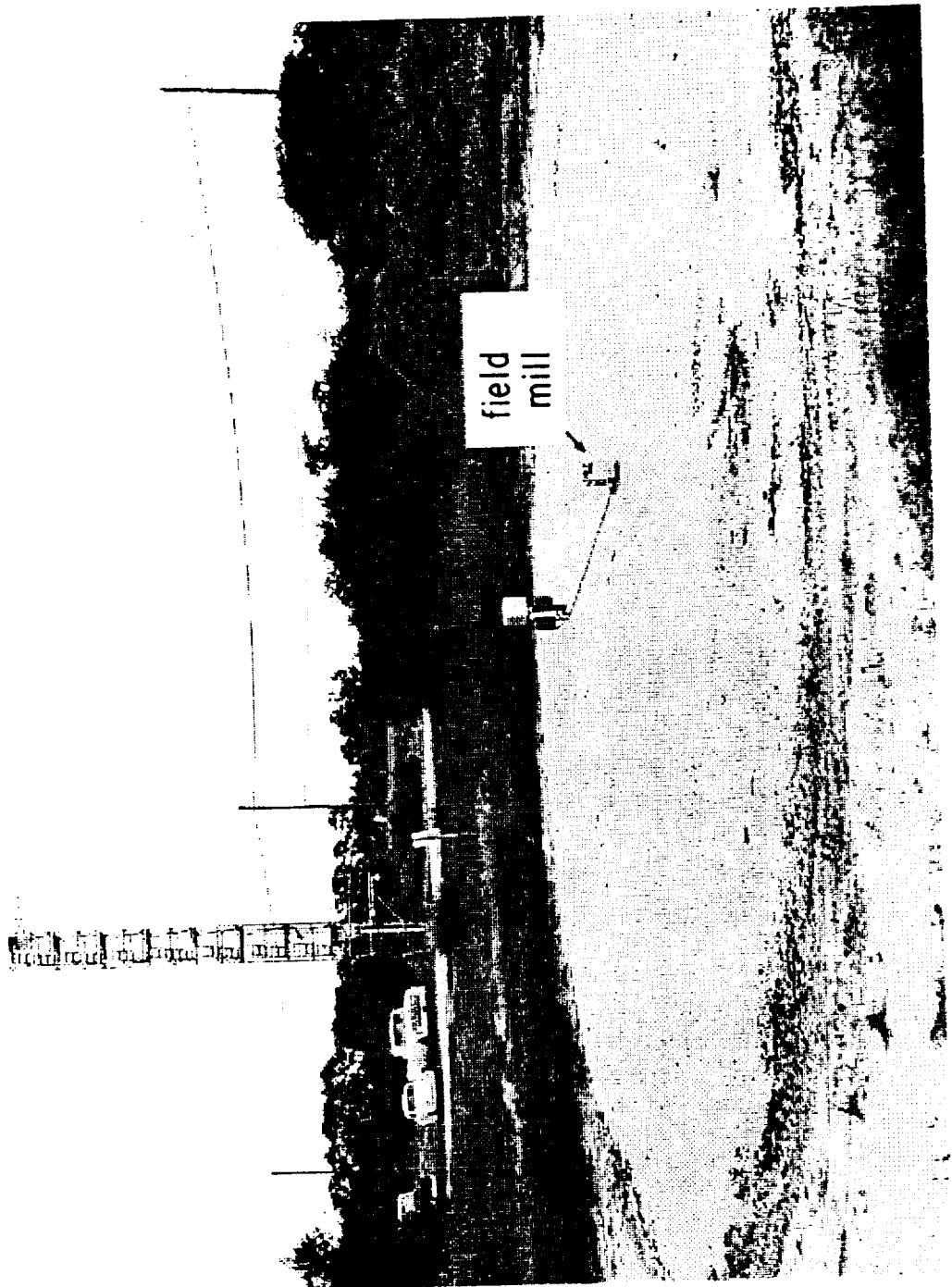


Figure 2.2 A typical electric field mill site.

ORIGINAL PAGE IS
OF POOR QUALITY

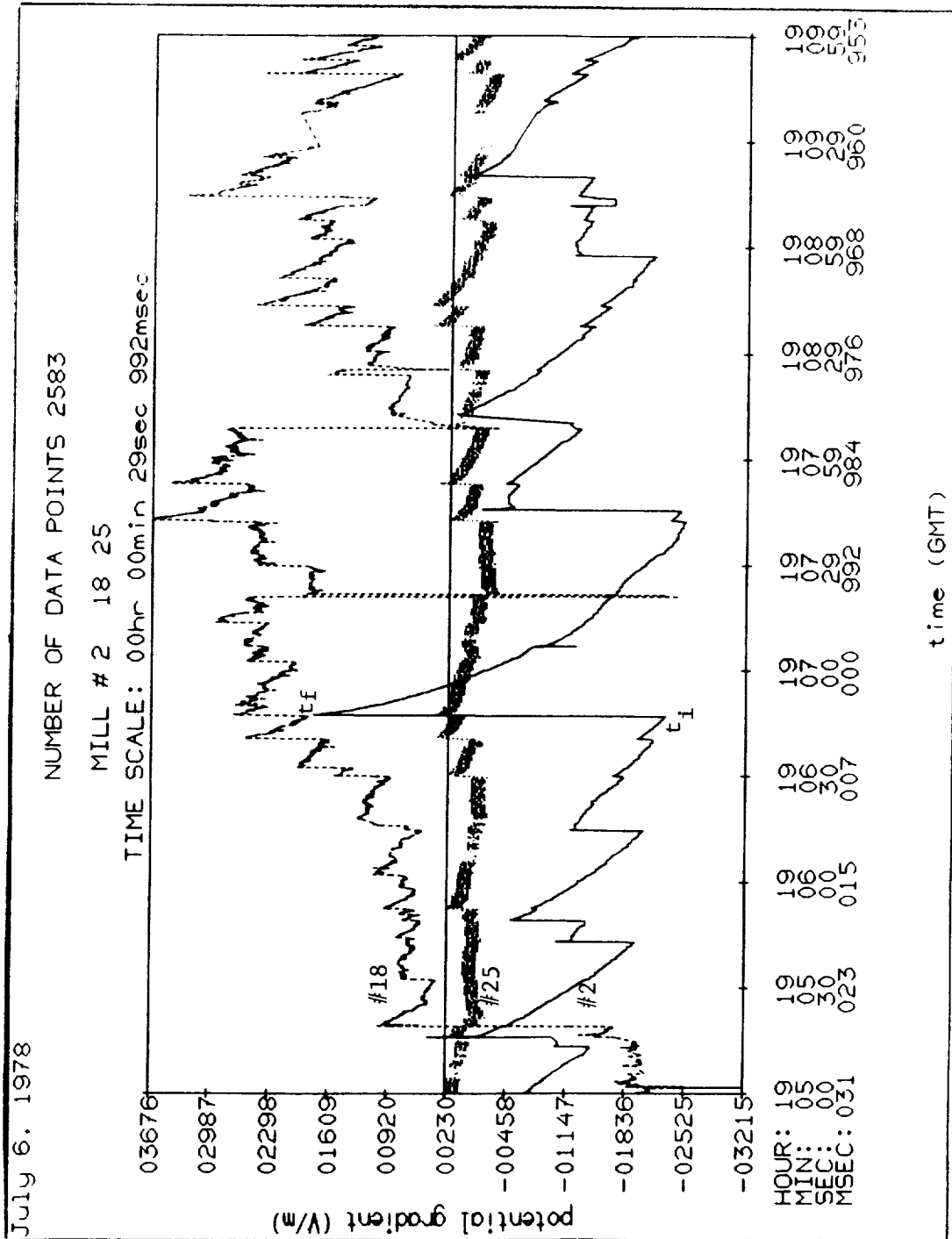


Figure 2.3 An example of KSC digital field mill data.

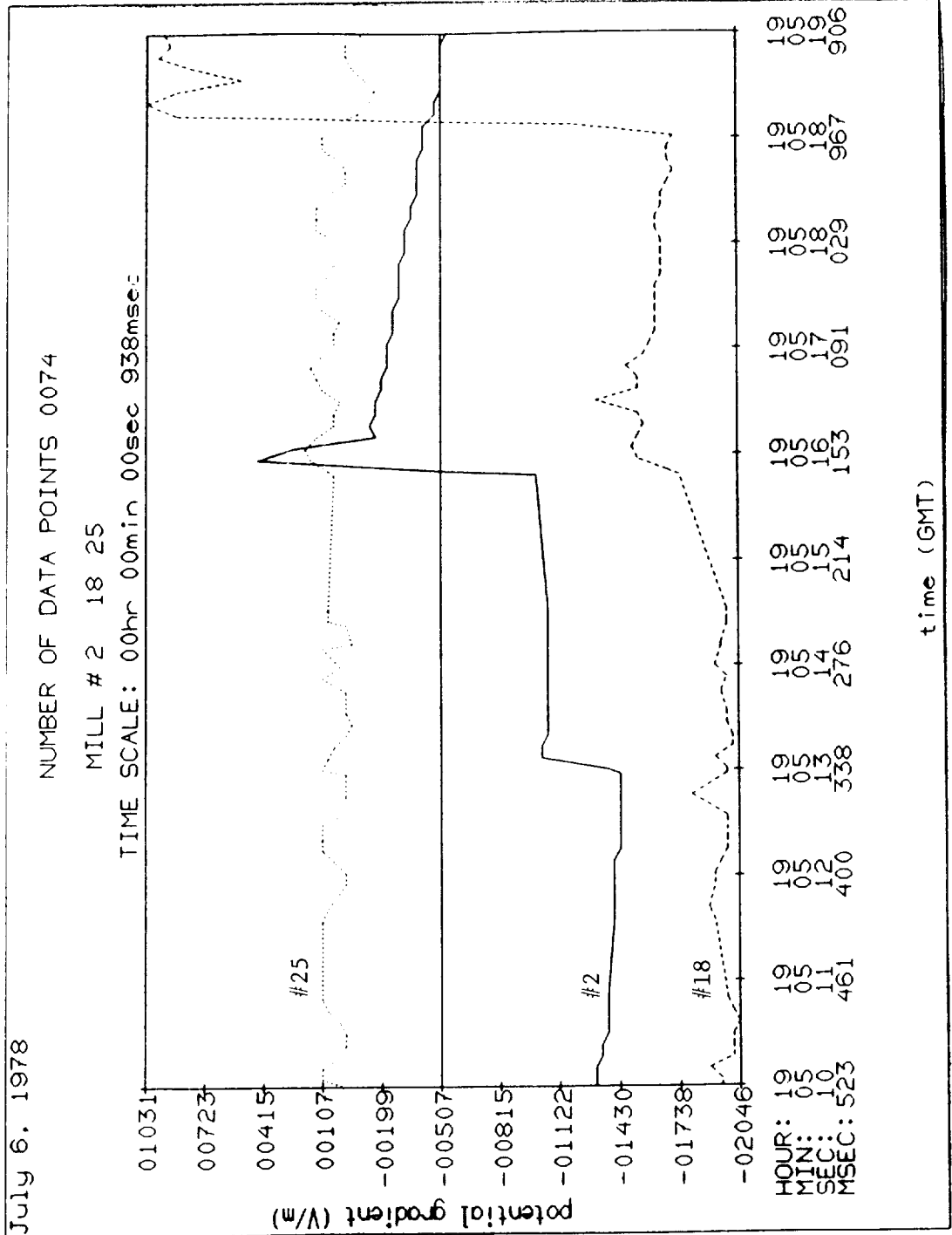


Figure 2.4 An example of an F-change structure (mill #2, second flash).

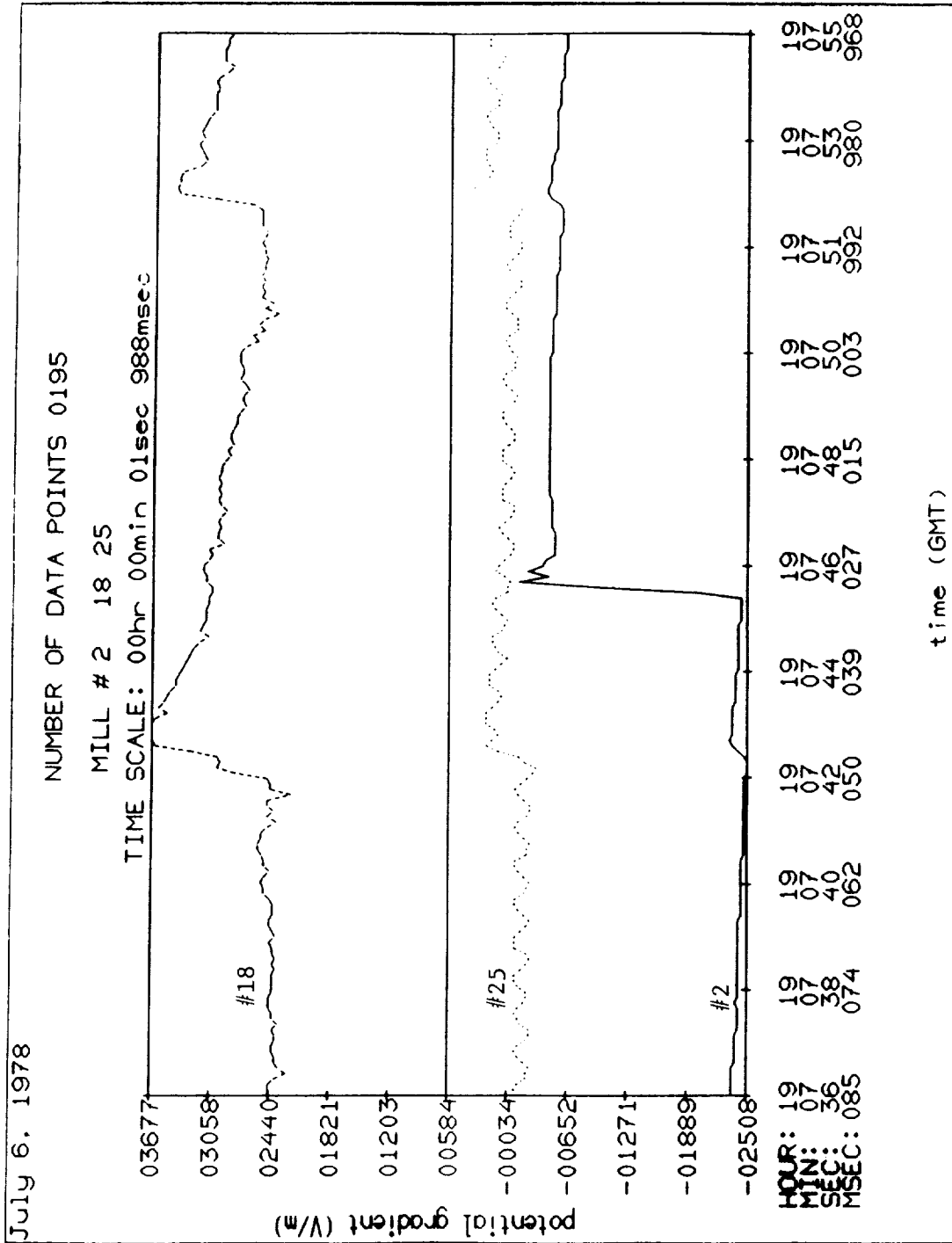
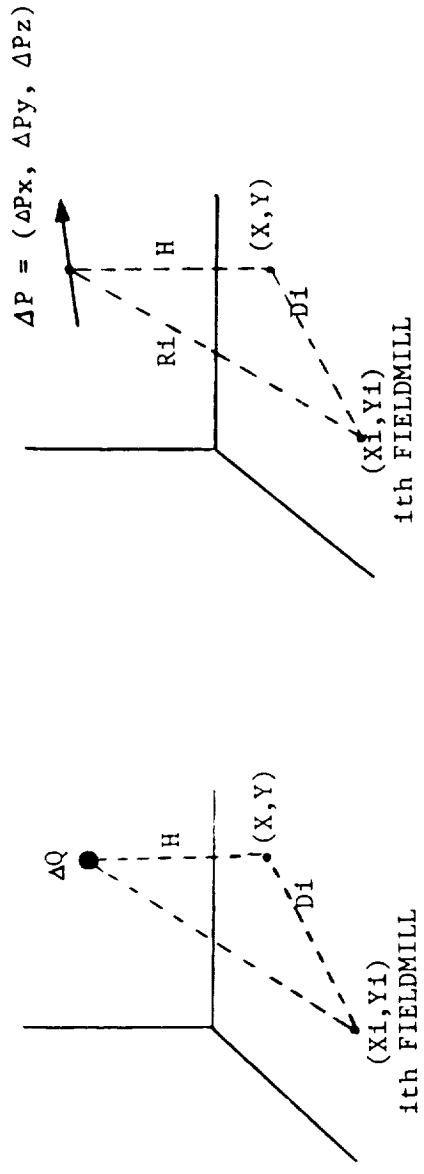


Figure 2.5 An example of a more complicated F-change (mill #2, second flash).



a) 4 Parameters $(X, Y, H, \Delta Q)$ b) 6 Parameters $(X, Y, H, \Delta Px, \Delta Py, \Delta Pz)$

Figure 3.1 Geometry associated with the a) Q-model and b) P-model.

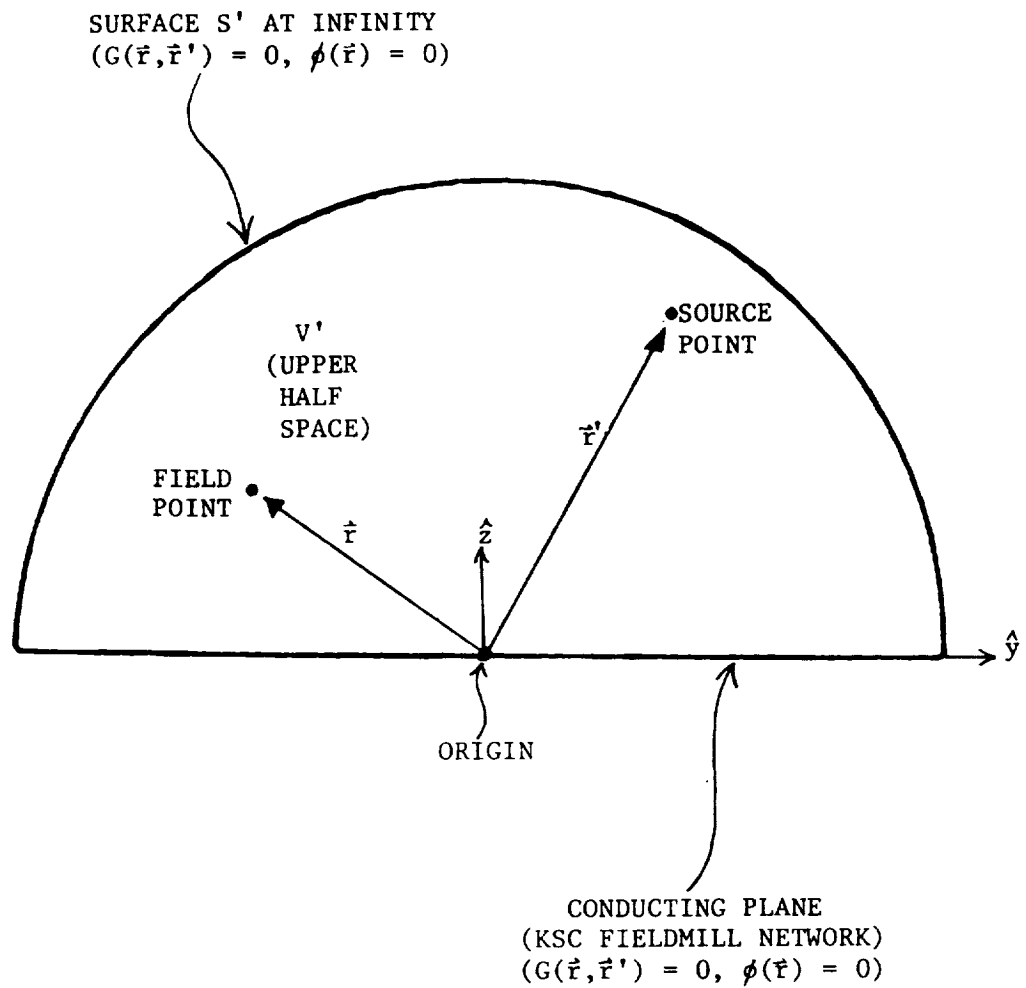


Figure 3.2 Geometry used in the Fredholm integral formulation.

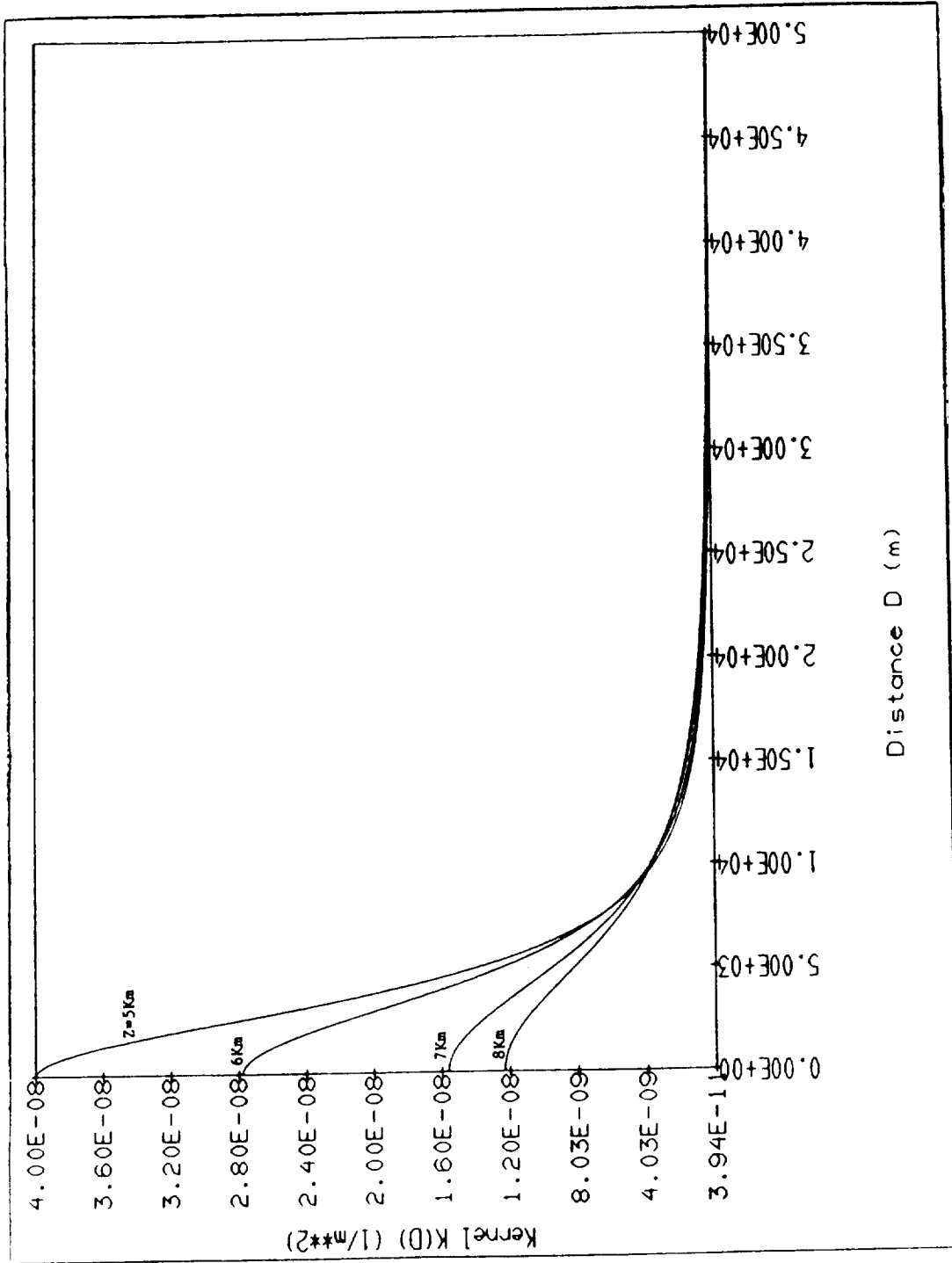


Figure 3.3 Kernel function (times $2\pi\epsilon$) vs. distance from fieldmill, for various altitudes.

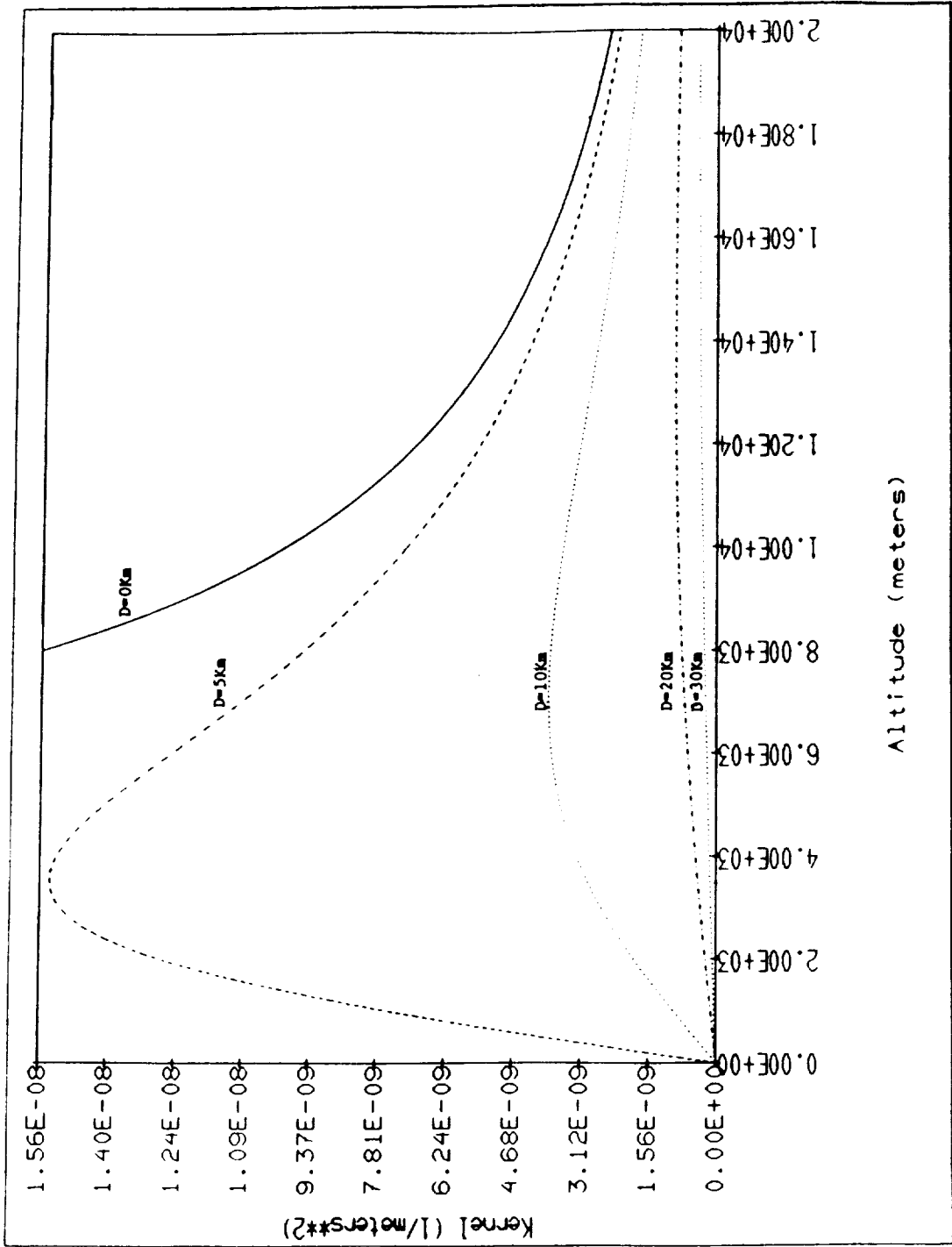


Figure 3.4 Kernel function (times $2\pi\epsilon$) vs. altitude, for various distances from fieldmill.

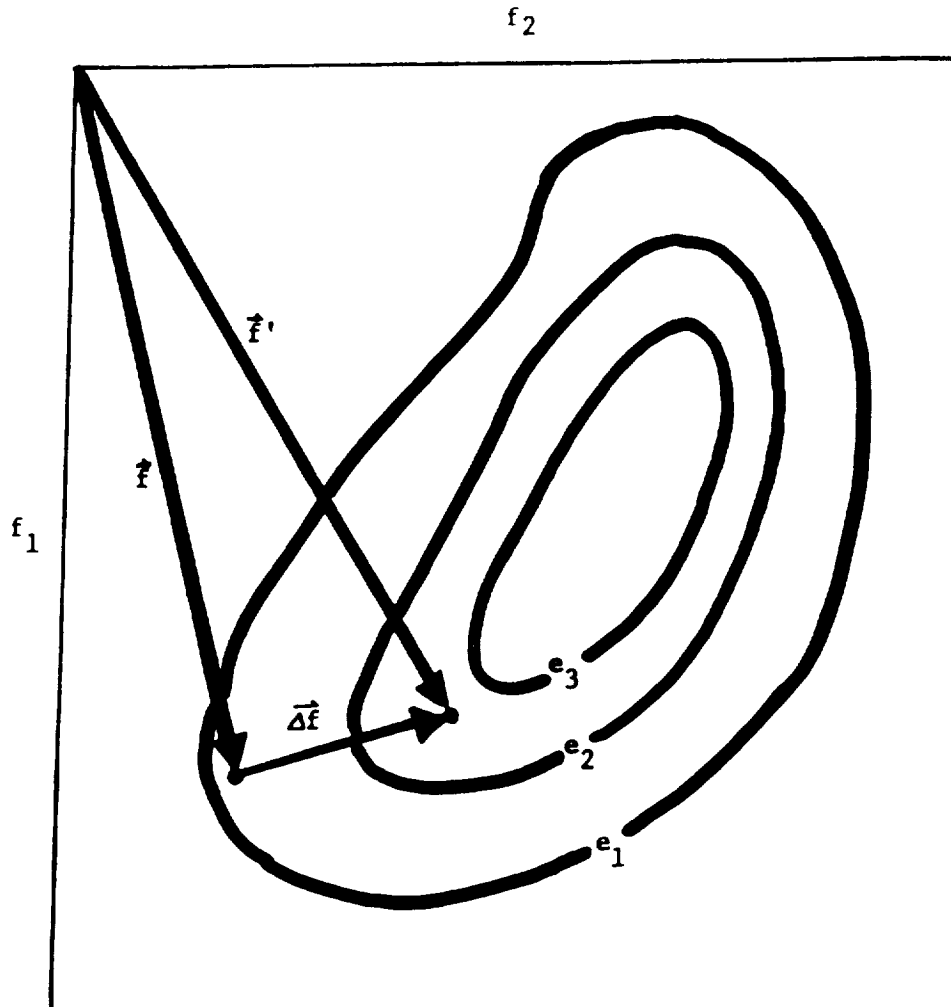


Figure 3.5 Schematic diagram of the method of steepest descent used to invert the linear system: $\vec{g} = K\vec{f}$; note that $\Delta\vec{f} = -t\nabla e$, where t is an adjustable parameter.

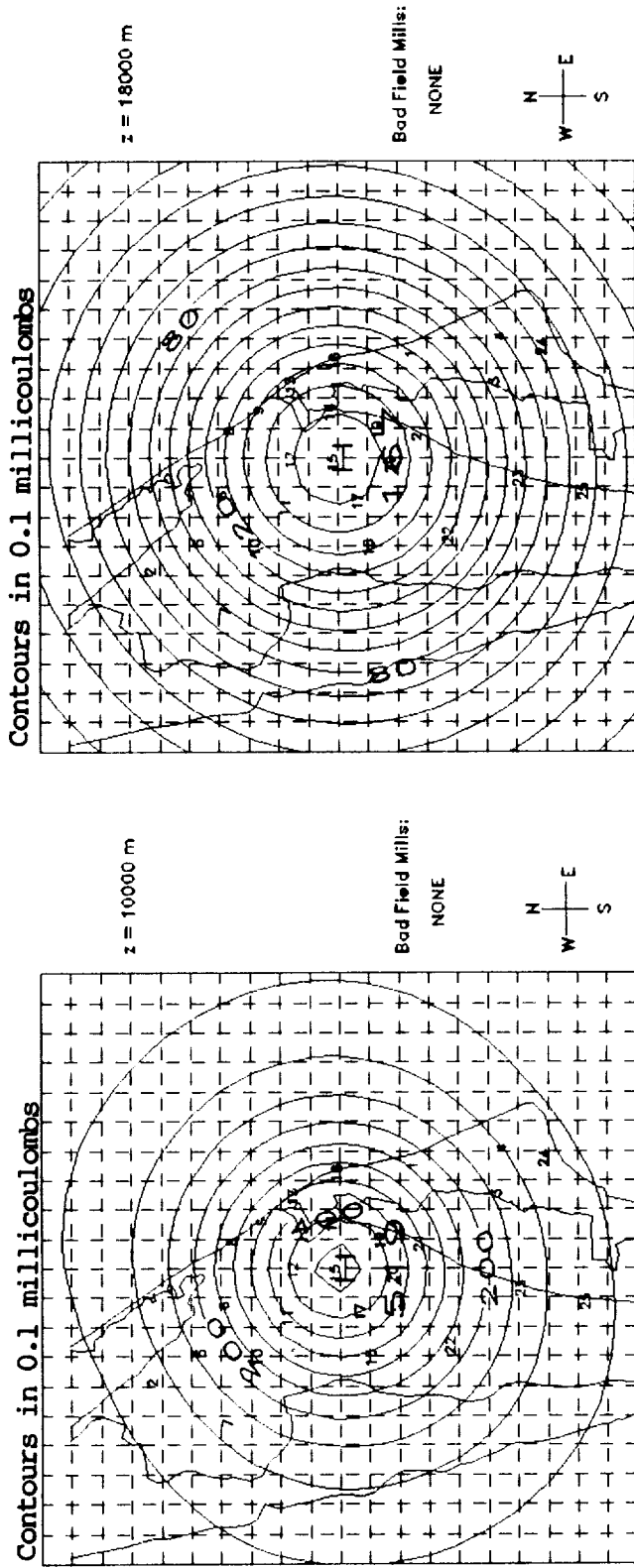


Figure 5.1 a. Plan views of solution when no kernel scaling is performed.
 Known source: (18Km, 18km, 8Km, 40C).

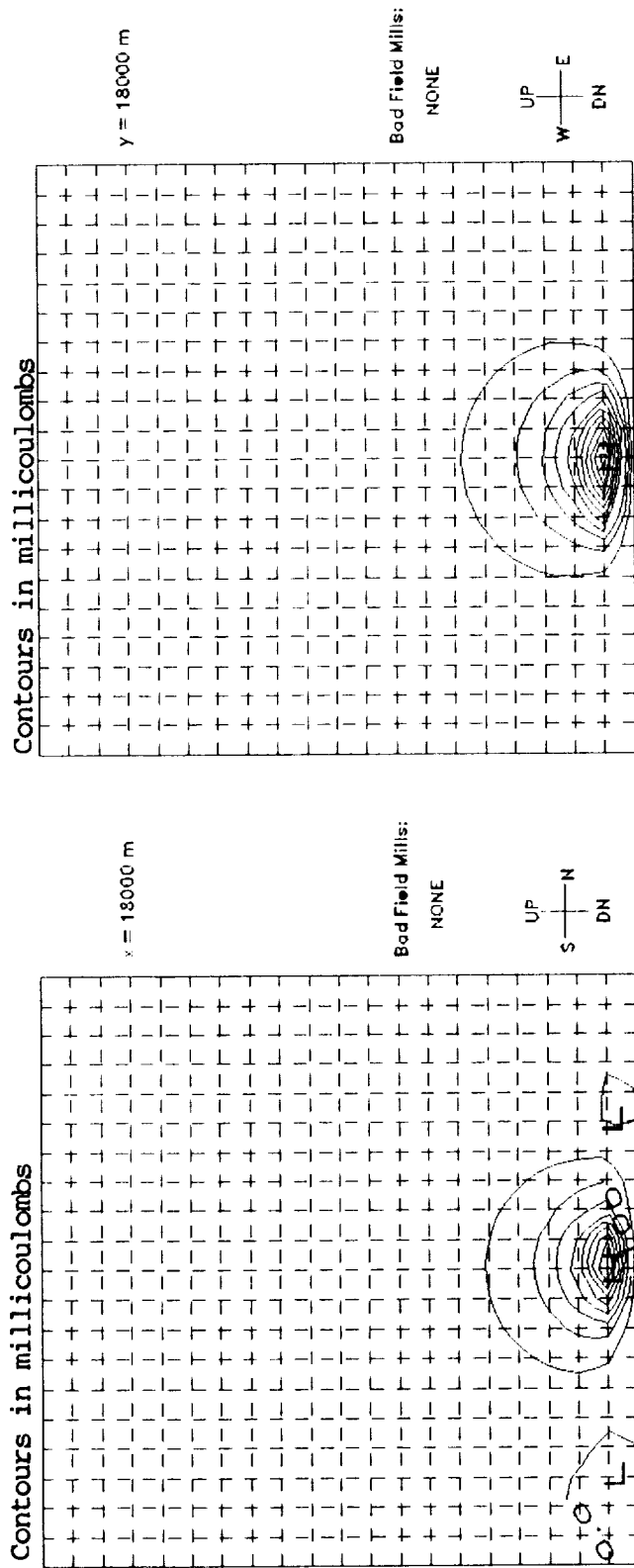


Figure 5.1b Altitude cross-sections of solution for the source described in previous figure.

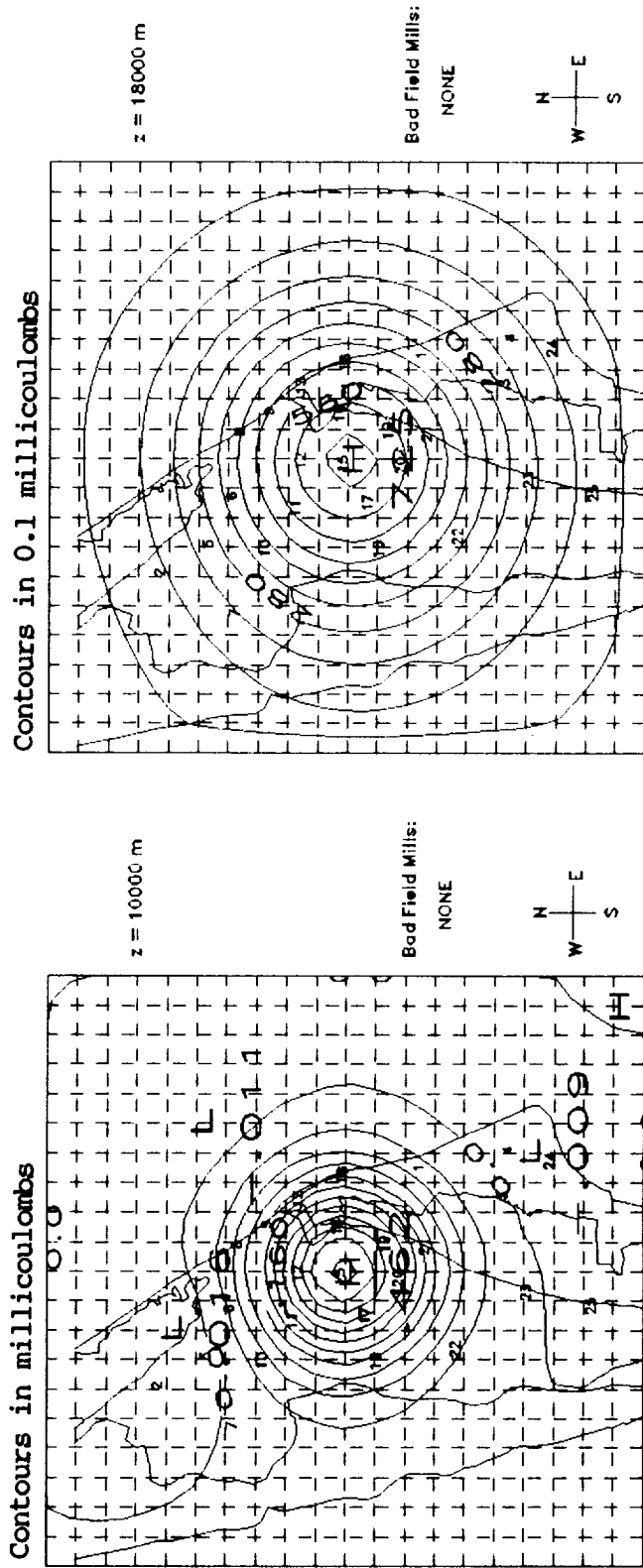


Figure 5.2a. Plan views of solution when kernel scaling is performed.
 Known source: (18Km, 18km, 8Km, 40C).

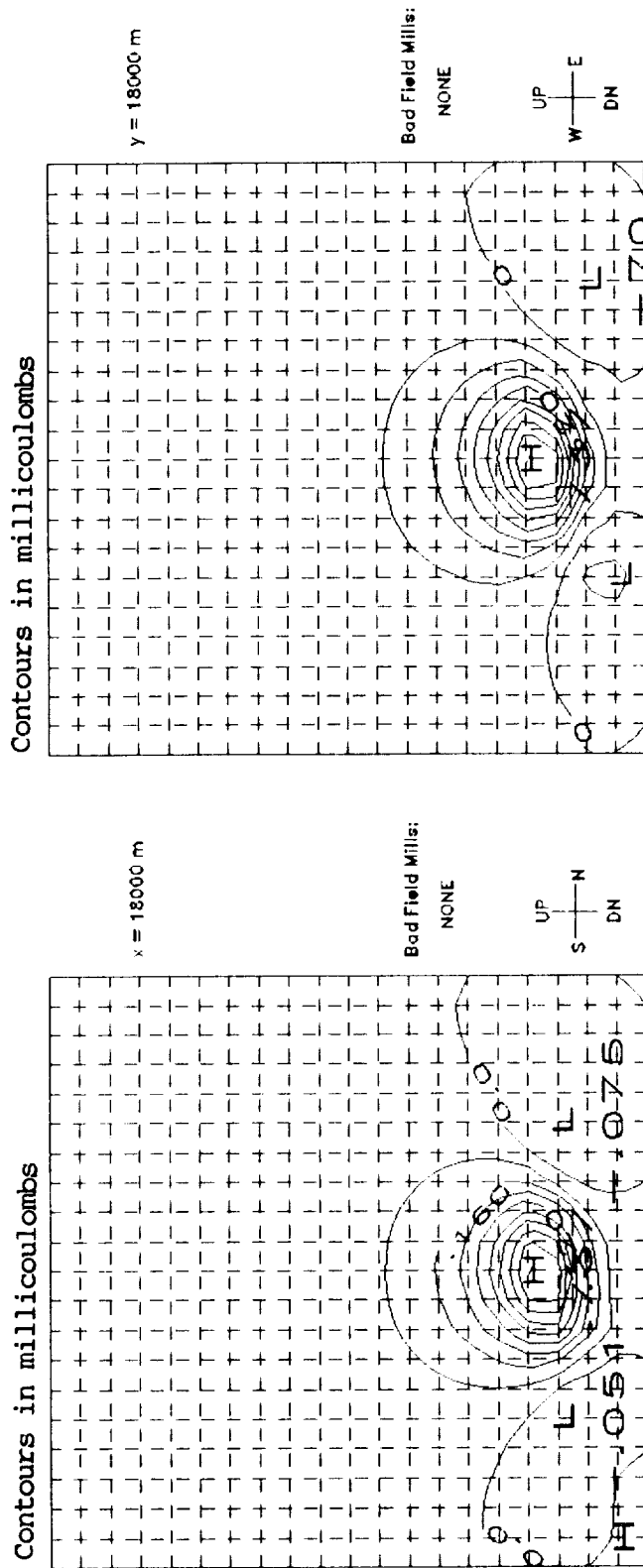


Figure 5.2 b Altitude cross-sections of solution for the source described in previous figure.

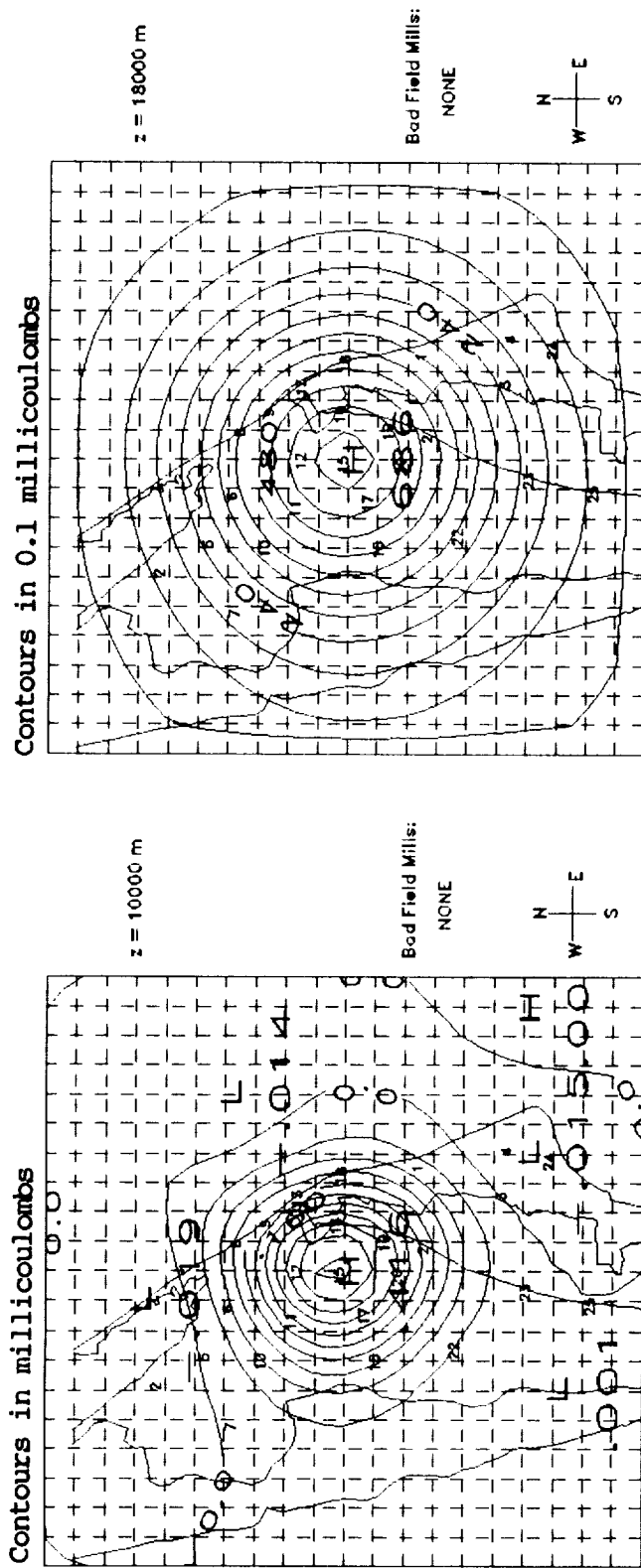


Figure 5.3a Plan views of solution when kernel scaling is performed, and measurement error is added. Known source: (18Km, 18km, 8Km, 40C).

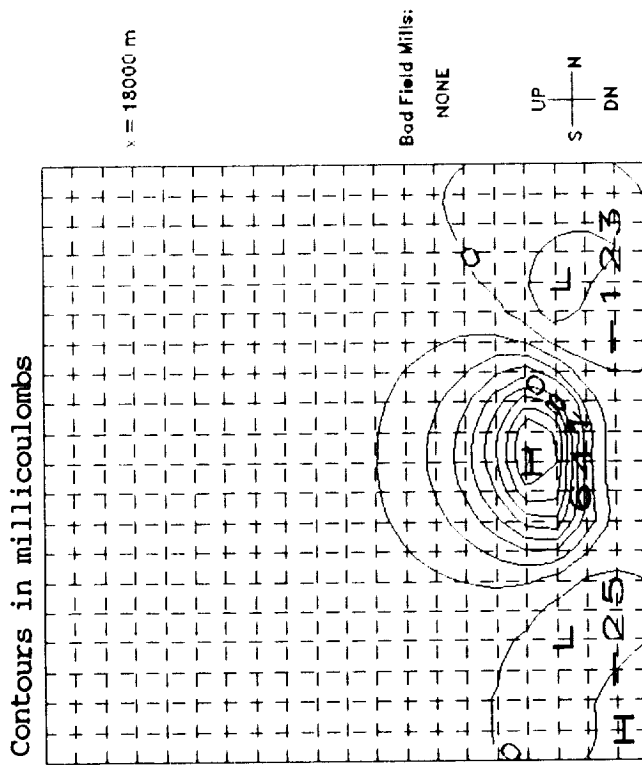
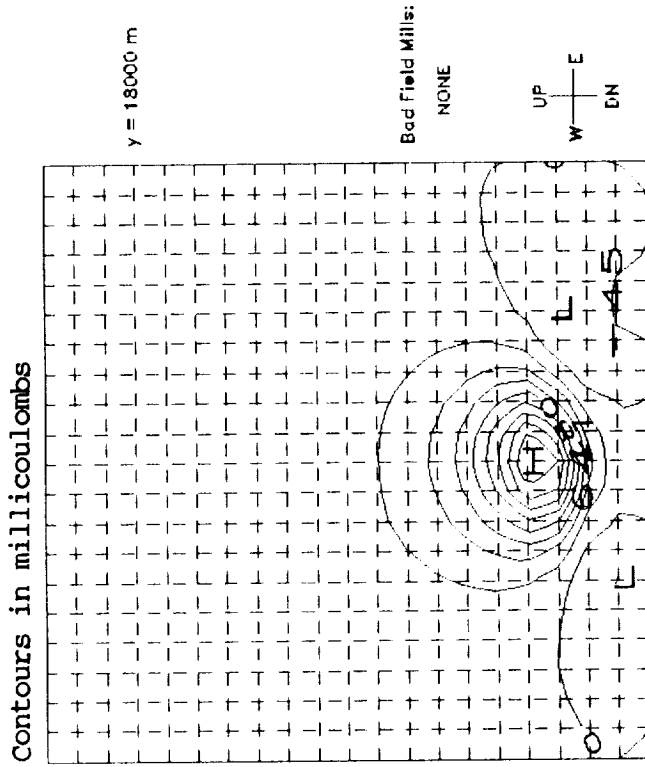


Figure 5.3b Altitude cross-sections of solution for the source described in previous figure.

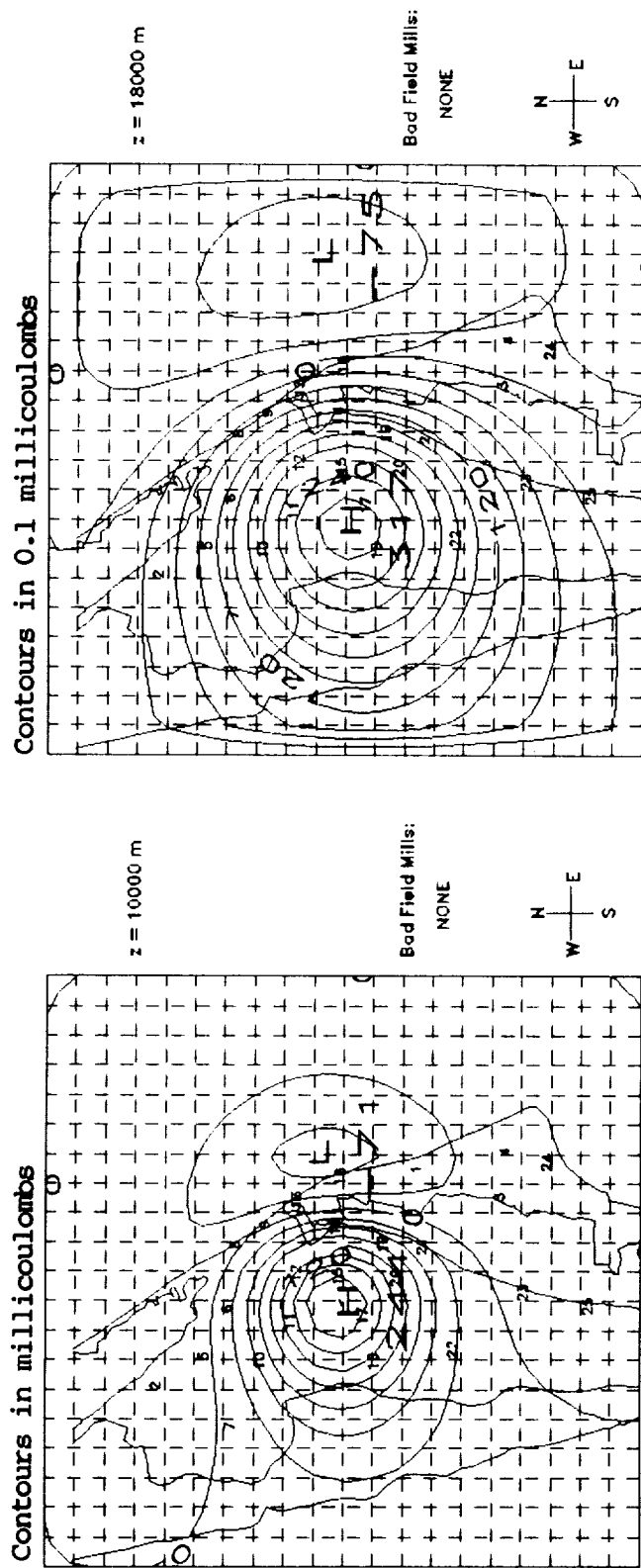


Figure 5.4a Plan views of solution. Known source: (16Km, 18km, 8Km, 40C), and (20Km, 18Km, 12Km, -40C).

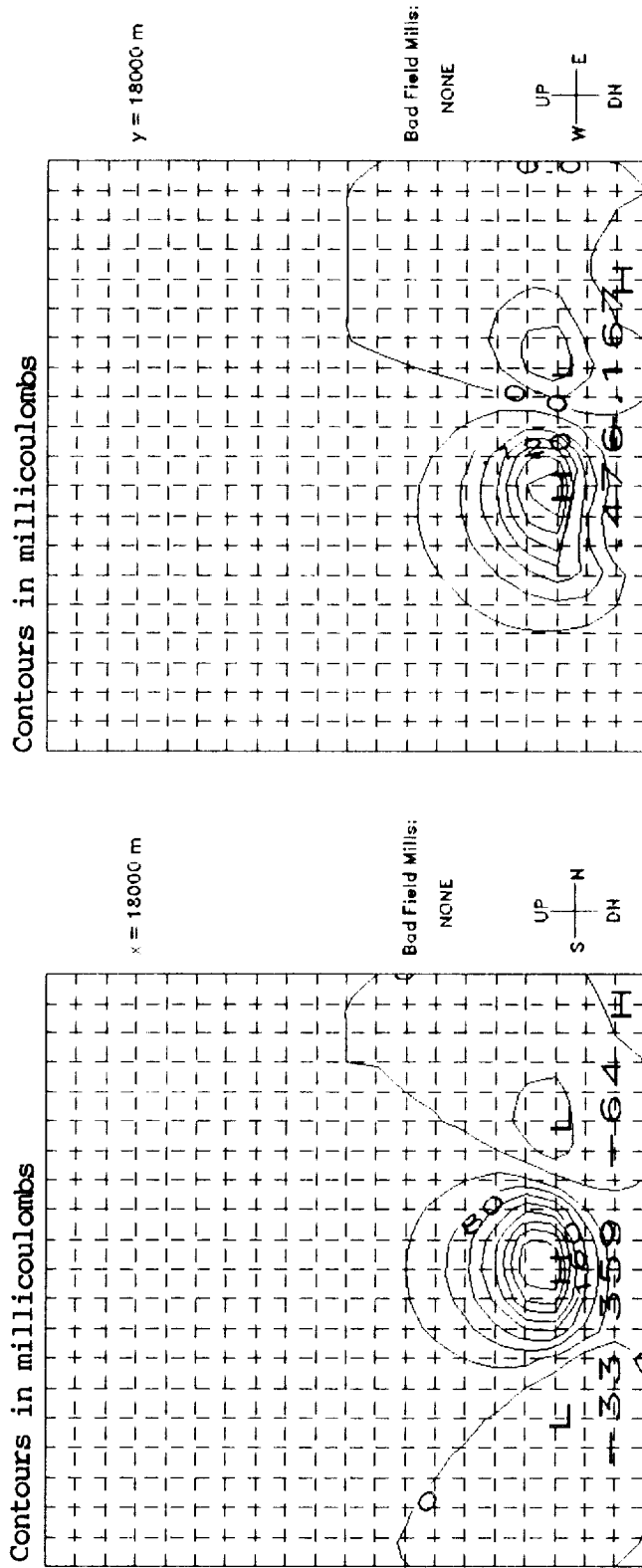


Figure 5.4b Altitude cross-sections of solution for the source described in previous figure.

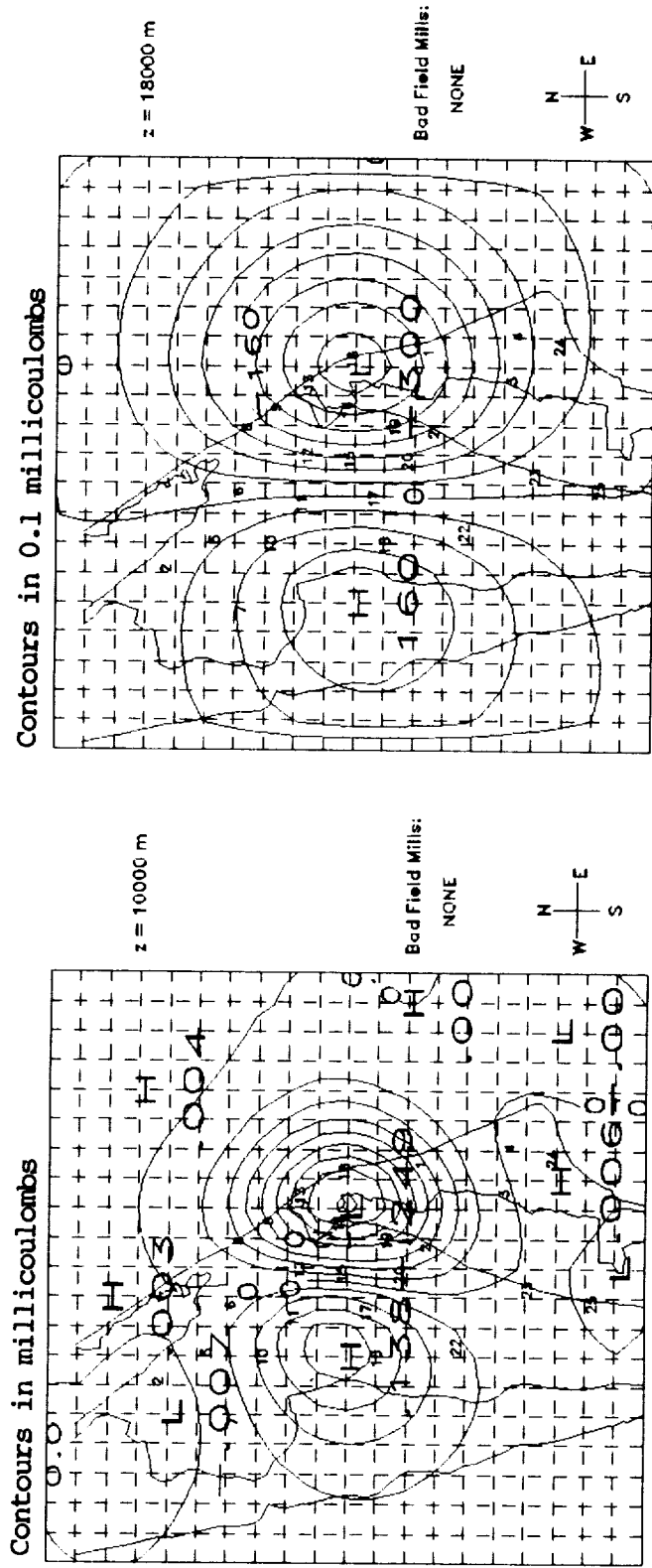


Figure 5.5a. Plan views of solution. Known source: (16Km, 18km, 8Km, 40C), and (20Km, 18Km, 8Km, -40C).

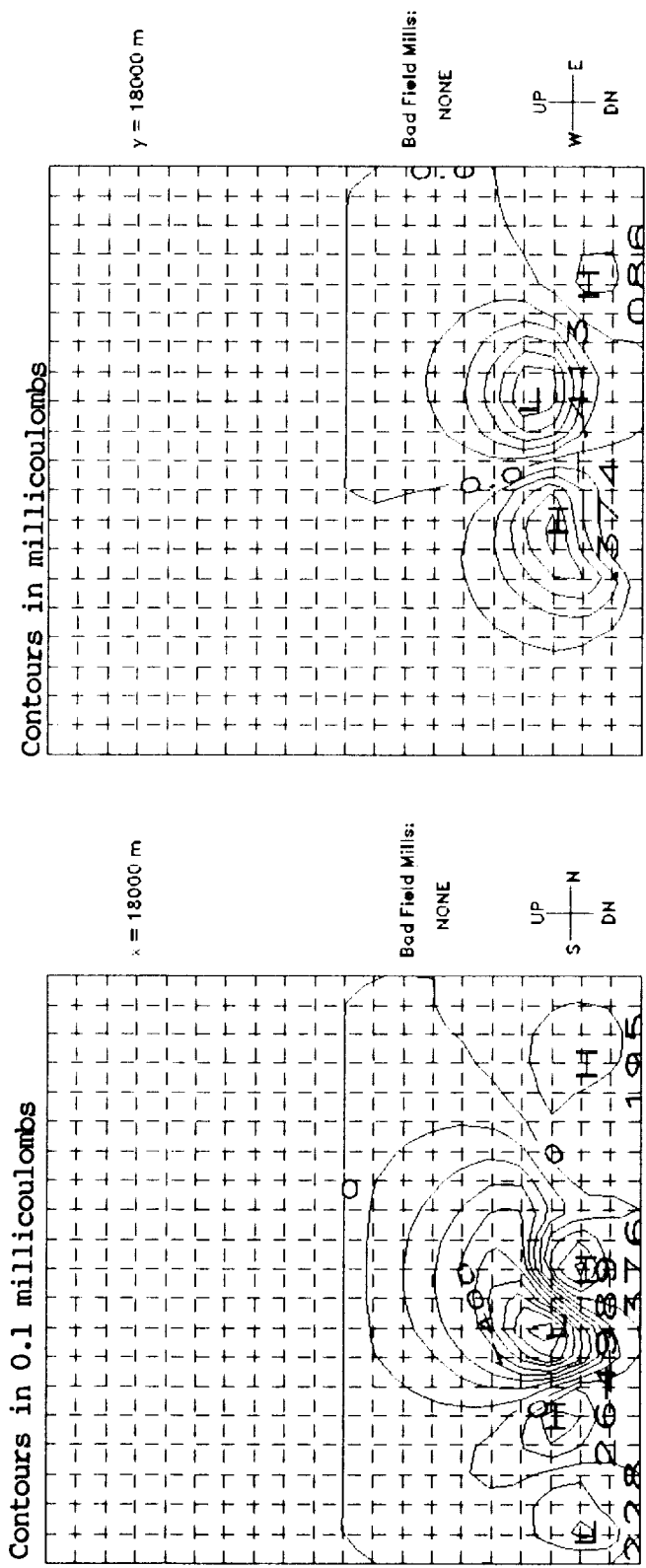


Figure 5.5b Altitude cross-sections of solution for the source described in previous figure.

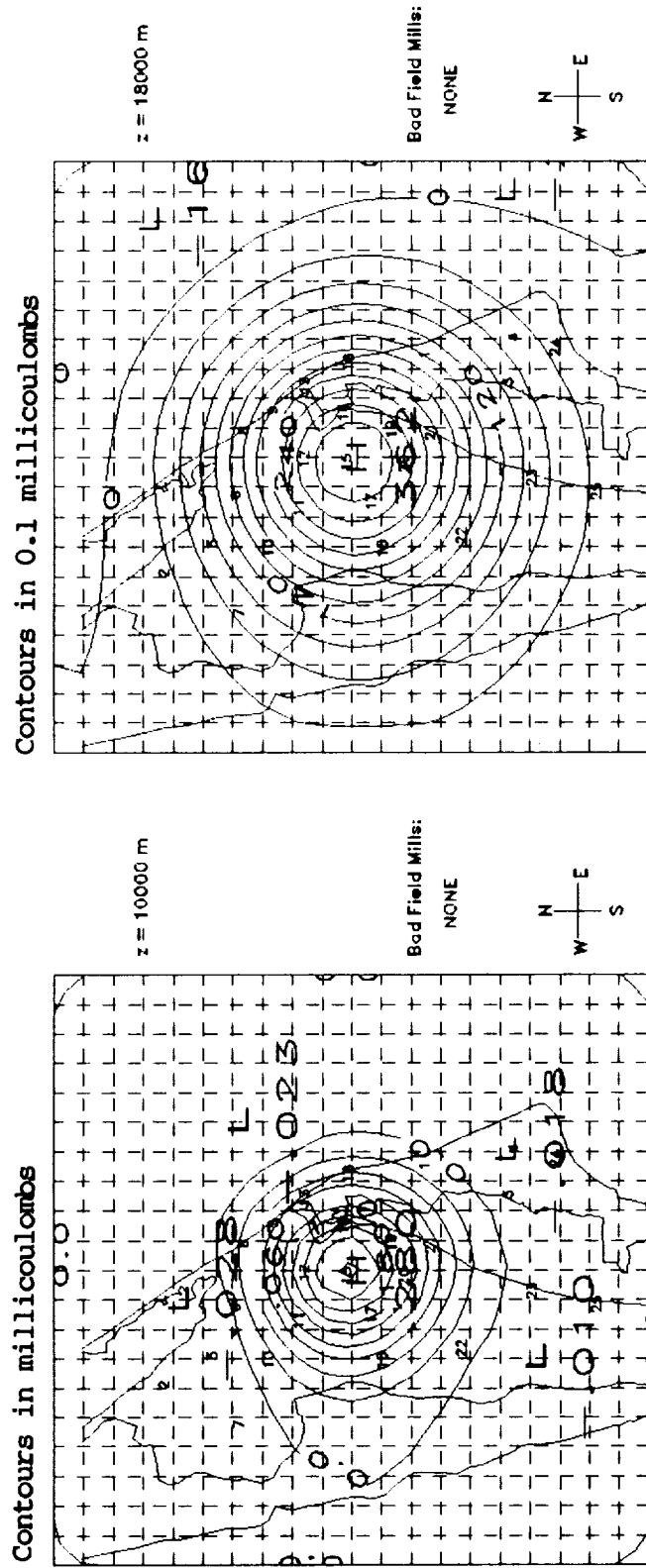


Figure 5.6a Plan views of solution. Known source: (18Km, 18km, 8Km, 40C), and (18Km, 18Km, 12Km, -40C).

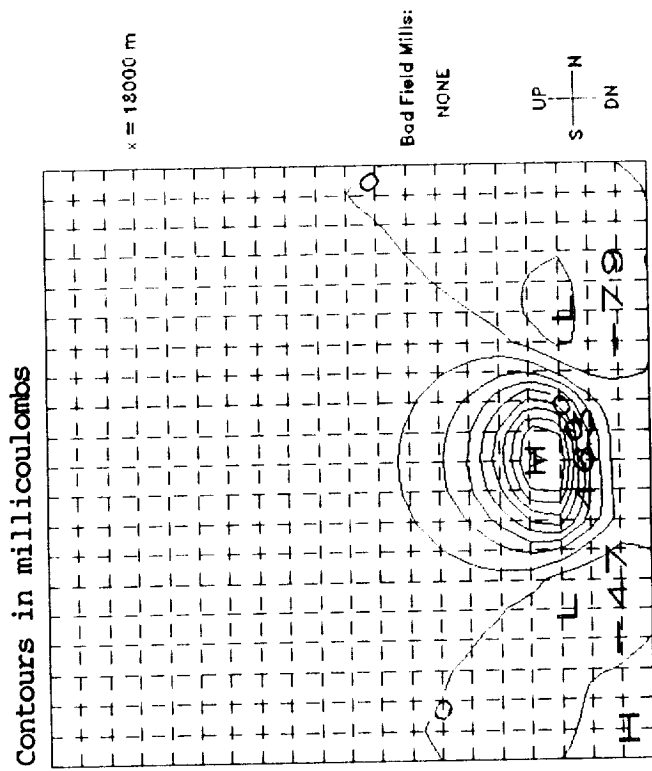
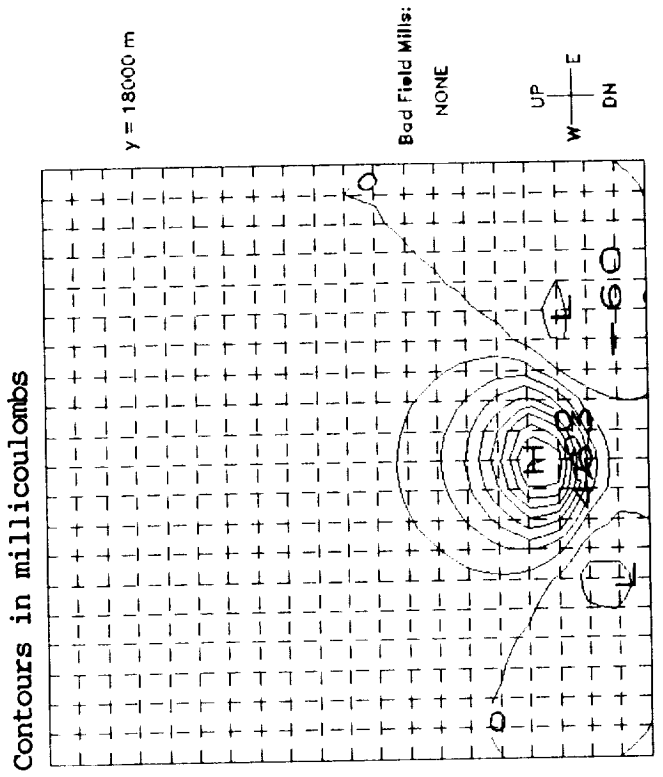


Figure 5.6b Altitude cross-sections of solution for the source described in previous figure.

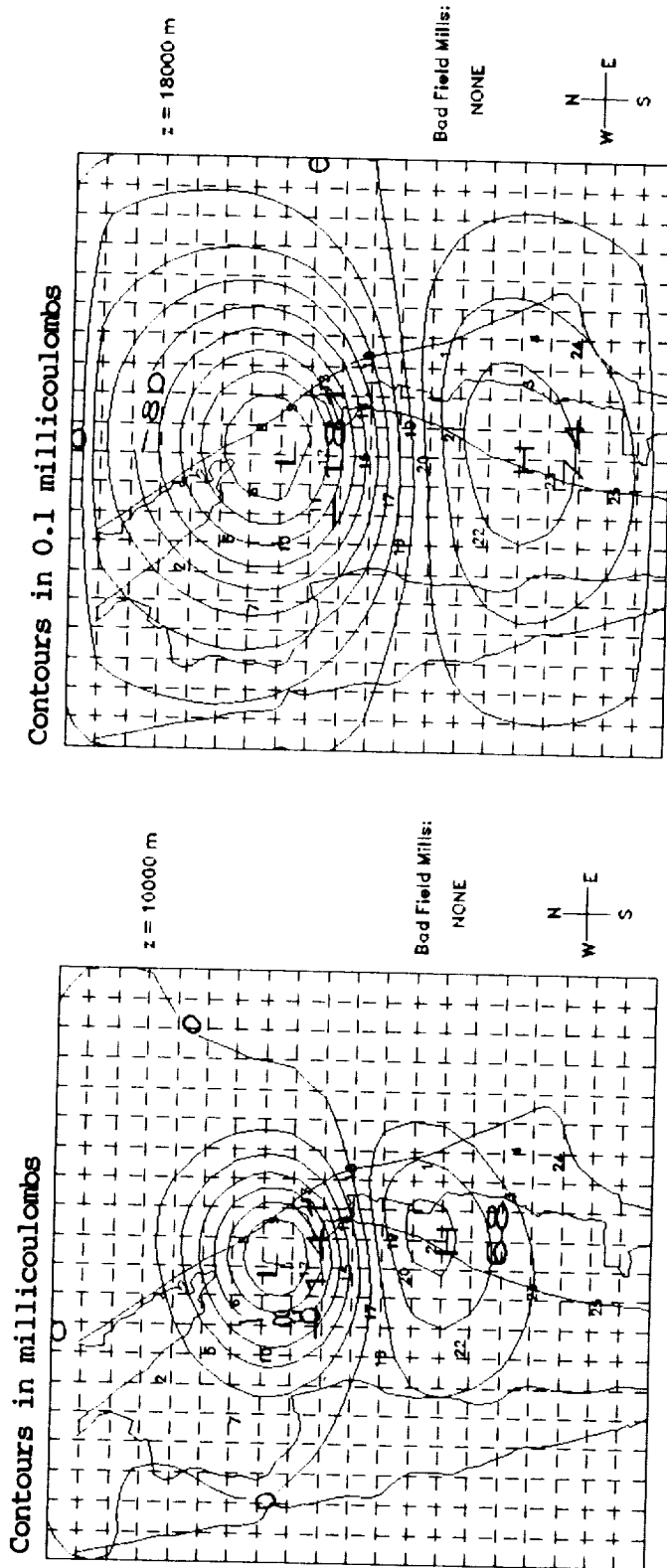


Figure 5.7a Plan views of solution. Known source: (16Km, 16Km, 10Km, 20C), (20Km, 16Km, 10Km, 20C), and (18Km, 20Km, 10Km, -40C).

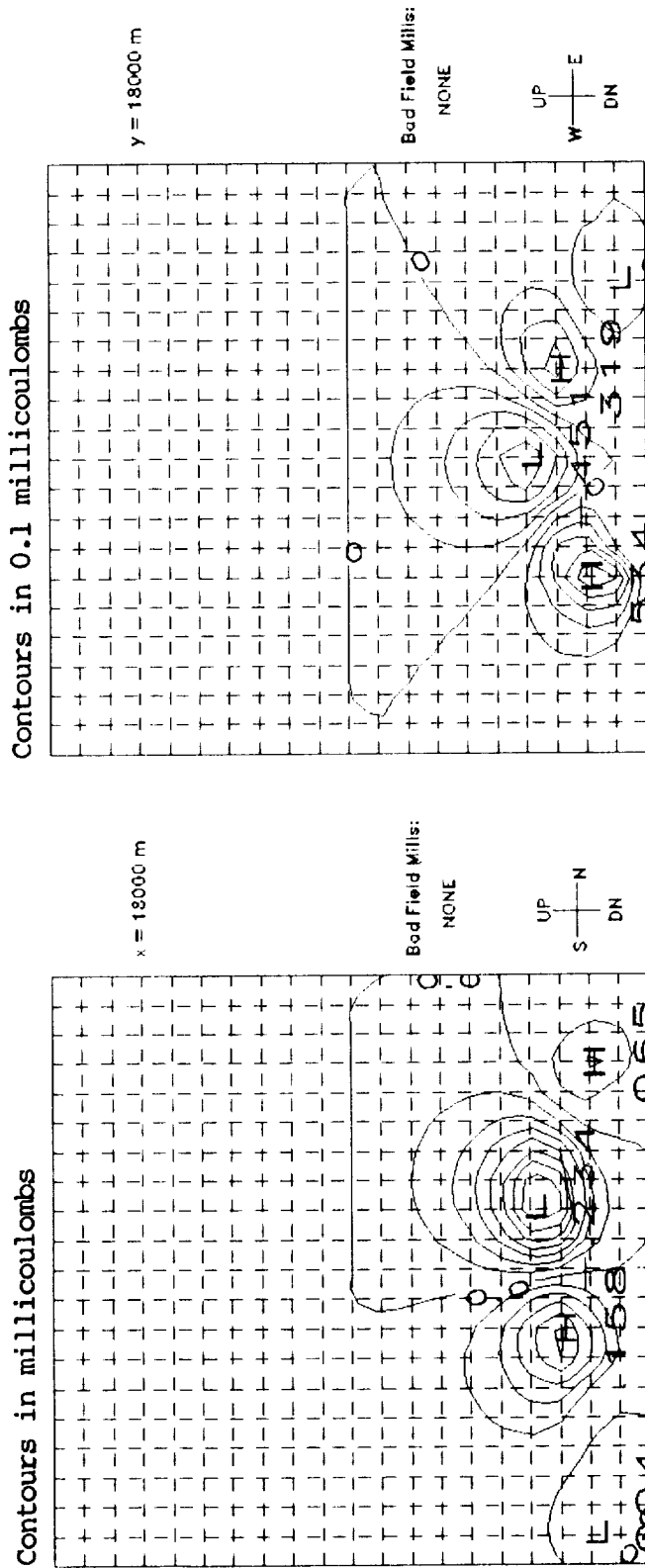


Figure 5.7b Altitude cross-sections of solution for the source described in previous figure.

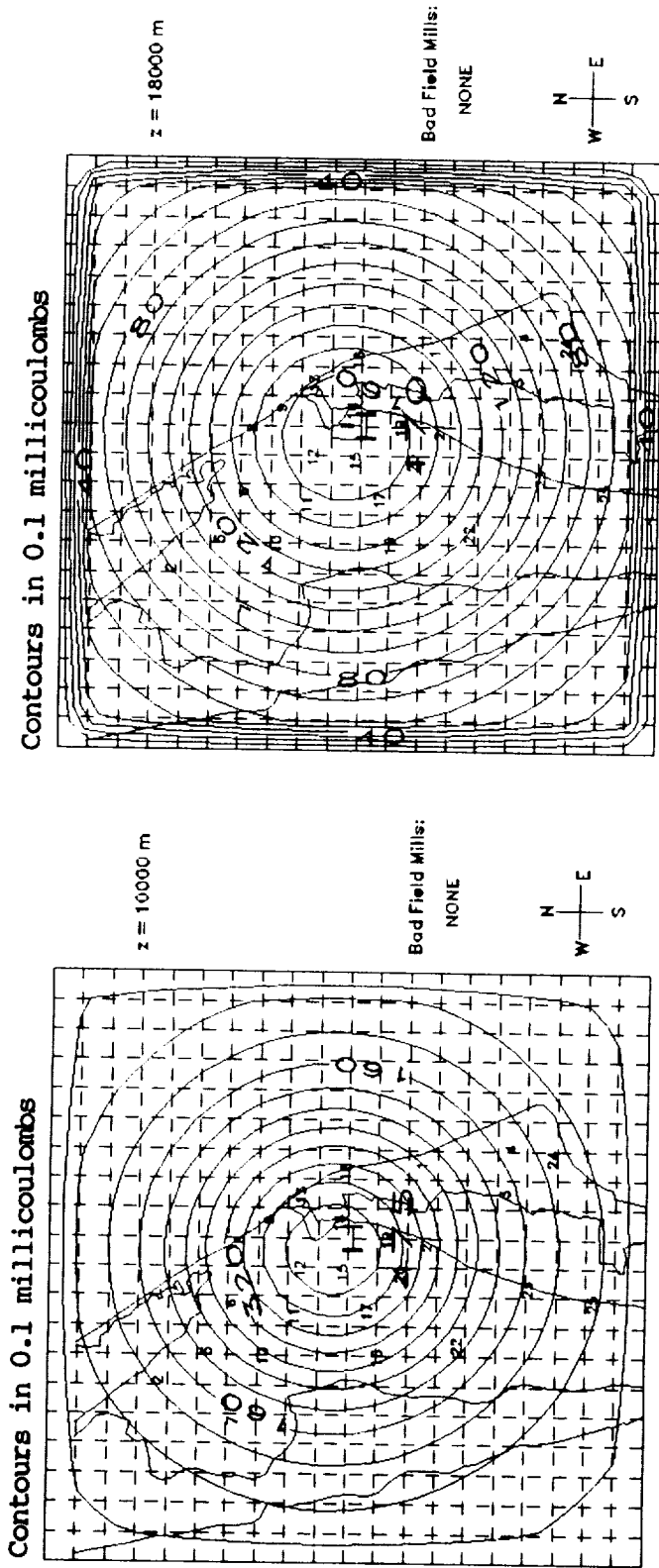


Figure 5.8a Plan views of solution. Known source: (18Km, 18km, 8Km, 40C). Maximum charge density constraint added.

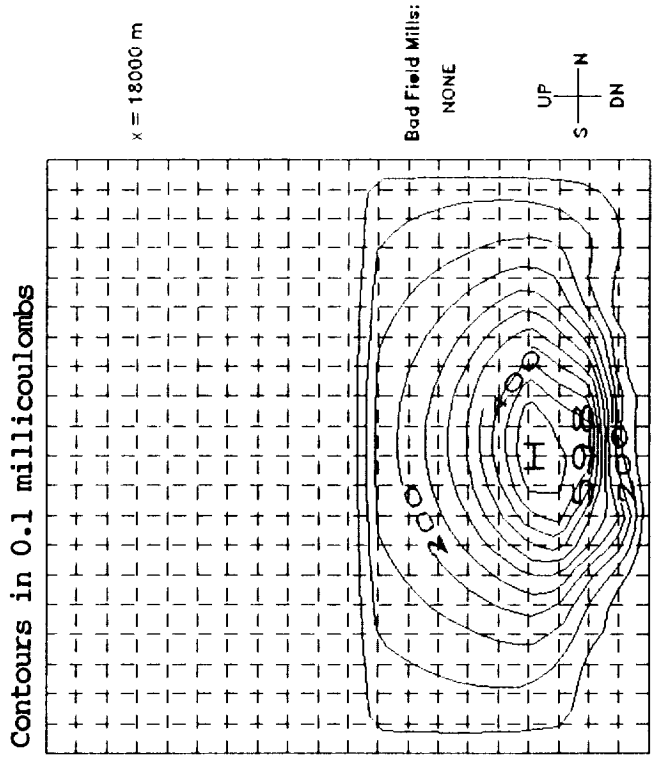
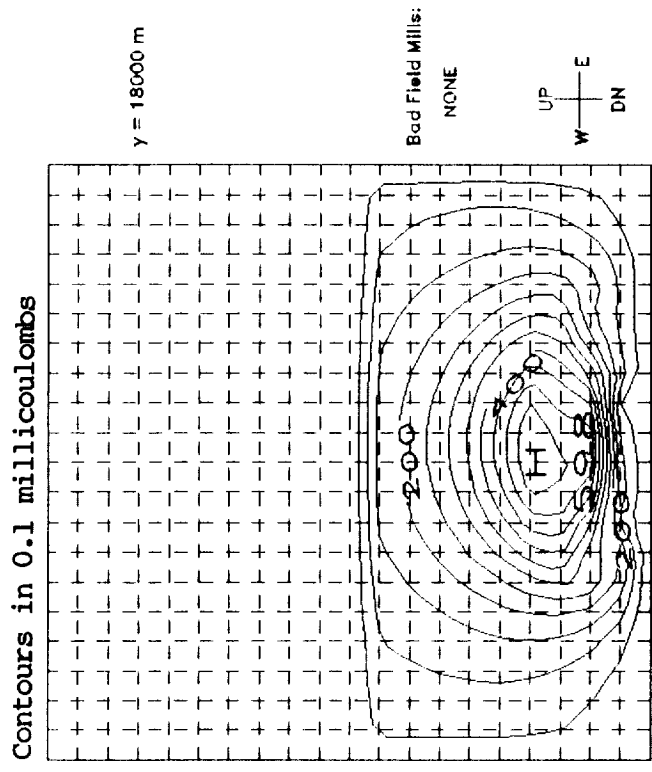


Figure 5.8b Altitude cross-sections of solution; source described in previous figure.

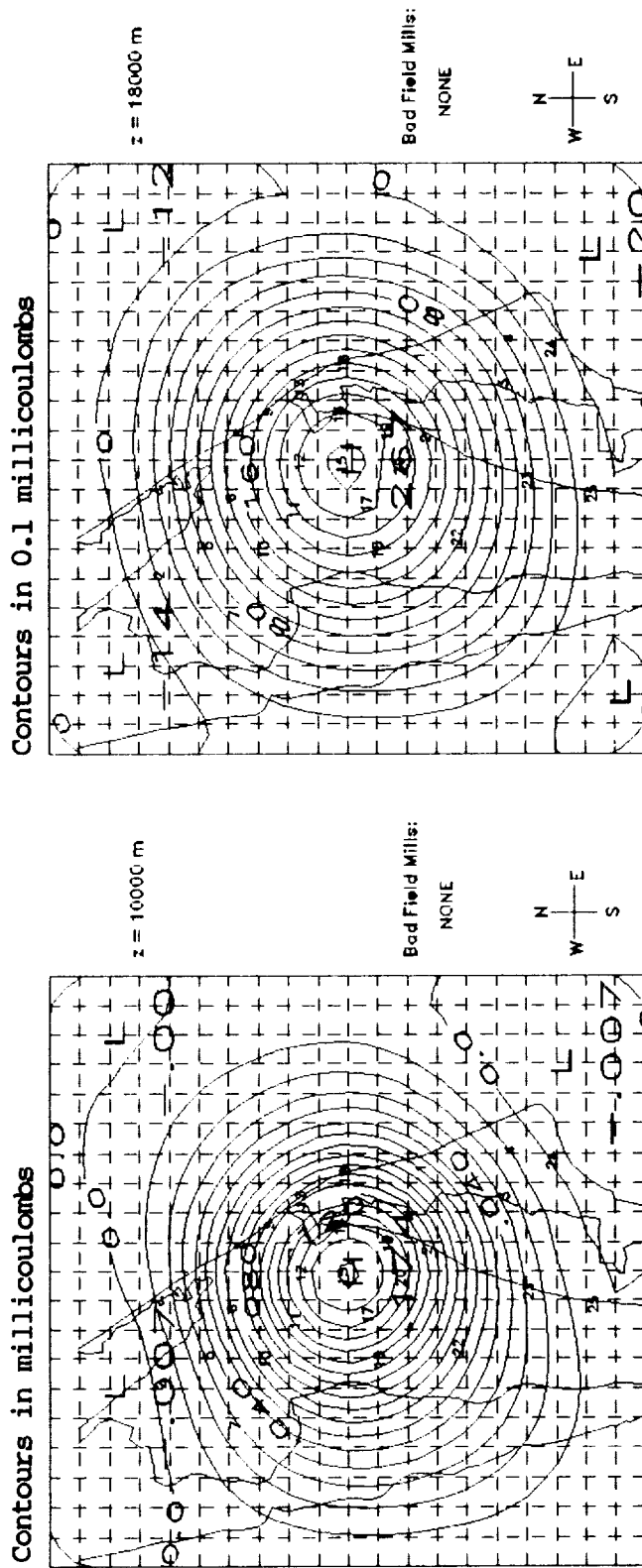


Figure 5.9a Plan views of solution. Known source: (18Km, 18km, 8Km, 40C).
Kernel scaling replaced by smoothing constraint.

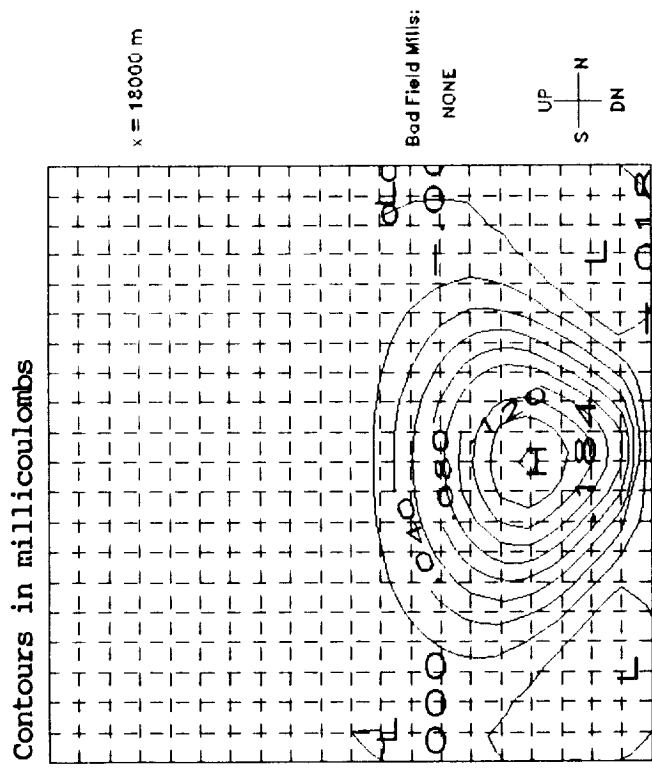
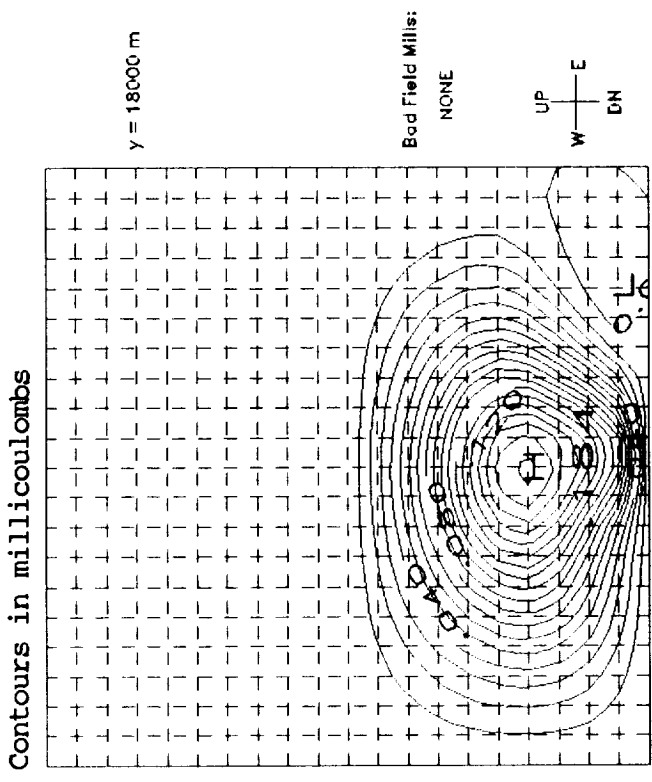


Figure 5.9b Altitude cross-sections of solution; source described in previous figure.

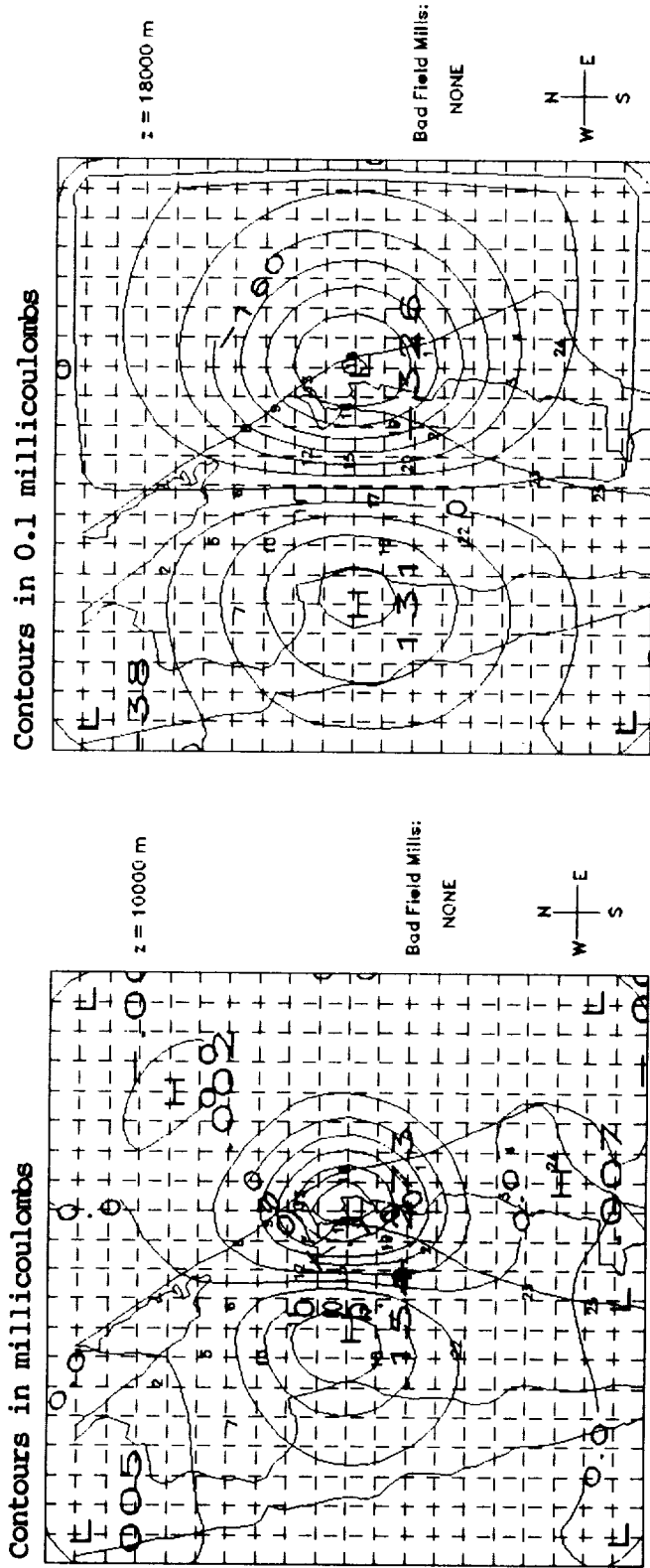


Figure 5.10a Plan views of solution. Known source: (16Km, 18km, 8Km, 40C), (20Km, 18Km, 8Km, -40C). Conservation of charge constraint added.

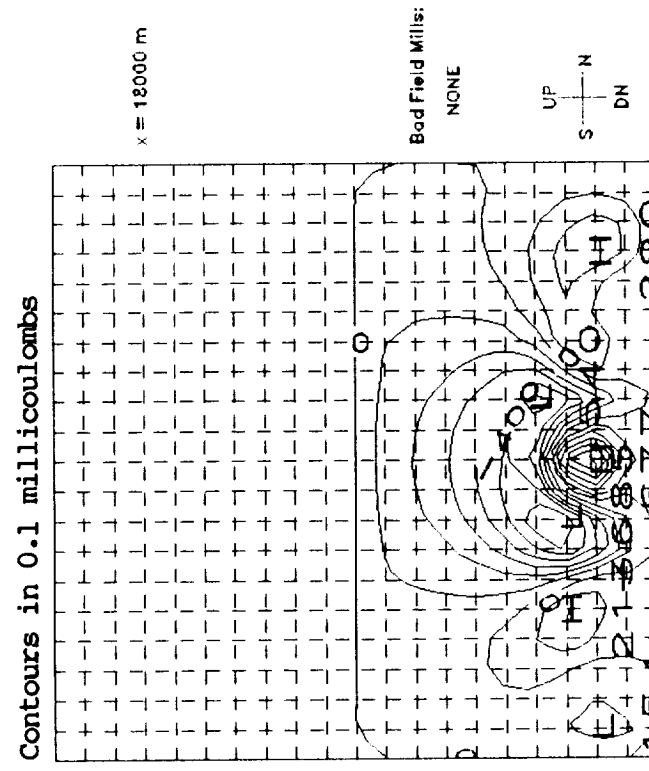
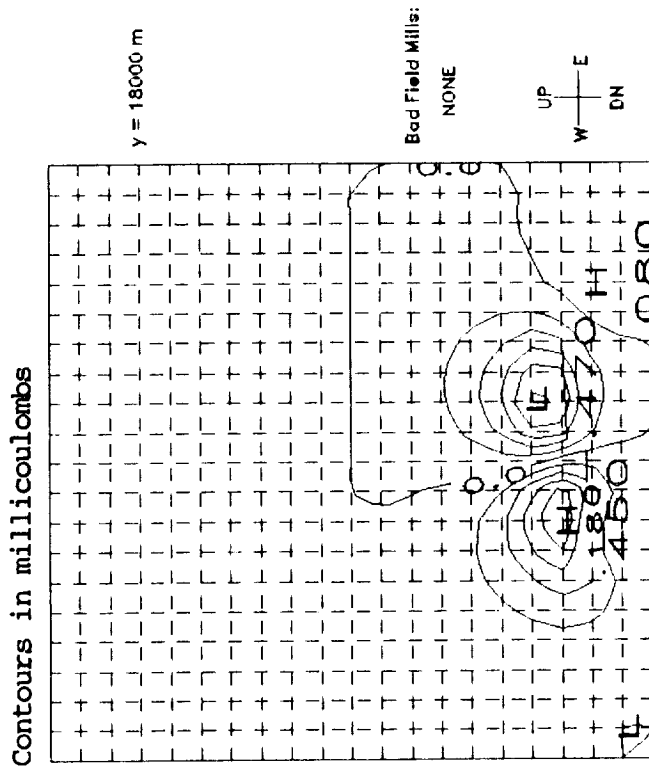


Figure 5.10b Altitude cross-sections of solution; source described in previous figure.

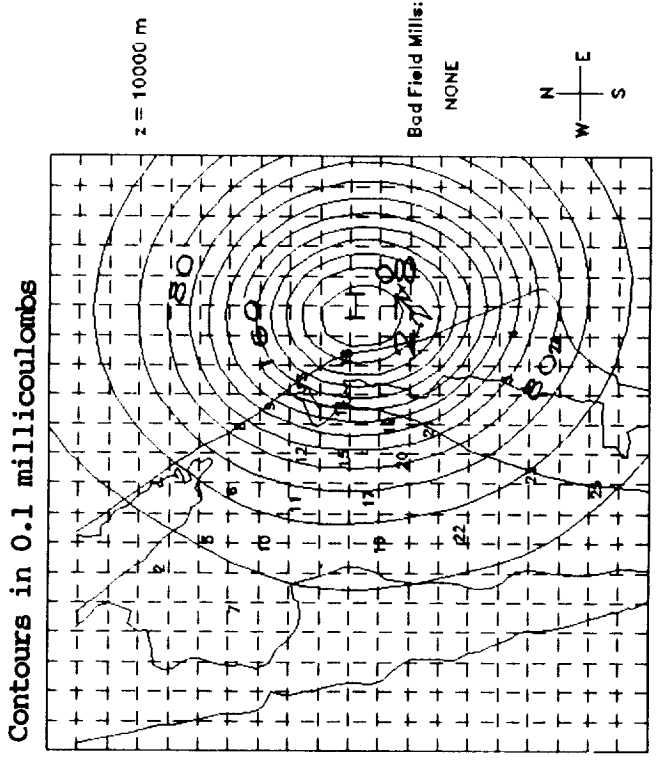
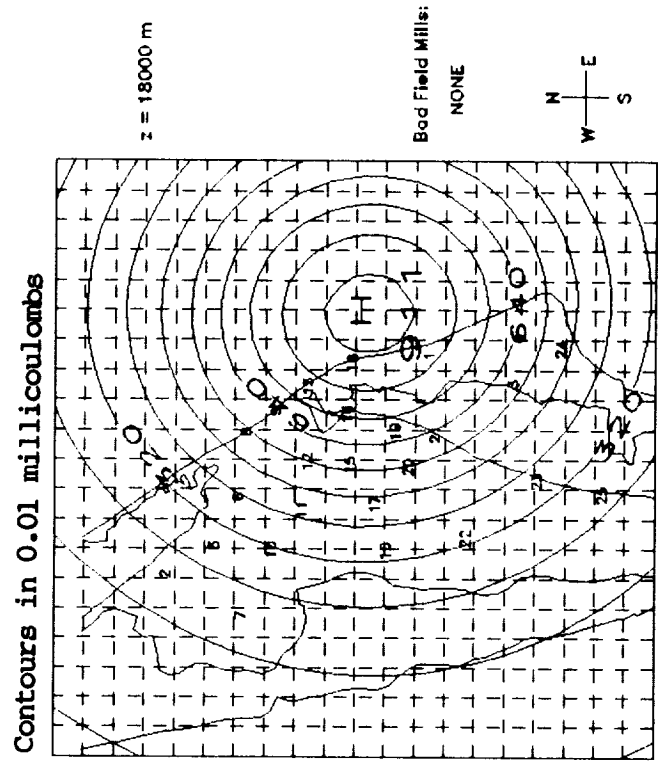


Figure 5.11a Plan views of solution. Known source: (32Km, 18Km, 8Km, 40C), No kernel scaling performed.

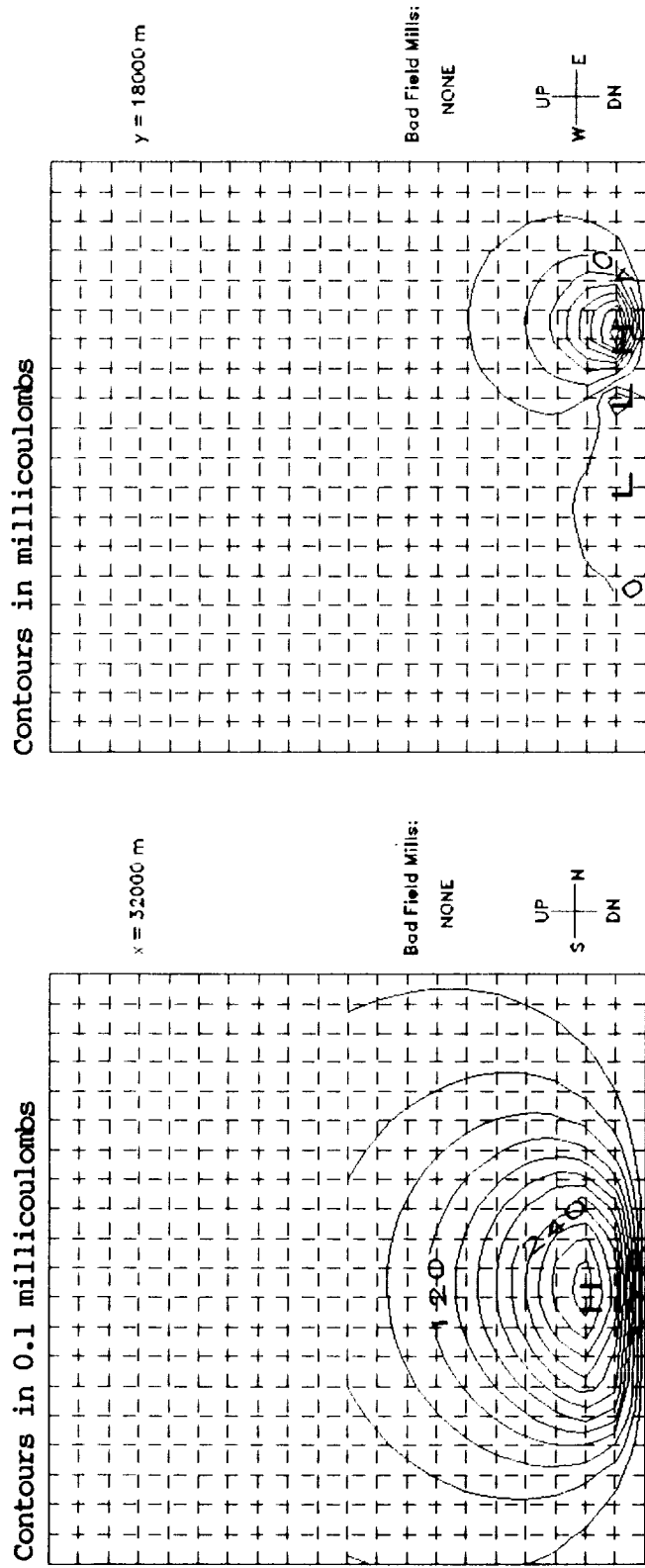


Figure 5.11b Altitude cross-sections of solution for the source described in previous figure.

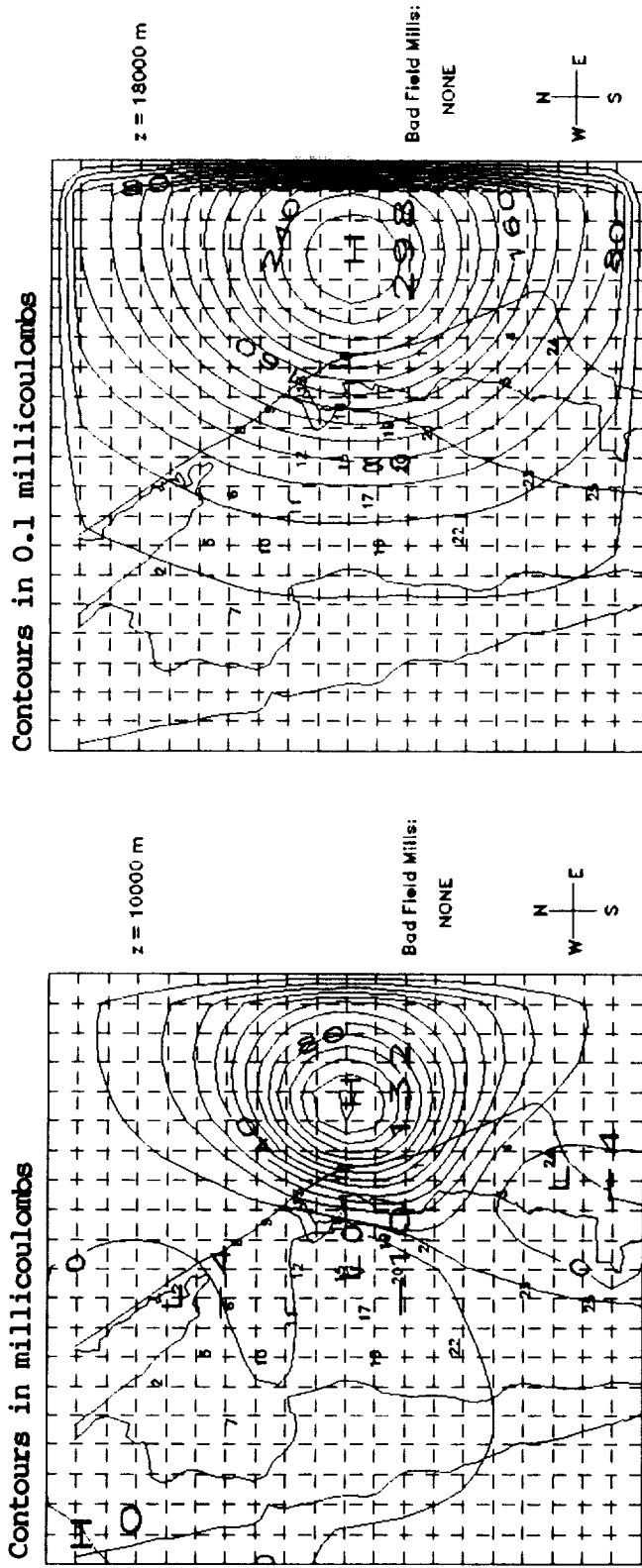


Figure 5.12a. Plan views of solution. Known source: (32Km, 18Km, 8Km, 40C), Kernel scaling performed.

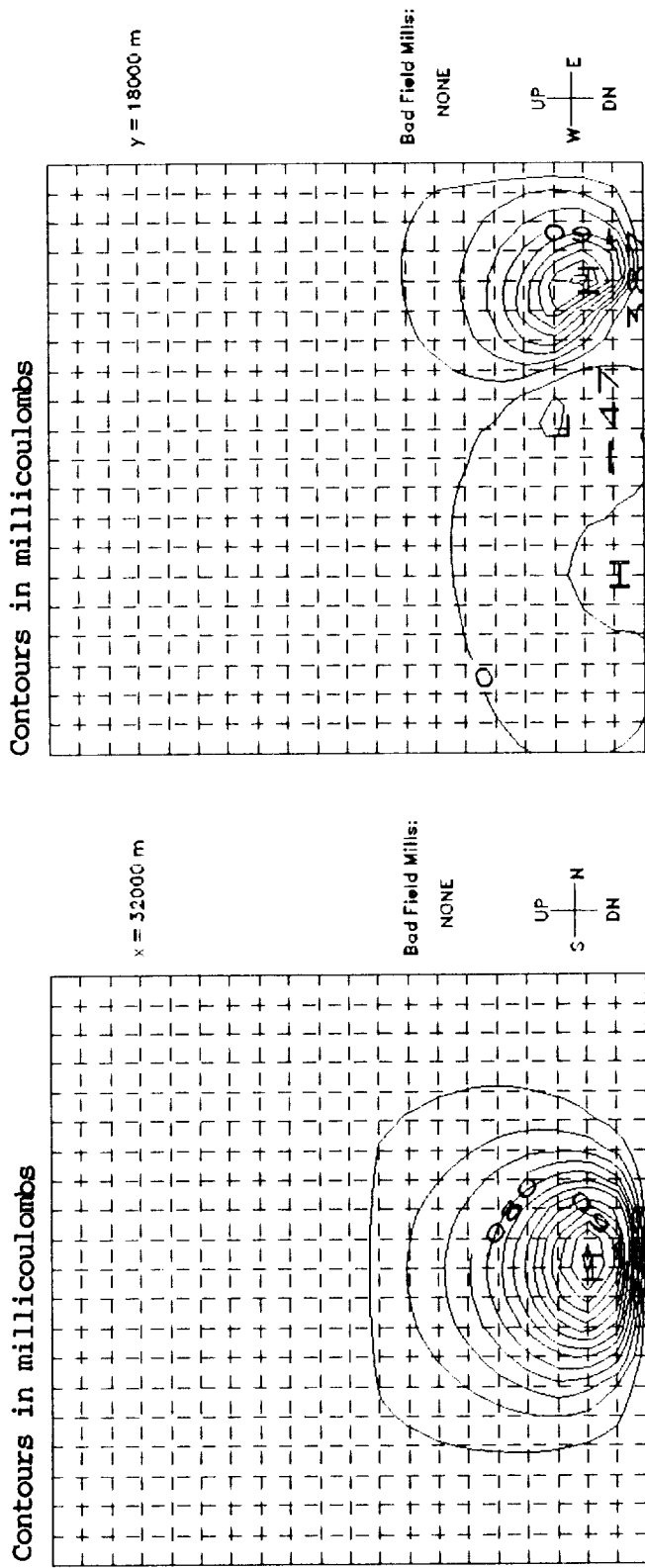


Figure 5.12b Altitude cross-sections of solution for the source described in previous figure.

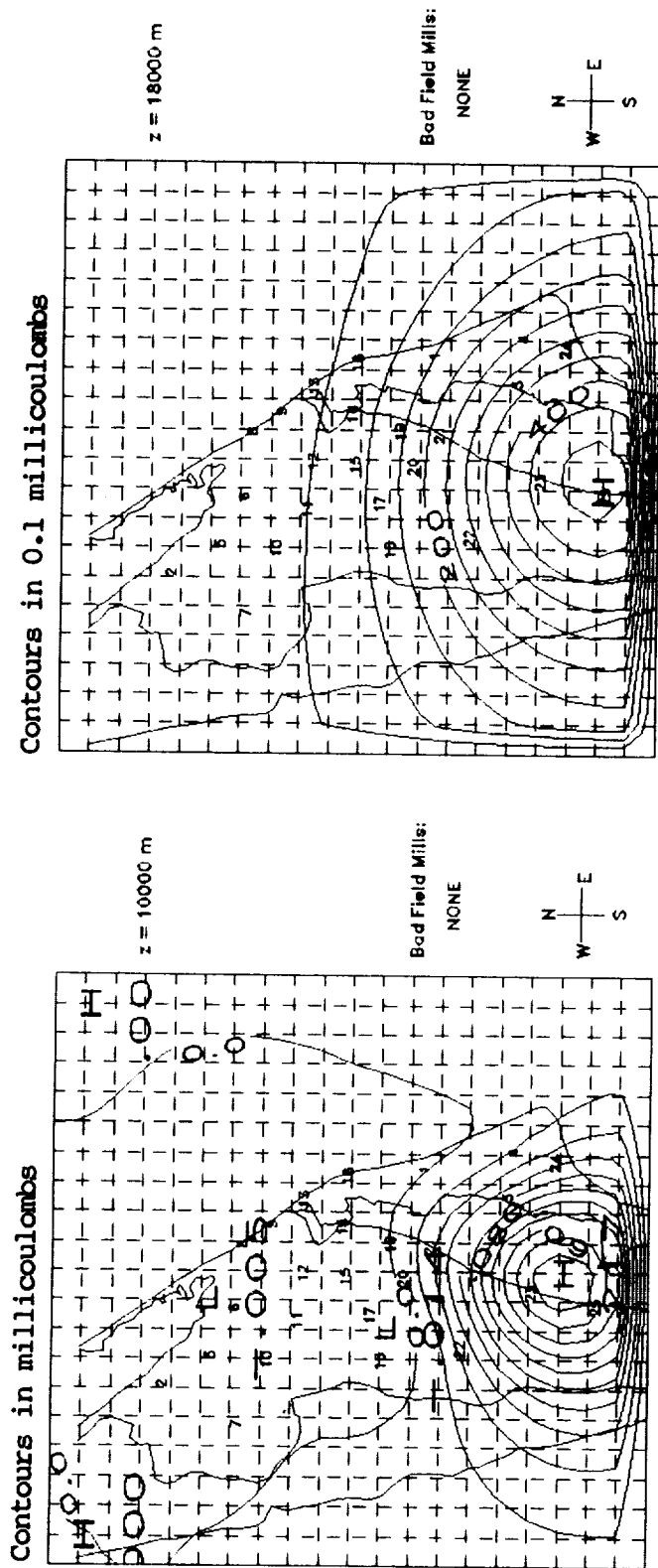


Figure 5.13a Plan views of solution. Known source: (18Km, 4Km, 8Km, 40C), Kernel scaling performed.

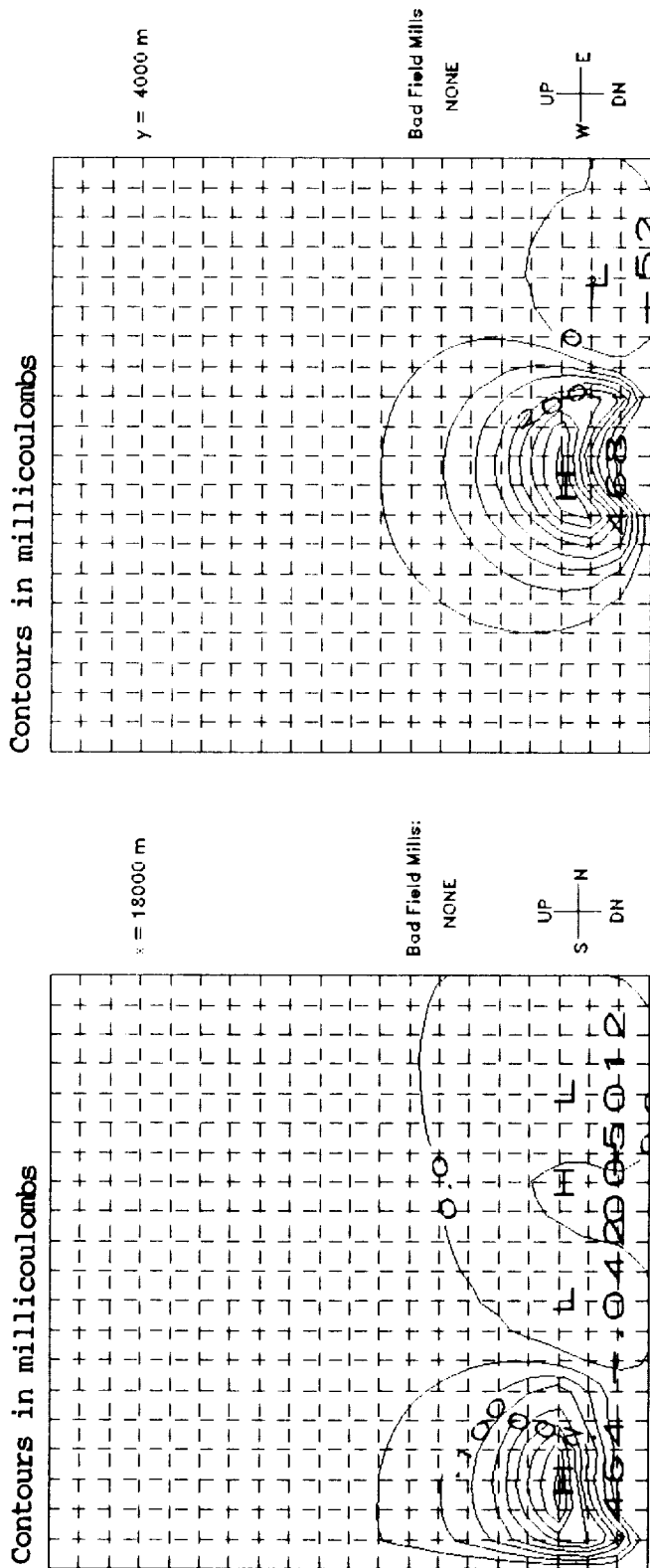


Figure 5.13b Altitude cross-sections of solution for the source described in previous figure.

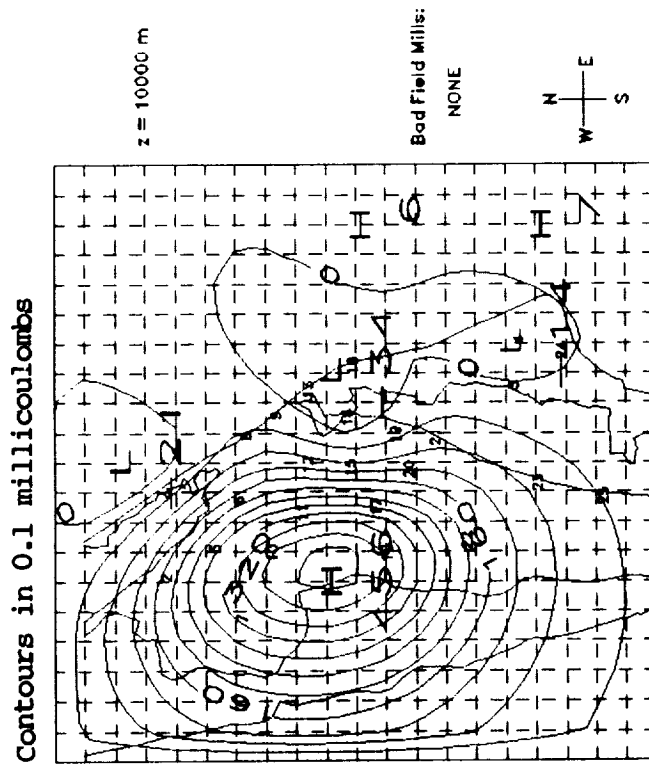
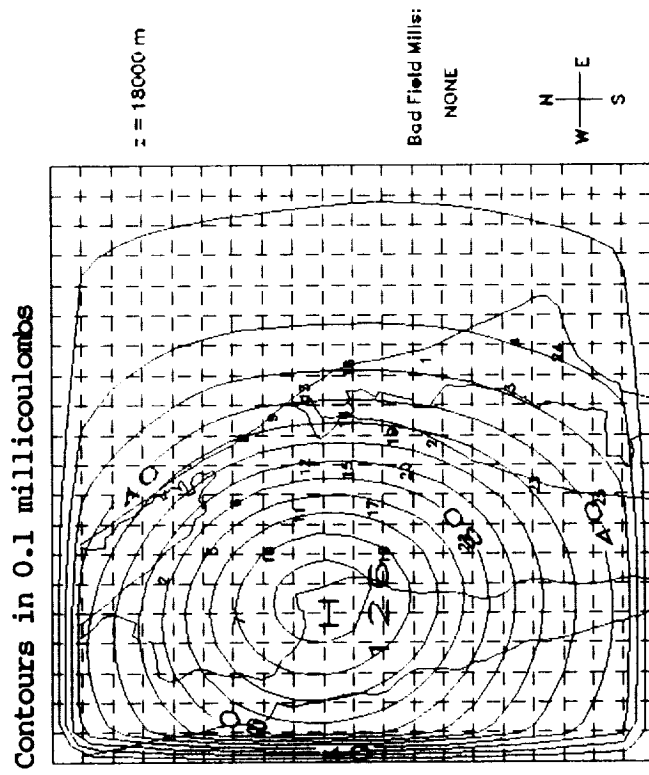


Figure 5.14a Plan views of solution. Known source: (4Km, 18Km, 8Km, 40C).
Kernel scaling performed.

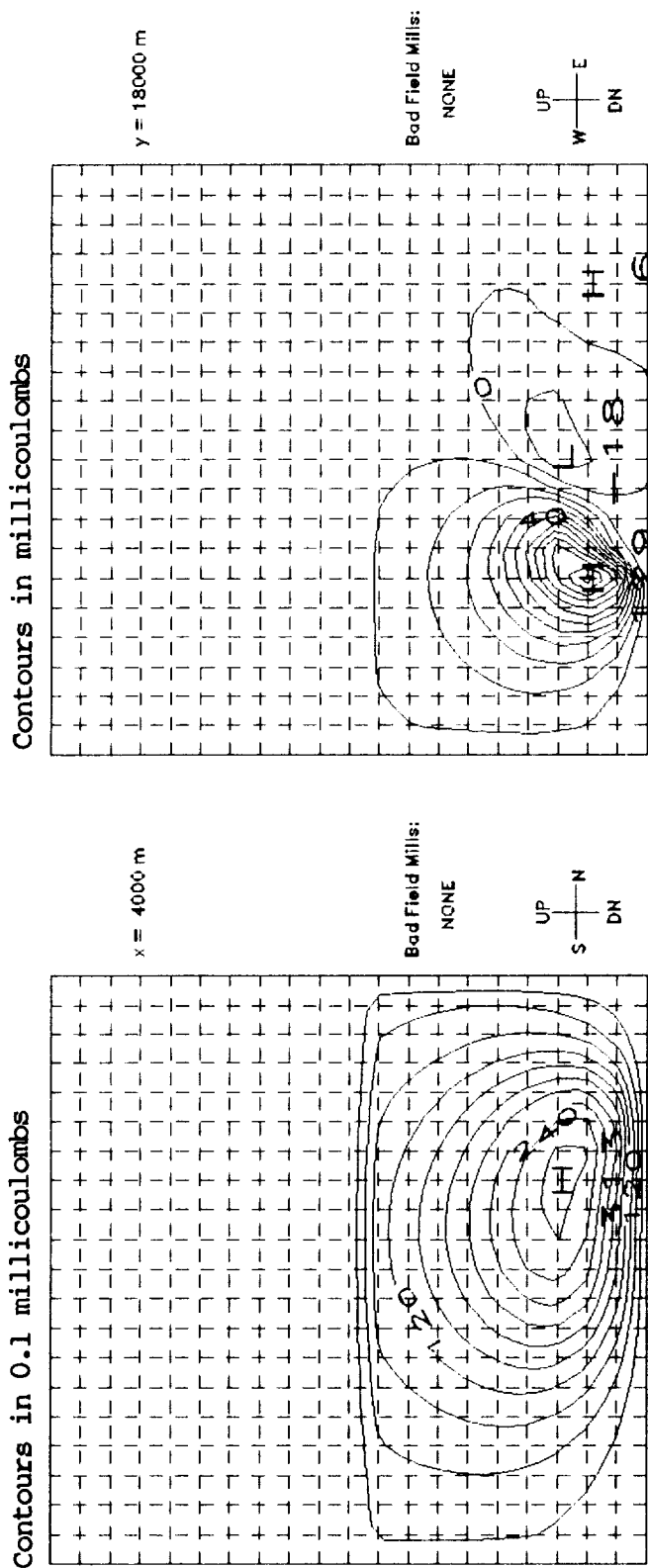


Figure 5.14b Altitude cross-sections of solution for the source described in previous figure.

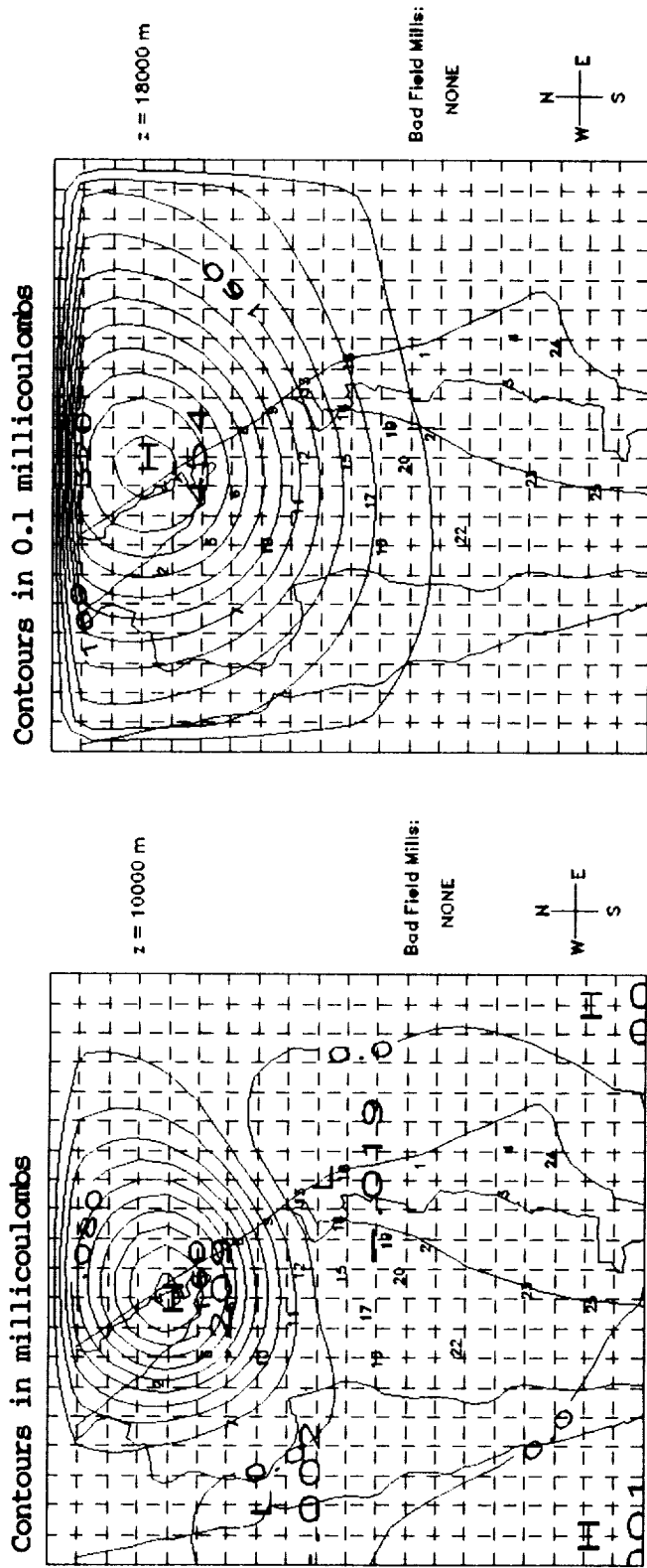


Figure 5.15a Plan views of solution. Known source: (18Km, 32Km, 8Km, 40C).
Kernel scaling performed.

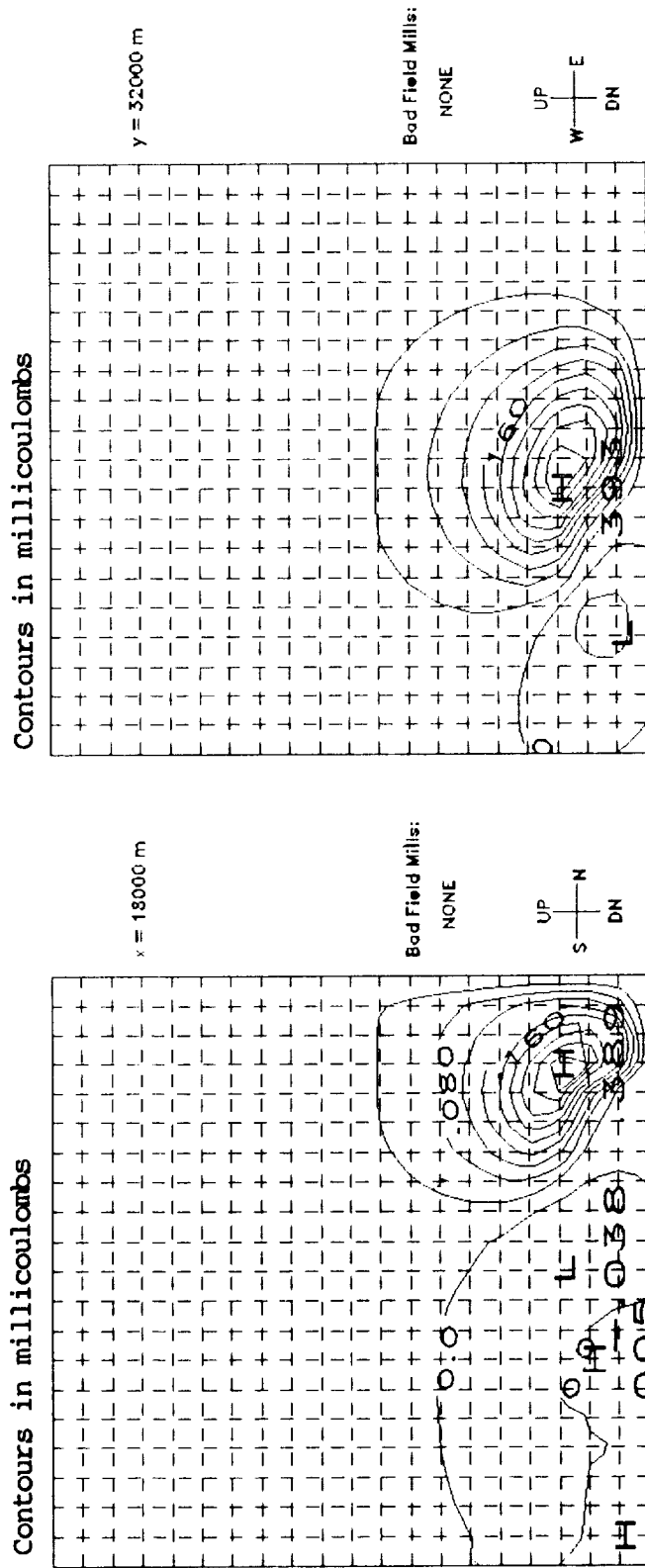


Figure 5.15b Altitude cross-sections of solution for the source described in previous figure.

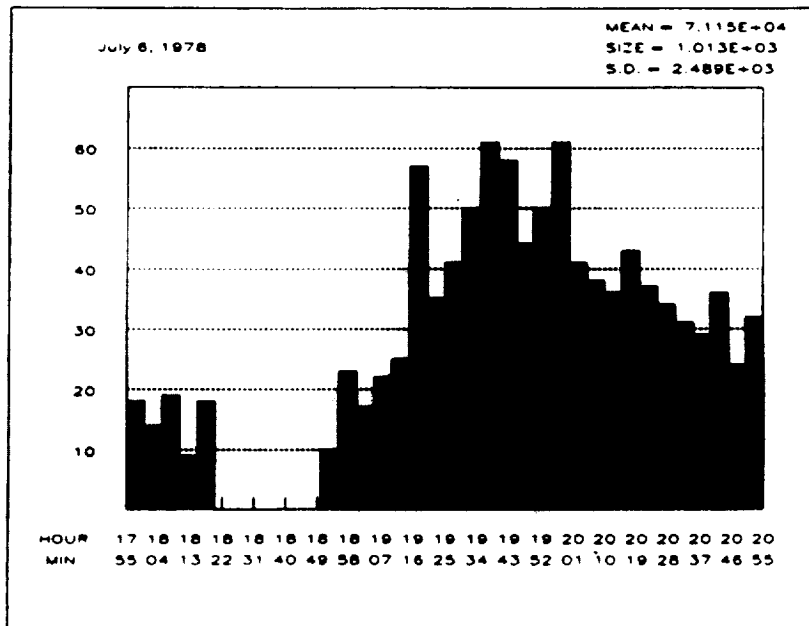
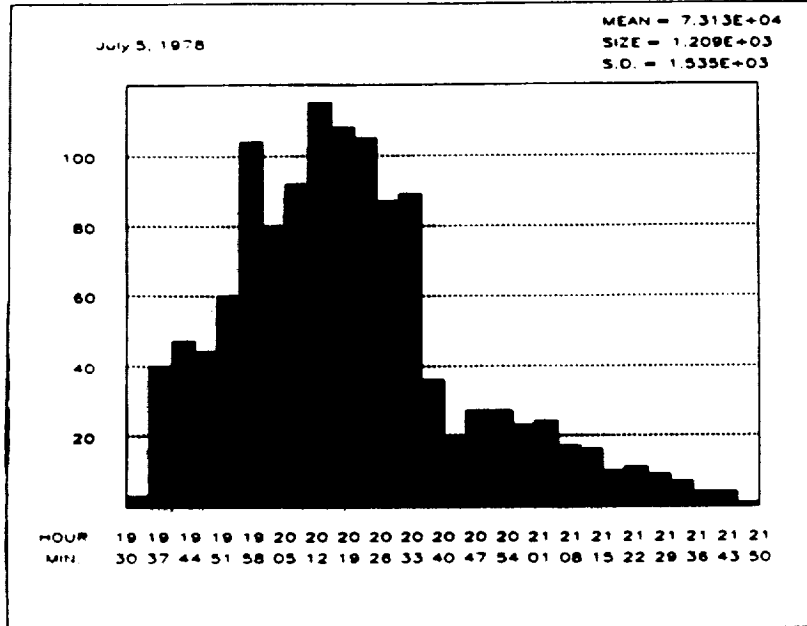


Figure 6.1 Five minute flashing rate histograms for July 5 and July 6, 1978.

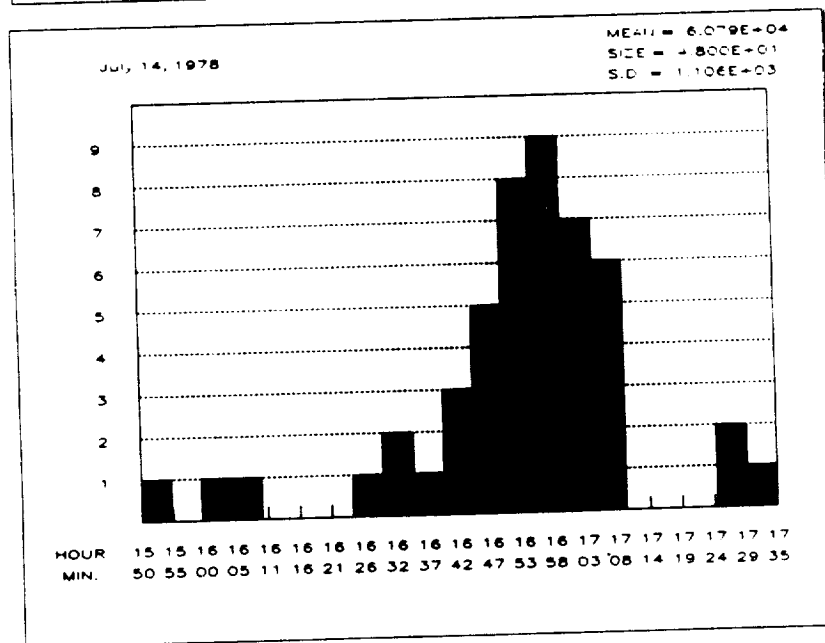
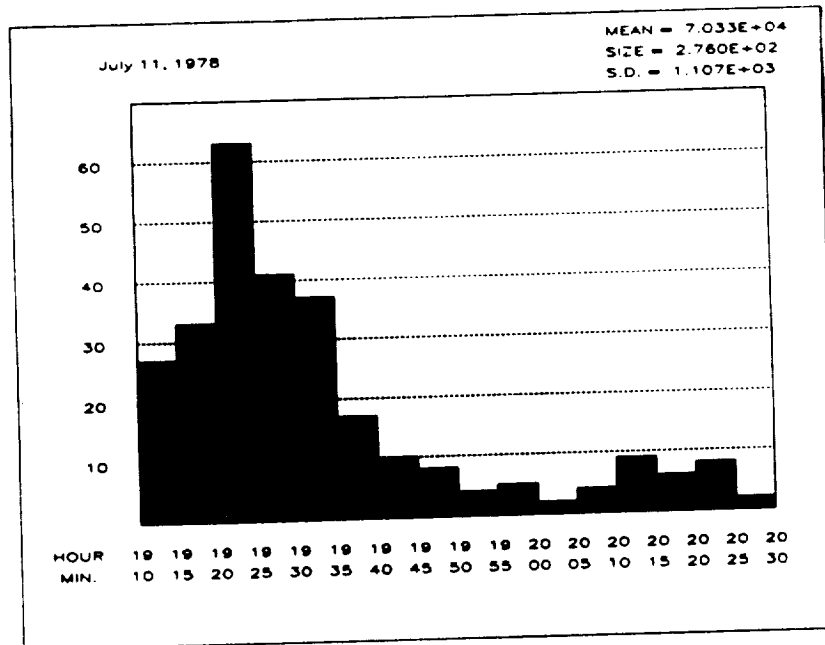


Figure 6.2 Five minute flashing rate histograms for July 11 and July 14, 1978.

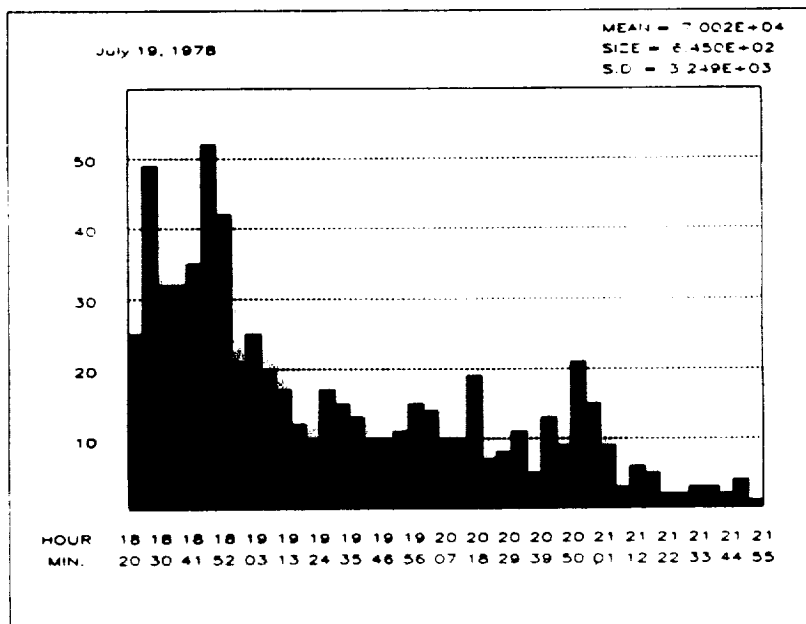
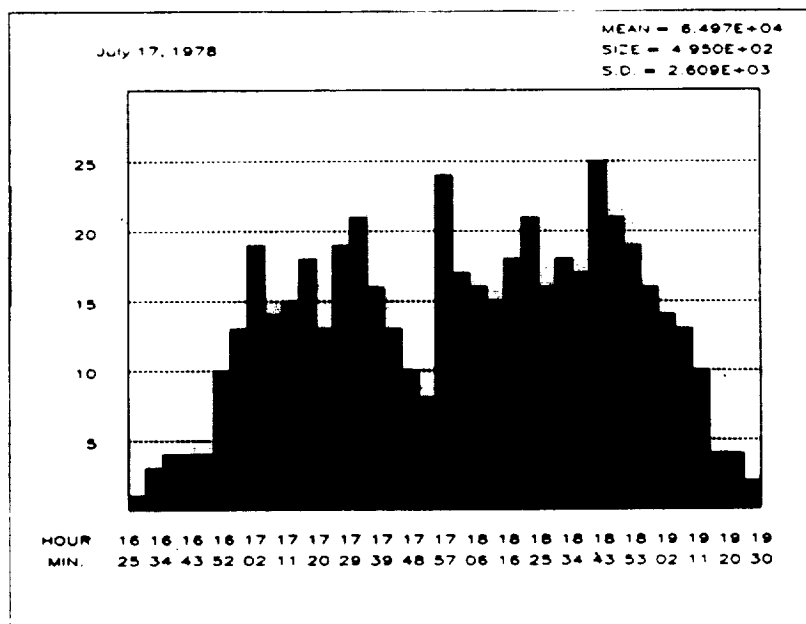


Figure 6.3 Five minute flashing rate histograms for July 17 and July 19, 1978.

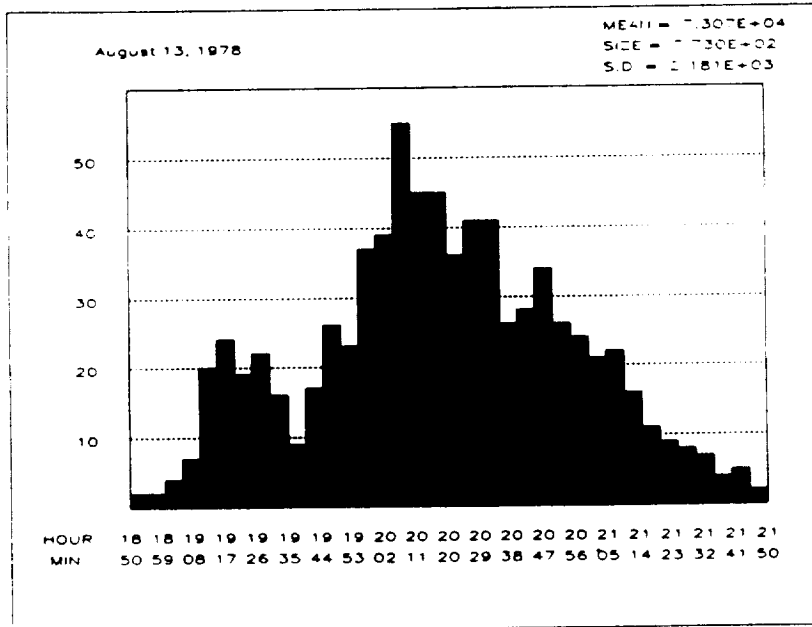
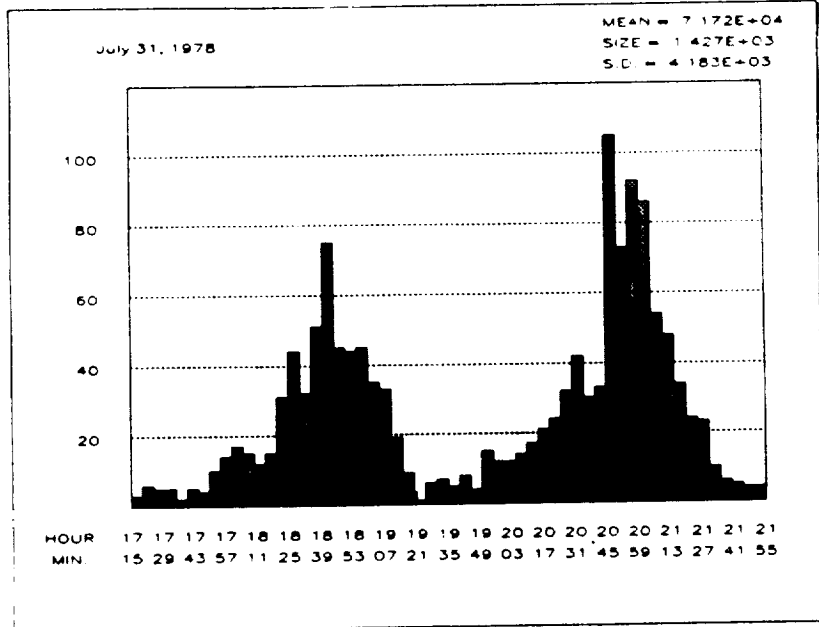


Figure 6.4 Five minute flashing rate histograms for July 31 and August 13, 1978.

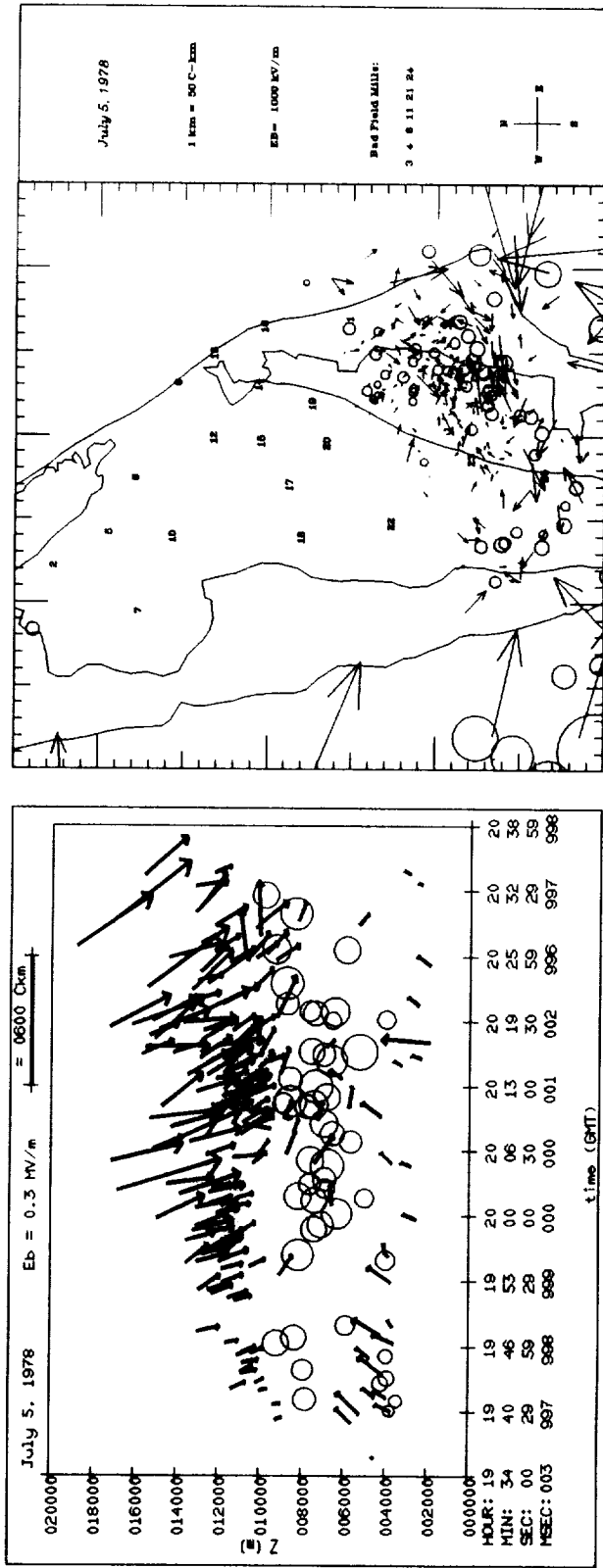


Figure 6.5 Q- and P- results for storm on July 5, 1978:

Height vs. time and plan views.

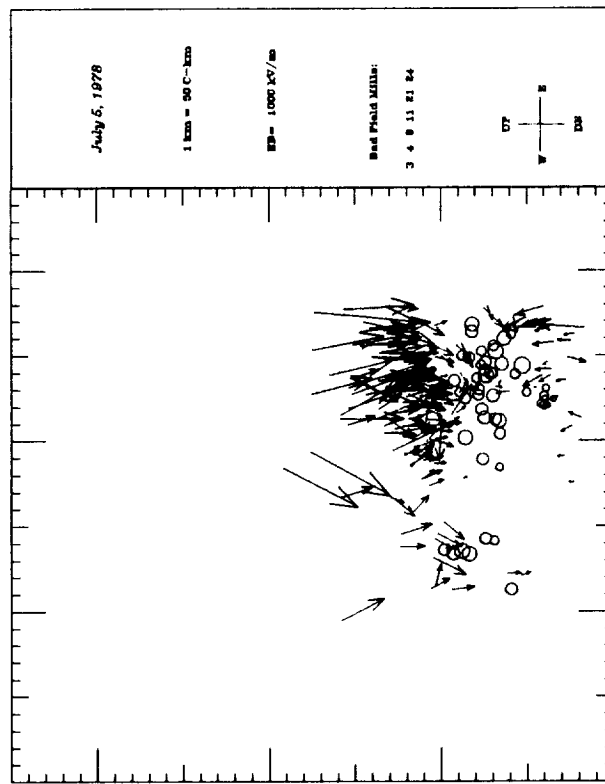
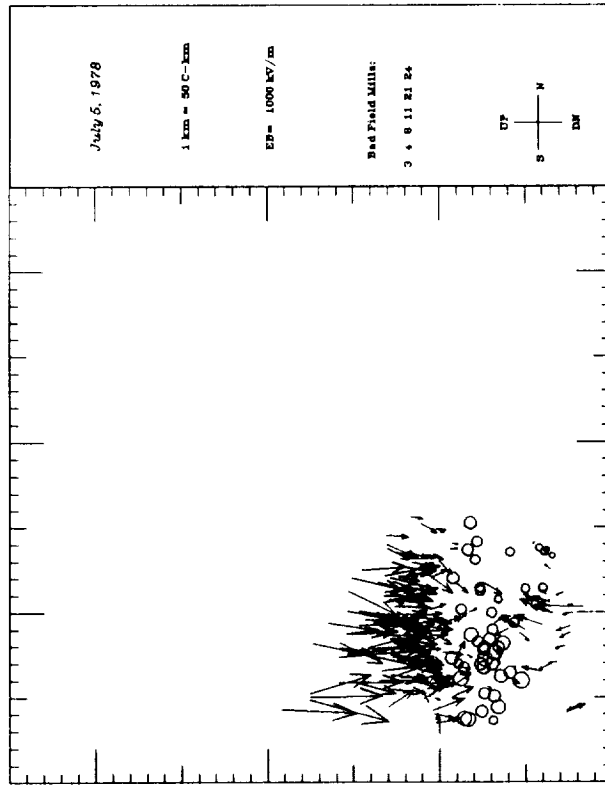


Figure 6.5 cont.
Altitude cross-section views.

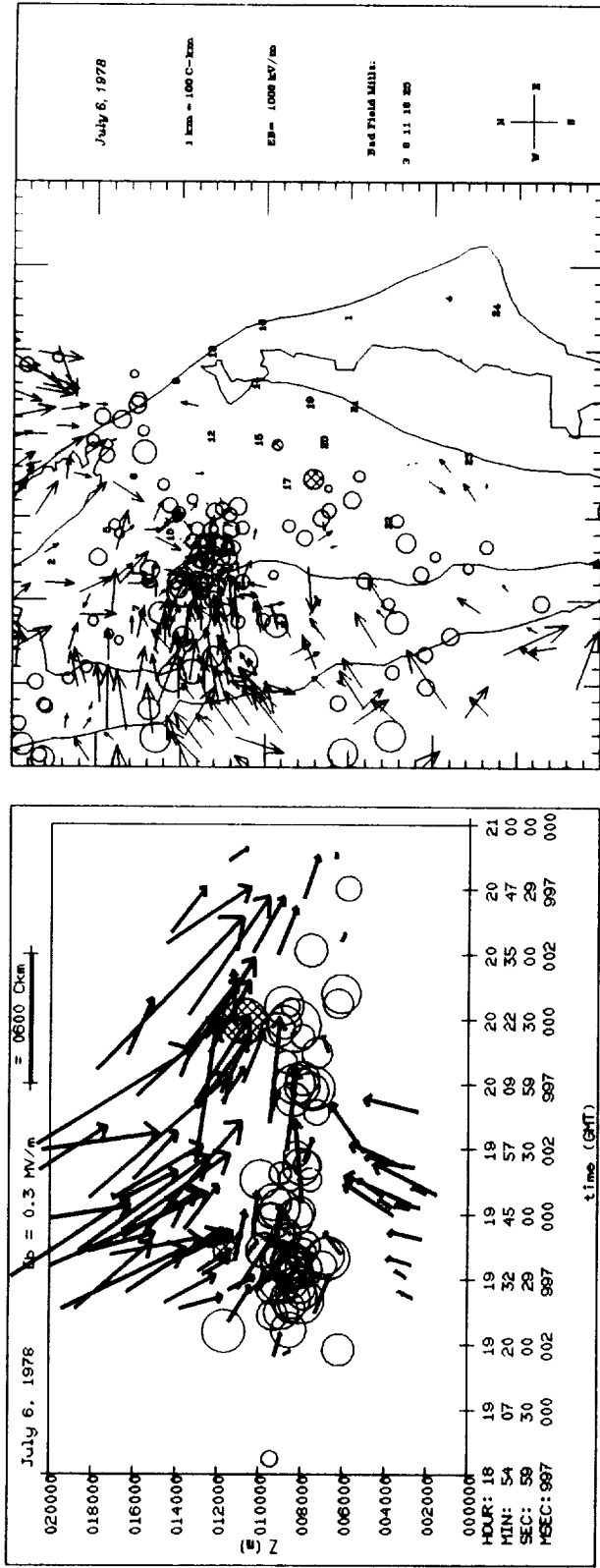


Figure 6.6 Q- and P- results for storm on July 6, 1978:
 Height vs. time and plan views.

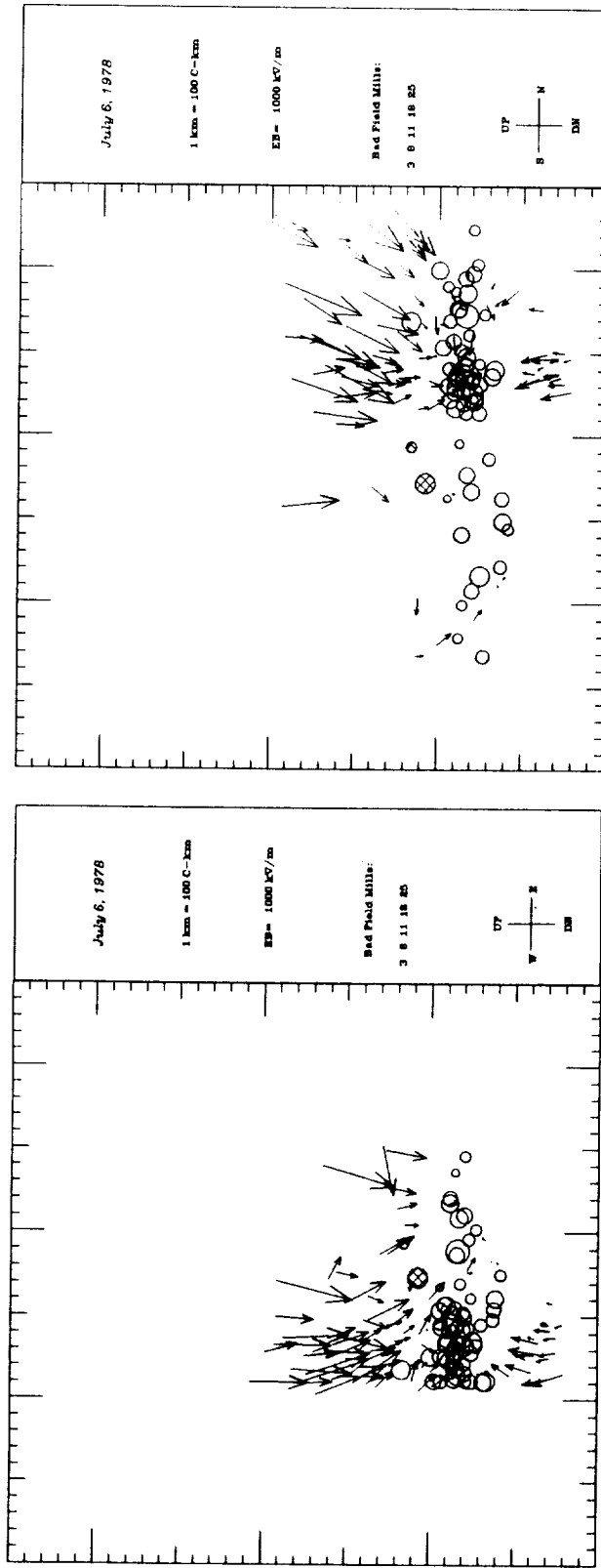


Figure 6.6 cont.
 Altitude cross-section views.

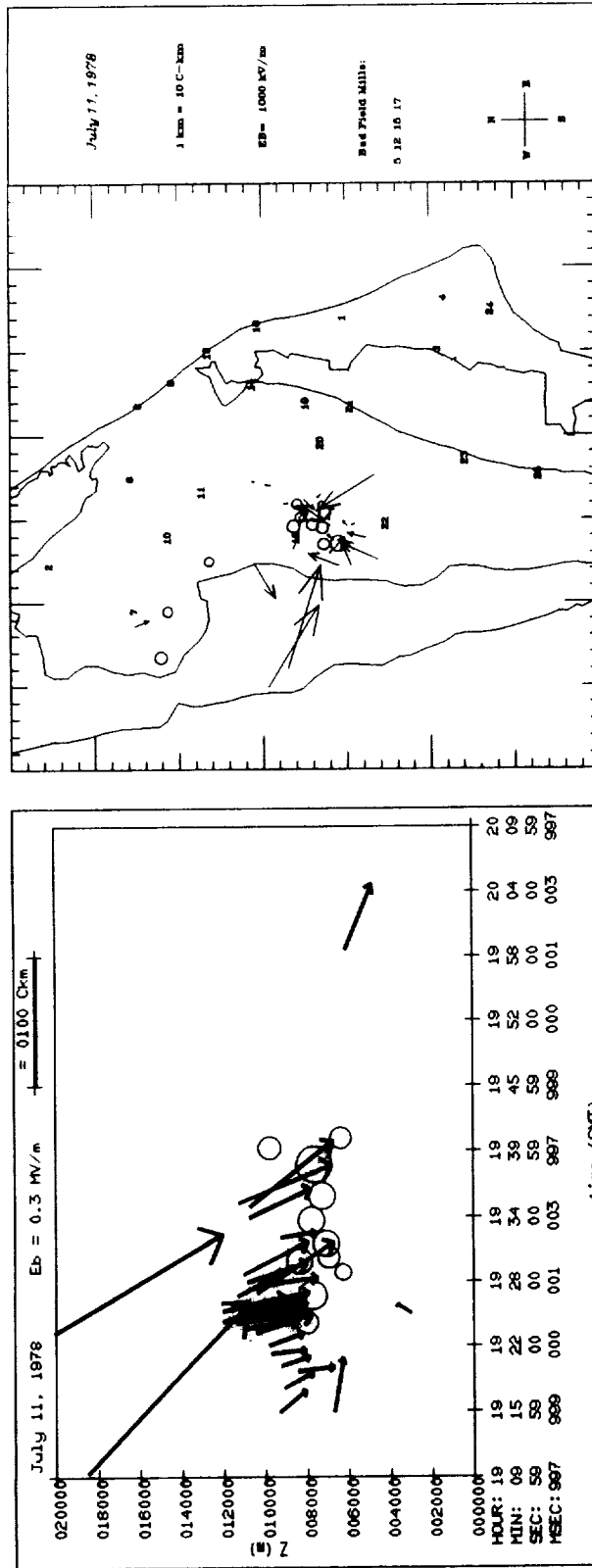


Figure 6.7 Q- and P- results for storm on July 11, 1978:
Height vs. time and plan views.

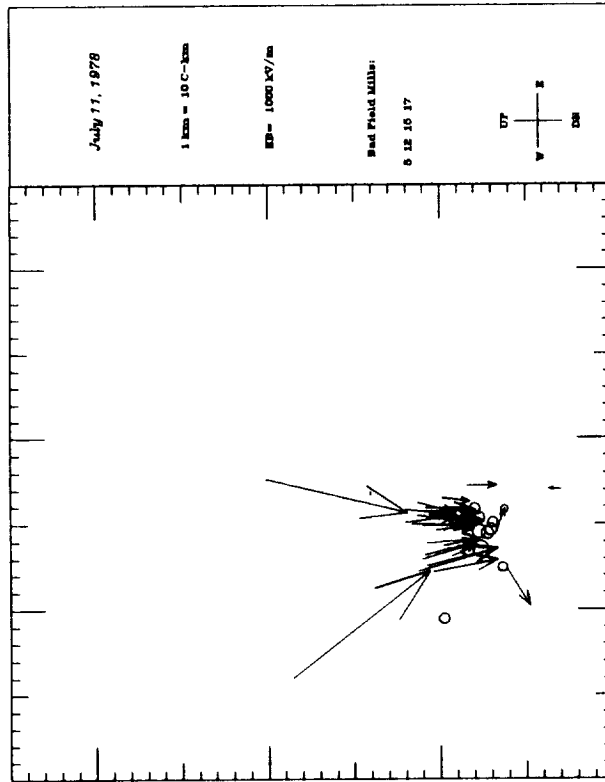
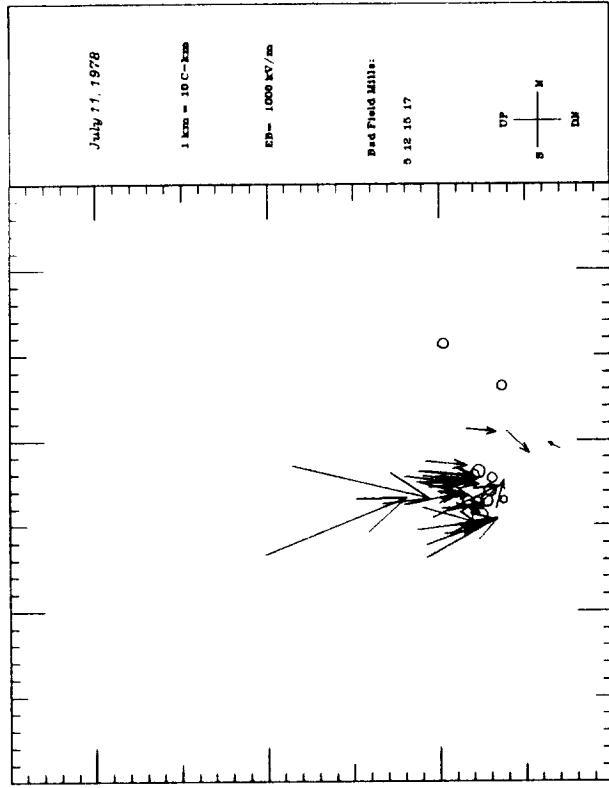


Figure 6.7 cont.
 Altitude cross-section views.

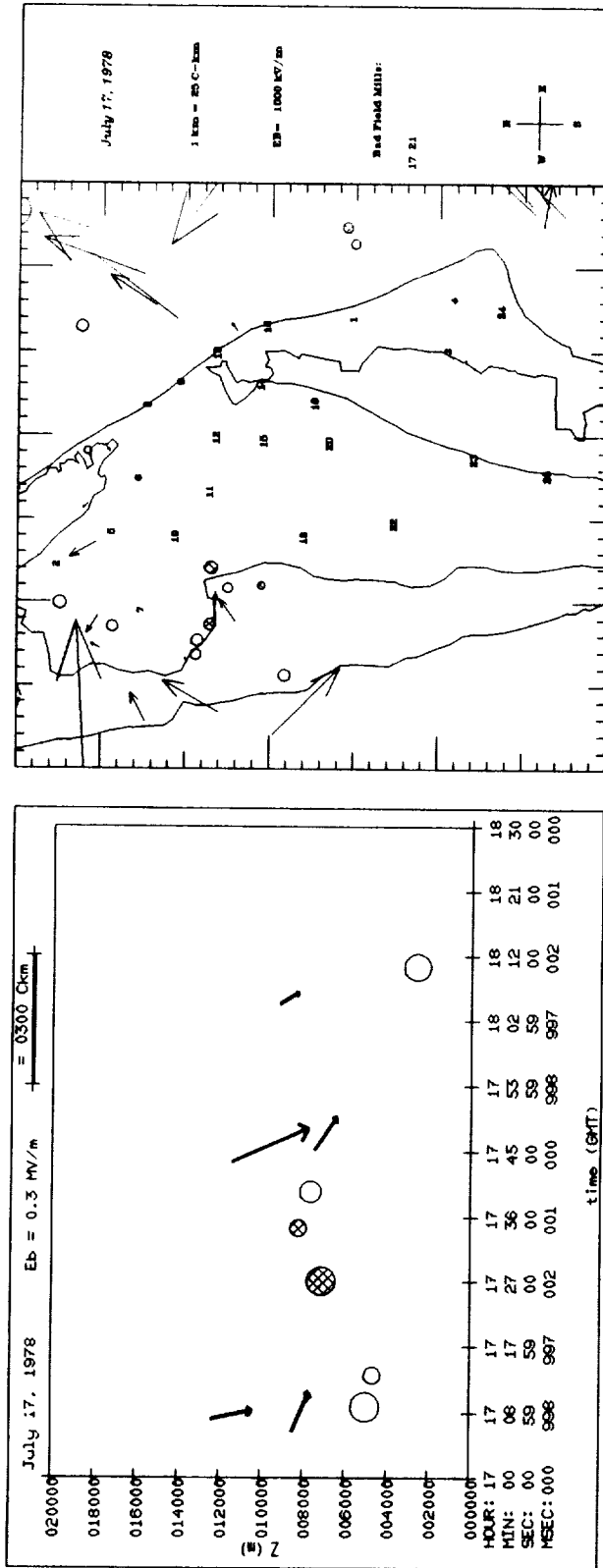


Figure 6.8 Q- and P- results for storm on July 17, 1978:
Height vs. time and plan views.

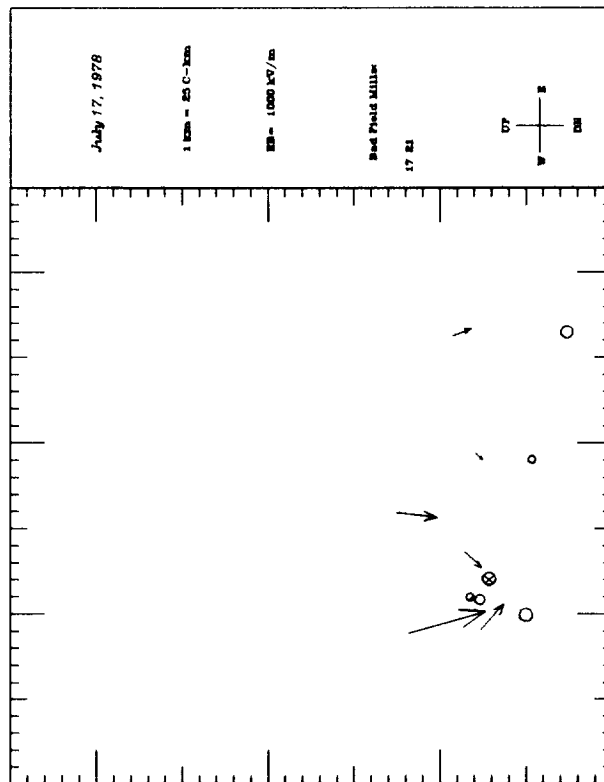
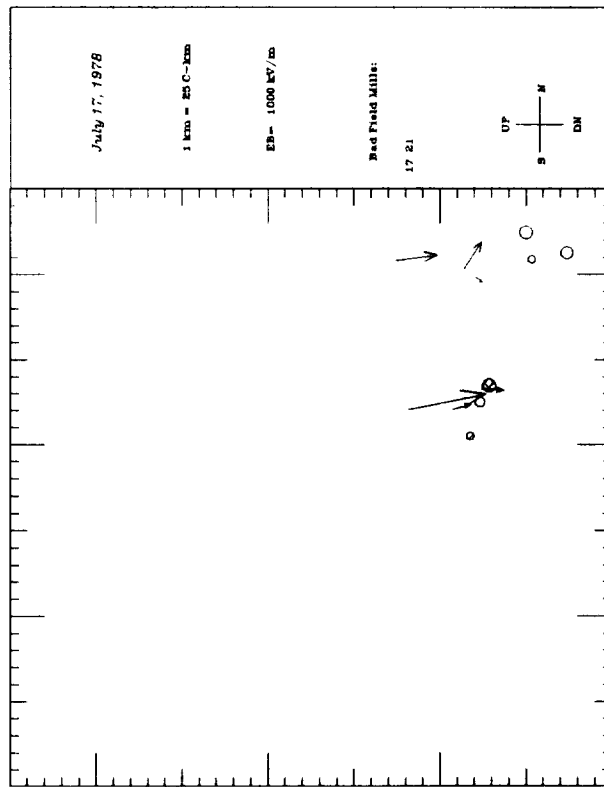


Figure 6.8 cont.

Altitude cross-section views.

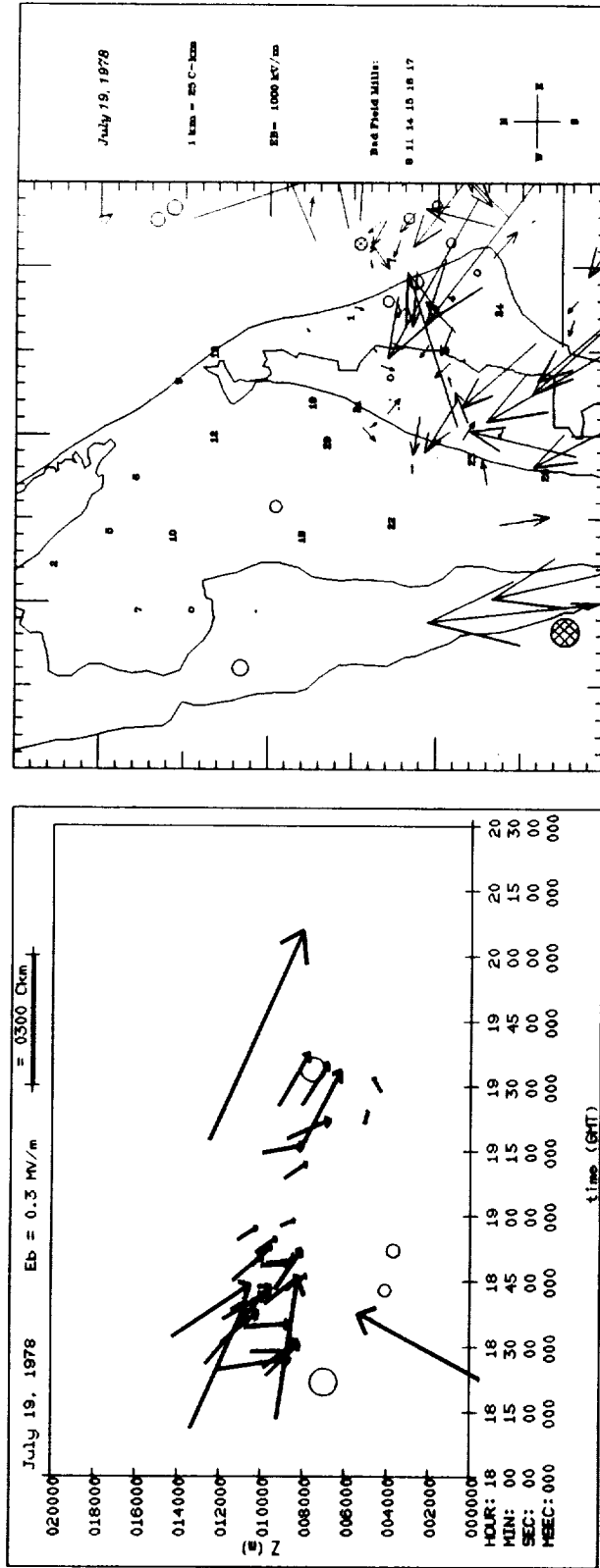


Figure 6.9 Q- and P- results for storm on July 19, 1978:
 Height vs. time and plan views.

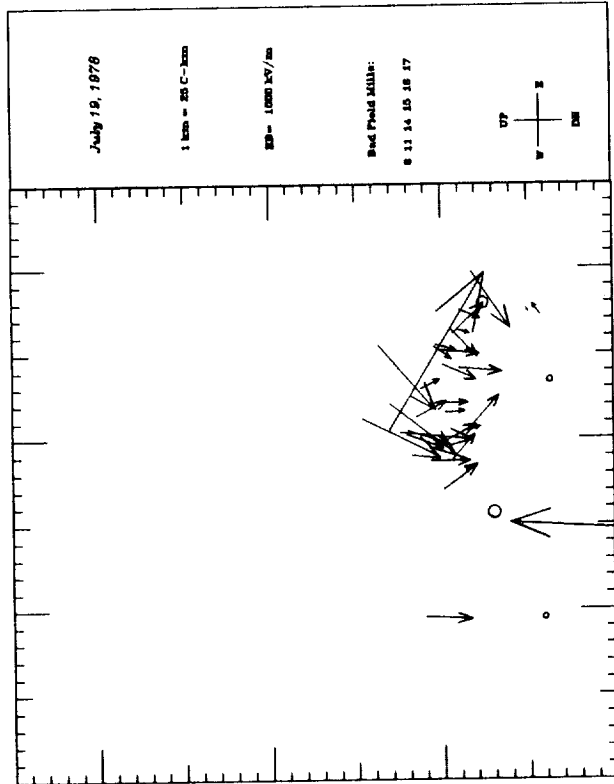
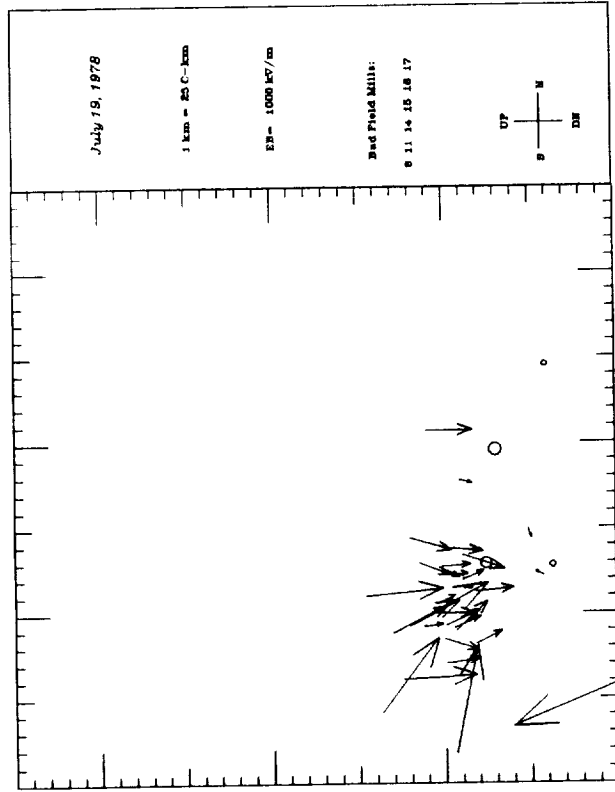


Figure 6.9 cont.
 Altitude cross-section views.

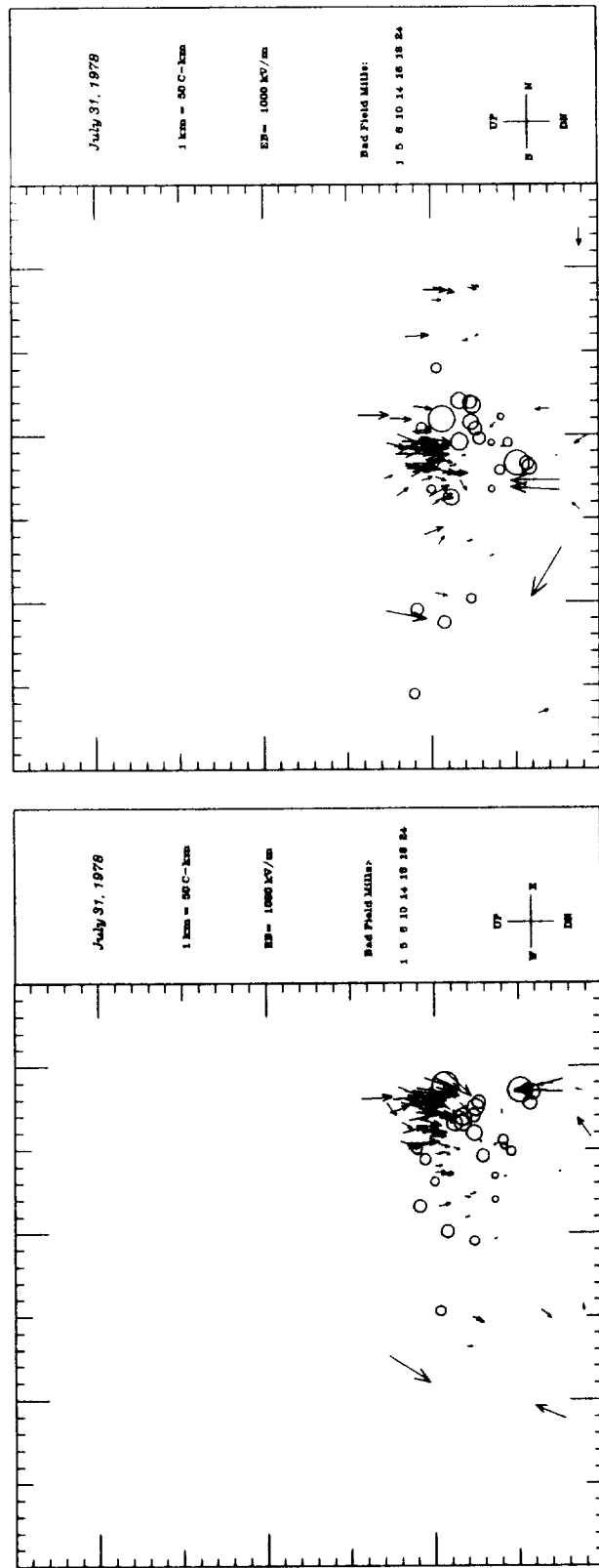


Figure 6.10 cont.
 Altitude cross-section views.

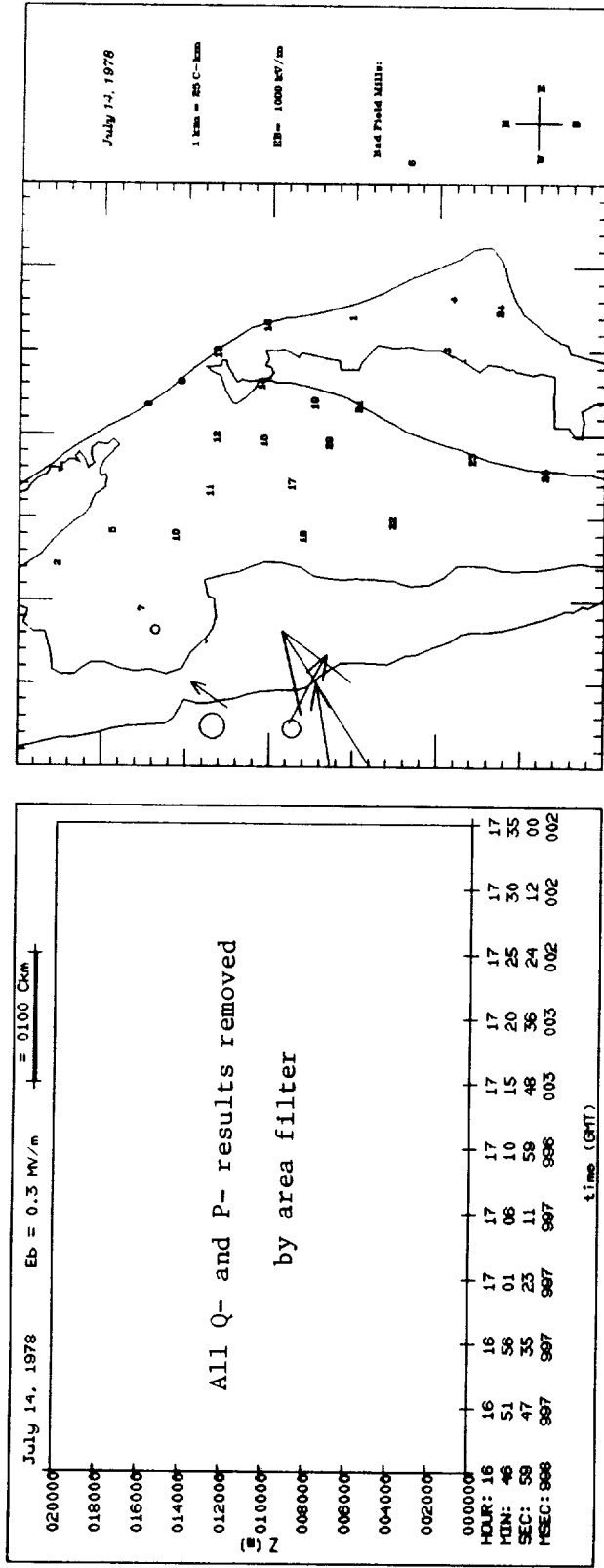


Figure 6.11 Q- and P- results for two distant storms on July 14 and August 13, 1978: Height vs. time and plan views.

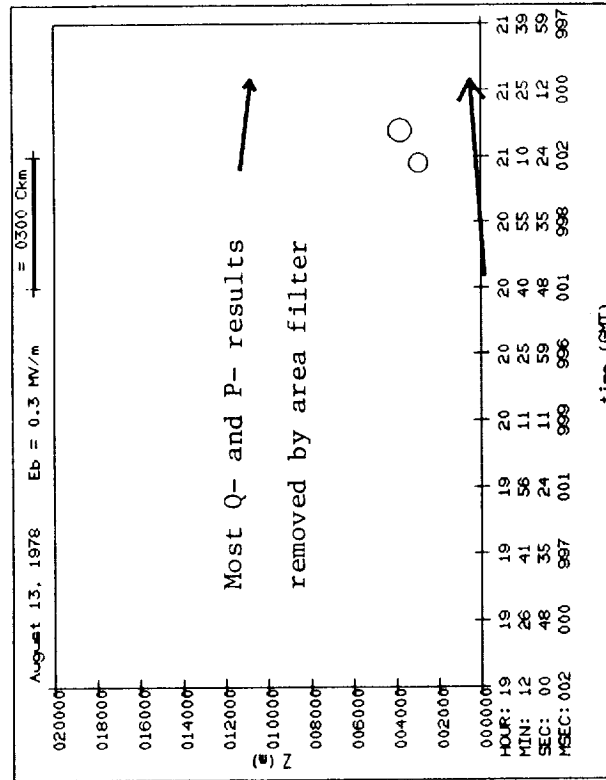
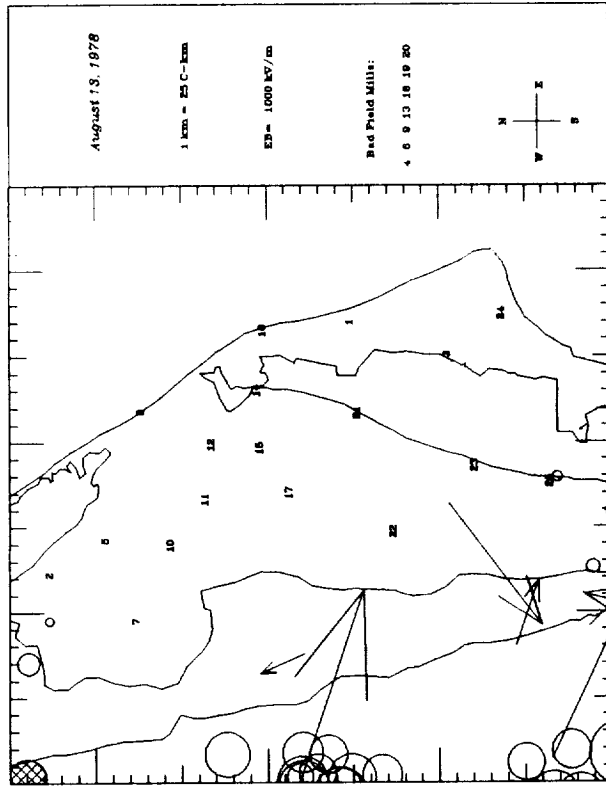


Figure 6.11 cont.

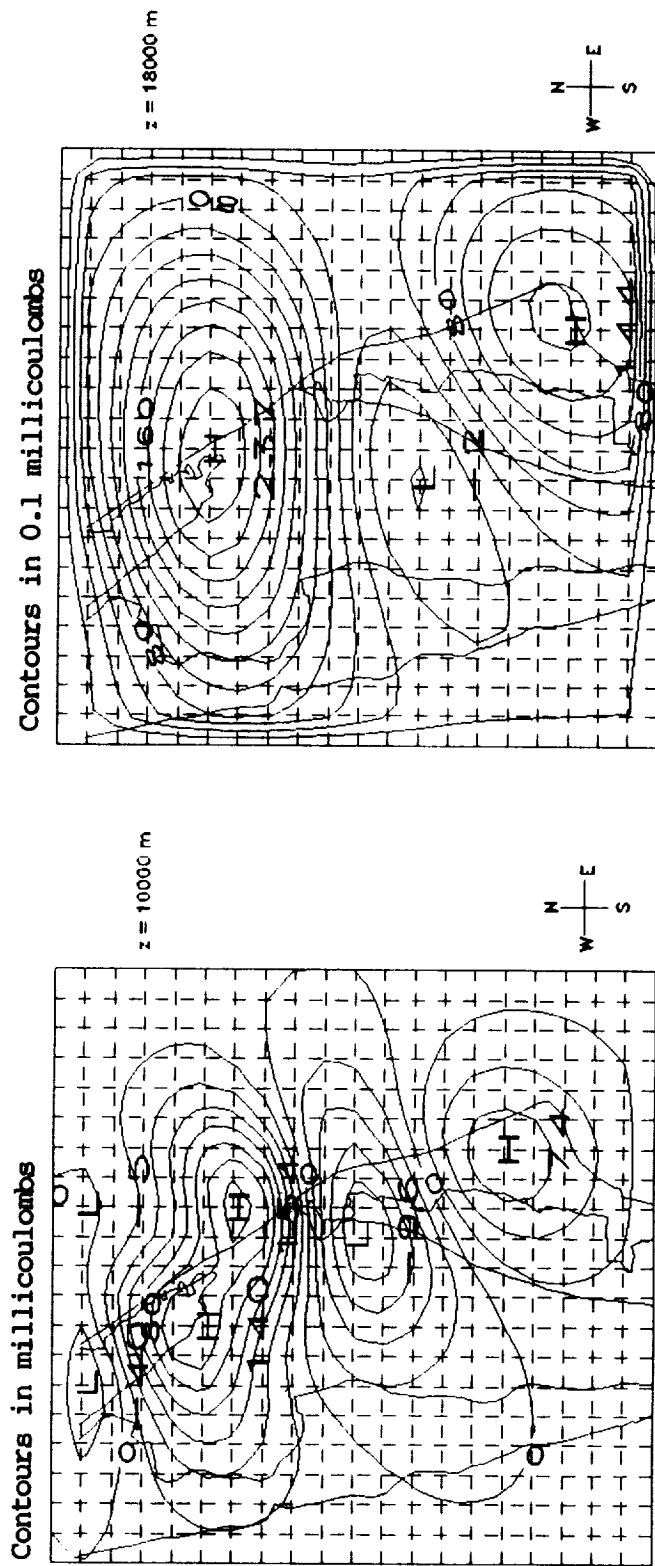


Figure 6.12a Plan views of solution for lightning flash occurring at 201521.4GMT on July 6, 1978. Kernel scaling performed.

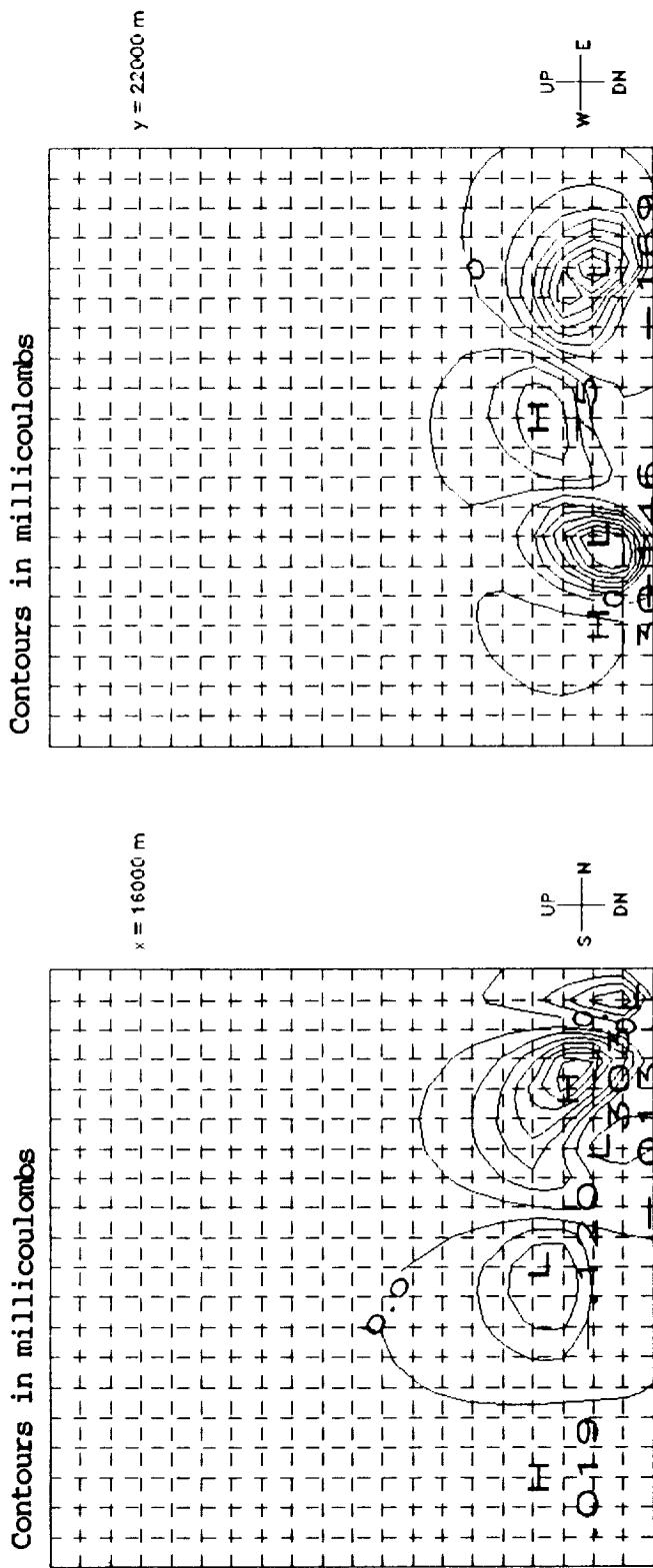


Figure 6.12b Altitude cross-sections of solution for the source described in previous figure.

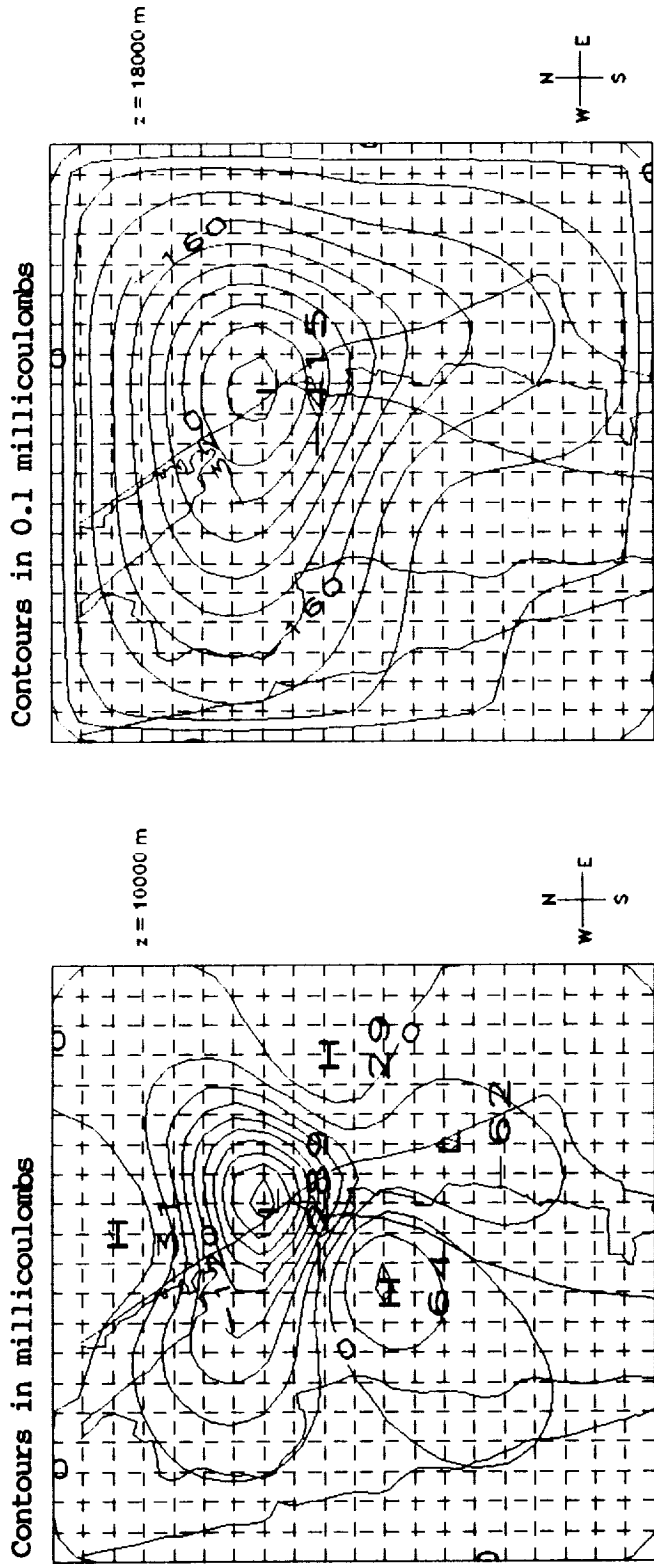


Figure 6.13a Plan views of solution for lightning flash occurring at 202210.4GMT on July 6, 1978. Kernel scaling performed.

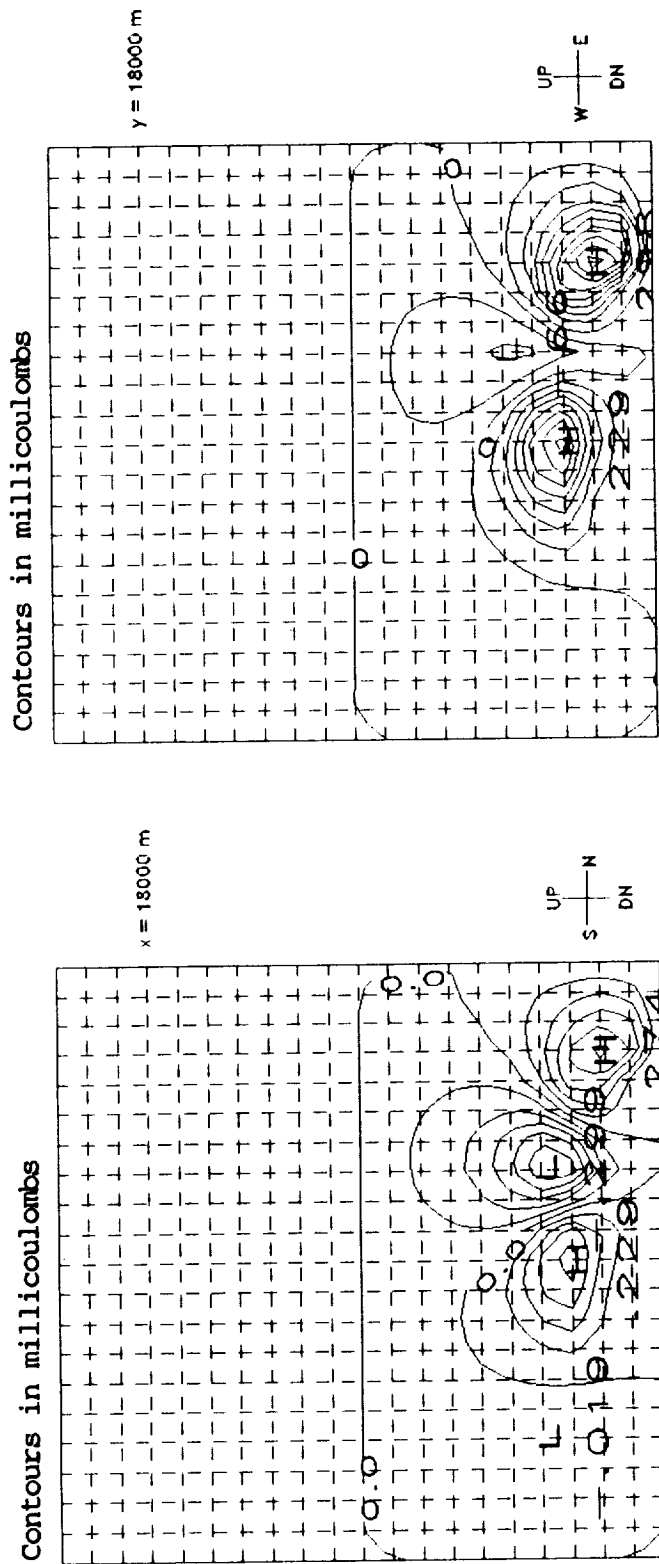


Figure 6.13b Altitude cross-sections of solution for the source described in previous figure.

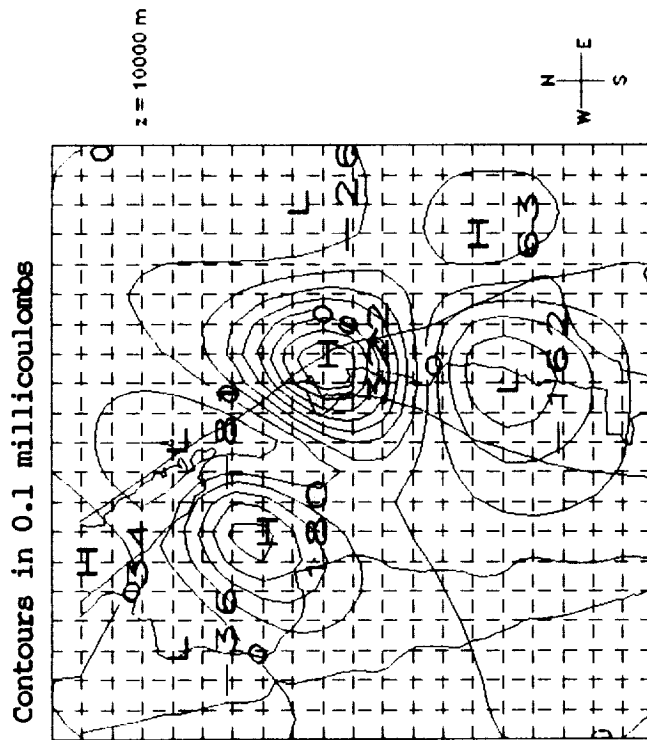
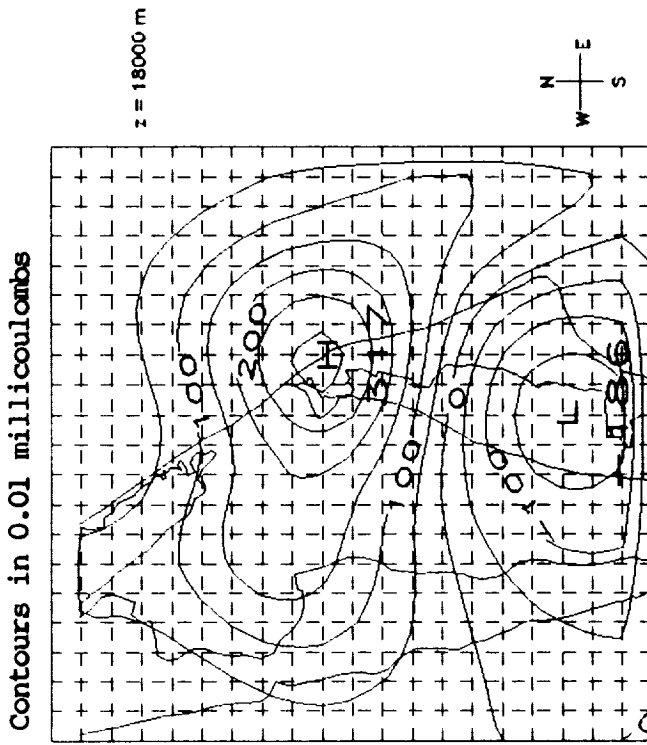


Figure 6.14a Plan views of solution for lightning flash occurring at 201611.9GMT on July 6, 1978. Kernel scaling performed.

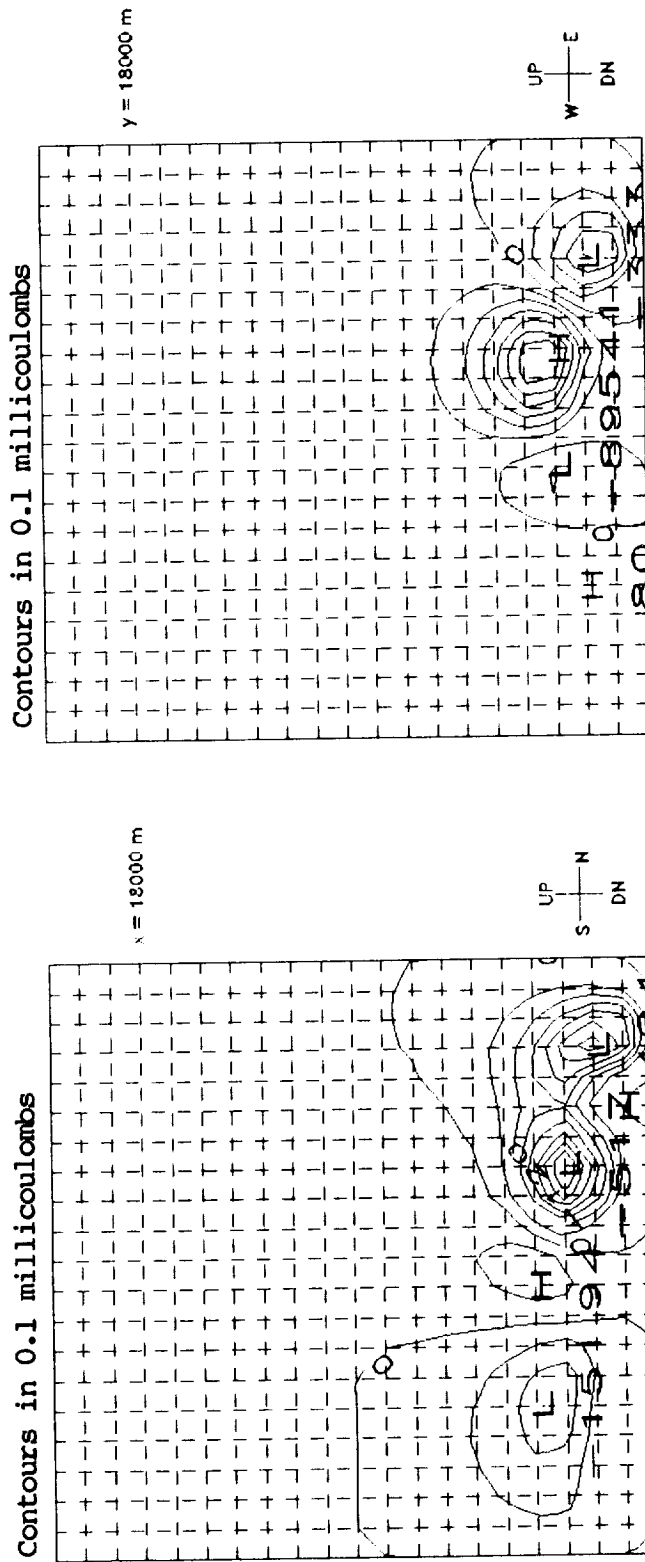


Figure 6.14b Altitude cross-sections of solution for the source described in previous figure.

TABLE 5.1 Eigenanalysis of a centrally located grid system for various grid resolutions. The center of the grid is always at $(x,y,z) = (18 \text{ km}, 18 \text{ km}, 10 \text{ km})$ and has horizontal and vertical dimensions of 40 km and 20 km, respectively. Values in the table are the scaled eigenvalues $\lambda_i^s = \lambda_i / \lambda_{\max}$. Expected solution errors \bar{s}^2 are also shown for each grid.

	Grid Resolution (km)		
	1	2	4
01	0.1000E+01	0.1000E+01	0.1000E+01
02	0.5020E+00	0.4196E+00	0.3360E+00
03	0.4167E+00	0.3177E+00	0.2157E+00
04	0.3953E+00	0.2839E+00	0.1780E+00
05	0.3130E+00	0.2024E+00	0.1107E+00
06	0.2940E+00	0.1863E+00	0.9028E-01
07	0.2633E+00	0.1463E+00	0.5914E-01
08	0.2551E+00	0.1382E+00	0.5227E-01
09	0.2388E+00	0.1227E+00	0.4419E-01
10	0.2182E+00	0.1049E+00	0.3363E-01
11	0.2153E+00	0.9591E-01	0.2876E-01
12	0.2114E+00	0.9308E-01	0.2380E-01
13	0.1912E+00	0.7782E-01	0.1900E-01
14	0.1886E+00	0.7434E-01	0.1339E-01
15	0.1805E+00	0.6560E-01	0.1307E-01
16	0.1775E+00	0.6211E-01	0.1246E-01
17	0.1718E+00	0.5945E-01	0.1088E-01
18	0.1647E+00	0.5396E-01	0.8755E-02
19	0.1570E+00	0.4834E-01	0.6600E-02
20	0.1488E+00	0.4450E-01	0.4447E-02
21	0.1476E+00	0.4049E-01	0.3157E-02
22	0.1431E+00	0.3314E-01	0.1396E-02
23	0.1298E+00	0.2949E-01	0.8359E-03
24	0.1250E+00	0.2544E-01	0.5052E-03
25	0.1175E+00	0.2005E-01	0.1398E-03
\bar{s}^2	1.274E-02	2.322E-02	4.508E-01

TABLE 5.2 Eigenanalysis of a centrally located grid system for various grid dimensions. Grid resolution is always 1 km, and the center of the grid is always at $(x,y,z) = (18 \text{ km}, 18 \text{ km}, 10 \text{ km})$. Values in the table are scaled eigenvalues $\lambda_i^s = \lambda_i / \lambda_{\max}$. Expected solution errors \bar{s}^2 are also shown for each grid.

Cubical Grid Dimension (km)				
	5	10	15	20
01	0.1000E+01	0.1000E+01	0.1000E+01	0.1000E+01
02	0.2077E-01	0.9151E-01	0.2511E+00	0.4755E+00
03	0.1827E-01	0.8307E-01	0.2205E+00	0.4272E+00
04	0.6230E-02	0.2368E-01	0.1141E+00	0.3476E+00
05	0.8597E-03	0.1649E-01	0.1001E+00	0.3162E+00
06	0.3419E-03	0.8046E-02	0.6768E-01	0.2866E+00
07	0.3121E-03	0.4469E-02	0.5391E-01	0.2831E+00
08	0.1096E-03	0.2913E-02	0.4942E-01	0.2562E+00
09	0.8020E-04	0.2526E-02	0.3265E-01	0.2379E+00
10	0.1800E-04	0.1194E-02	0.2402E-01	0.2131E+00
11	0.1130E-04	0.9595E-03	0.1850E-01	0.2083E+00
12	0.5051E-05	0.5321E-03	0.1659E-01	0.2055E+00
13	0.3460E-05	0.3358E-03	0.1452E-01	0.1968E+00
14	0.1796E-05	0.1889E-03	0.1194E-01	0.1898E+00
15	0.7817E-06	0.1496E-03	0.1040E-01	0.1766E+00
16	0.6453E-06	0.1409E-03	0.8702E-02	0.1723E+00
17	0.3875E-06	0.9240E-04	0.7818E-02	0.1661E+00
18	0.1669E-06	0.4667E-04	0.6484E-02	0.1624E+00
19	0.7287E-07	0.3211E-04	0.3769E-02	0.1495E+00
20	0.5334E-07	0.1779E-04	0.1864E-02	0.1438E+00
21	0.2123E-07	0.1418E-04	0.1034E-02	0.1318E+00
22	0.7835E-08	0.5724E-05	0.5089E-03	0.2064E-01
23	0.1590E-08	0.2085E-05	0.4213E-03	0.1477E-01
24	0.1014E-08	0.4923E-06	0.7132E-04	0.3763E-02
25	0.4784E-09	0.4269E-06	0.4786E-04	0.1447E-02
\bar{s}^2	6.576E+04	1.038E+02	1.353E+00	1.083E-01

TABLE 5.3 Eigenanalysis of a small cubical grid system (dimension 10 km, resolution 1 km) for various distances from the measuring network. Center of grid is always at an altitude of 8 km. Values in table are scaled eigenvalues $\lambda_i^s = \lambda_i / \lambda_{\max}$. For very illconditioned cases (i.e., when grid is well off network), the smallest eigenvalues could not be accurately computed and hence have been omitted below. Expected solution errors are given only for those cases where all eigenvalues have been found.

	(x,y) Location of Grid System Center (km)				
	(18,18)	(25,25)	(32,32)	(39,39)	(46,46)
01	0.1000E+01	0.1000E+01	0.1000E+01	0.1000E+01	0.1000E+01
02	0.1722E+00	0.1755E+00	0.2592E-01	0.3983E-02	0.1568E-02
03	0.1579E+00	0.1101E+00	0.1648E-01	0.3402E-02	0.9226E-03
04	0.5838E-01	0.4331E-01	0.1041E-02	0.5126E-04	0.5855E-05
05	0.4414E-01	0.2228E-01	0.7562E-03	0.2580E-04	0.2104E-05
06	0.3520E-01	0.1712E-01	0.5174E-03	0.8809E-05	0.8335E-06
07	0.1683E-01	0.1226E-01	0.3351E-04	0.2689E-06	0.1340E-07
08	0.1531E-01	0.8082E-02	0.2154E-04	0.1872E-06	0.4766E-08
09	0.1208E-01	0.3632E-02	0.1199E-04	0.8320E-07	0.3026E-08
10	0.7505E-02	0.1443E-02	0.7062E-05	0.3800E-07	0.7670E-09
11	0.5937E-02	0.1155E-02	0.1165E-05	0.2435E-08	0.3181E-09
12	0.4458E-02	0.4851E-03	0.4494E-06	0.1141E-08	0.1529E-09
13	0.2549E-02	0.3170E-03	0.1896E-06	0.3151E-09	0.1284E-09
14	0.1383E-02	0.1274E-03	0.6925E-07	0.2504E-09	0.1057E-09
15	0.8865E-03	0.4511E-04	0.5212E-07	0.1770E-09	0.7397E-10
16	0.4913E-03	0.2804E-04	0.1095E-07	0.1245E-09	0.4279E-10
17	0.2685E-03	0.1552E-04	0.7298E-08	0.7937E-10	0.2903E-10
18	0.1475E-03	0.1005E-04	0.1469E-08	0.3725E-10	0.1361E-10
19	0.1216E-03	0.6217E-05	0.4730E-09	0.9219E-11	0.1948E-11
20	0.7002E-04	0.2158E-05	0.3384E-09	0.2854E-11	
21	0.2824E-04	0.6079E-06	0.1263E-09		
22	0.1492E-04	0.3107E-06	0.6439E-10		
23	0.1004E-04	0.1649E-06	0.2914E-10		
24	0.1102E-05	0.1743E-07	0.8911E-11		
25	0.6529E-06	0.5484E-08			
\bar{s}^2	0.6583E+04	0.5617E+06			

TABLE 5.4 Eigenanalyses of five different field mill networks: (1) a small square network of area 5.76 km², (2) the 1978 KSC network, (3) the 1987 KSC network, (4) the 1991 KSC network, and (5) a large square network of area 1024 km². The U.H.S. grid has 2 km resolution with x and y ranging from -2 to 38 km, and z from 0 to 20 km. Expected solution errors ξ^2 are shown for each network.

	Small Area Network	KSC Network (1978)	KSC Network (1987)	KSC Network (1991)	Large Area Network
01	0.1000E+01	0.1000E+01	0.1000E+01	0.1000E+01	0.1000E+01
02	0.6410E-01	0.4196E+00	0.5277E+00	0.5202E+00	0.5492E+00
03	0.6393E-01	0.3177E+00	0.3702E+00	0.3587E+00	0.5492E+00
04	0.9410E-02	0.2839E+00	0.2946E+00	0.2844E+00	0.4022E+00
05	0.7557E-02	0.2024E+00	0.2309E+00	0.2065E+00	0.3559E+00
06	0.6190E-02	0.1863E+00	0.2154E+00	0.1914E+00	0.3517E+00
07	0.1251E-02	0.1463E+00	0.1661E+00	0.1608E+00	0.2999E+00
08	0.1086E-02	0.1382E+00	0.1491E+00	0.1454E+00	0.2999E+00
09	0.2477E-03	0.1227E+00	0.1341E+00	0.1320E+00	0.2627E+00
10	0.1864E-04	0.1049E+00	0.1229E+00	0.1155E+00	0.2627E+00
11	0.1784E-04	0.9591E-01	0.1056E+00	0.1122E+00	0.2501E+00
12	0.3274E-05	0.9308E-01	0.9682E-01	0.9389E-01	0.2403E+00
13	0.1376E-05	0.7782E-01	0.8085E-01	0.8822E-01	0.2394E+00
14	0.9867E-06	0.7434E-01	0.7964E-01	0.8275E-01	0.2211E+00
15	0.8476E-06	0.6560E-01	0.7535E-01	0.7984E-01	0.2209E+00
16	0.3069E-06	0.6211E-01	0.7320E-01	0.7717E-01	0.2146E+00
17	0.2147E-06	0.5945E-01	0.6987E-01	0.7129E-01	0.2146E+00
18	0.1027E-06	0.5396E-01	0.6355E-01	0.6755E-01	0.2090E+00
19	0.7777E-07	0.4834E-01	0.6098E-01	0.5681E-01	0.2089E+00
20	0.2496E-07	0.4450E-01	0.5150E-01	0.5503E-01	0.1943E+00
21	0.1040E-07	0.4049E-01	0.4938E-01	0.5153E-01	0.1941E+00
22	0.9157E-08	0.3314E-01	0.4794E-01	0.4444E-01	0.1940E+00
23	0.1842E-08	0.2949E-01	0.4315E-01	0.4275E-01	0.1810E+00
24	0.8621E-09	0.2544E-01	0.3677E-01	0.3759E-01	0.1809E+00
25	0.8080E-09	0.2005E-01	0.3417E-01	0.3475E-01	0.1721E+00
26			0.3252E-01	0.3189E-01	
27			0.2837E-01	0.3045E-01	
28			0.2527E-01	0.2646E-01	
29			0.2253E-01	0.2330E-01	
30			0.1812E-01	0.1838E-01	
31			0.1667E-01	0.1702E-01	
32			0.1173E-01		
33			0.9806E-02		
34			0.8838E-03		
ξ^2	5.944E+04	2.322E-02	7.099E-02	2.483E-02	1.191E-02

TABLE 5.5 Summary of solution error for various lightning source geometries and locations. The effects of measurement error and constraints are tested. Note that solution charge errors are large, but that centroid errors are usually within the grid resolution (≈ 2 km).*

FIGURE	ADDED CONSTRAINTS	MEASUREMENT ERROR	RMS RELATIVE RESIDUAL	SOLUTION ERROR						
				ΔX (km)	ΔY (km)	ΔZ (km)	ΔD (km)	ΔR (km)	ΔQ (C)	
5.1	NO	NO	1.2×10^{-5}	-0.18	-0.04	1.17	0.19	1.19	10.2	
5.2	SCALING	NO	4.2×10^{-3}	-0.09	-0.20	1.68	0.22	1.70	14.3	
5.3	SCALING	YES	7.6×10^{-3}	0.05	0.16	1.60	0.17	1.61	13.0	
5.4	SCALING	YES	8.1×10^{-3}	-1.36	0.33	-1.13	1.40	1.80	14.1	
5.5	SCALING	YES	1.5×10^{-2}	-0.11	-0.06	0.30	0.12	0.33	6.5	
5.6	SCALING	YES	1.0×10^{-2}	0.31	0.14	-1.46	0.35	1.50	9.6	
5.7	SCALING	YES	1.0×10^{-2}	0.06	0.99	-1.14	0.99	1.51	1.0	
5.8	SCALING + MAX P	YES	1.3×10^{-1}	0.72	0.55	2.12	0.90	2.30	-0.1	
5.9	SMOOTHING	YES	2.4×10^{-2}	-1.18	-0.40	1.41	1.24	1.88	18.0	
5.10	SCALING + CONS. OF CHARGE	YES	8.5×10^{-2}	0.81	0.03	0.52	0.81	0.96	-0.1	
5.11	NO	YES	5.84×10^{-5}	-6.25	-0.65	0.87	6.29	6.35	-14.1	
5.12	SCALING	YES	6.25×10^{-3}	-3.34	-0.18	0.67	3.35	3.41	1.2	
5.13	SCALING	YES	2.12×10^{-3}	-1.34	2.26	0.63	2.62	2.70	19.1	
5.14	SCALING	YES	4.86×10^{-3}	6.66	1.48	1.01	6.82	6.89	-16.7	
5.15	SCALING	YES	3.66×10^{-3}	-0.24	-3.10	1.02	3.10	3.27	7.4	

* Values of ΔX , ΔY , and ΔZ represent spatial errors between the known centroid and the centroid of the distribution $|f_j|$, i.e., $\Delta X \equiv X_{\text{retrieved}} - X_{\text{true}}$; $\Delta D^2 \equiv \Delta X^2 + \Delta Y^2$; $\Delta R^2 \equiv \Delta X^2 + \Delta Y^2 + \Delta Z^2$; and $\Delta Q \equiv (\sum f_j - \text{actual charge})$.

TABLE 6.1 The total number of flashes identified during each storm period (N_T), the number of flashes with $\Delta E \geq 1$ kV/m at 2 or more sites (N_L), the number of acceptable solutions obtained with a Q- or P- model (N), and the number of these solutions within the region of optimum accuracy (N_0).

	COL. 1	COL. 2	COL. 3	COL. 4						
Date	Number of (N_T) Flashes	Number (N_L) From Col. 1 that have $\Delta E \geq 1$ kV/m at ≥ 2 Sites	Number (N) From Col. 2 that have $C_T^2 < 10$	Number (N_0) From Col. 2 Not Removed By Area Filter						
	N_T	N_L	N_P	N_0						
		N_L/N_T	N_Q	N_{OP}						
			N	N_{0g}						
			N/N_L	N_0/N						
				N_0/M_L						
07-05-78	1209	818	76	235	311	48	194	242	78%	30%
07-06-78	1013	612	116	275	391	67	90	157	40%	26%
07-11-78	276	52	12	34	46	11	32	43	93%	83%
07-14-78	48	8	3	5	8	0	0	0	0%	0%
07-17-78	495	169	15	39	54	6	6	12	22%	7%
07-19-78	645	456	21	74	95	4	32	36	38%	8%
07-31-78	1427	990	45	138	183	24	76	100	55%	10%
08-13-78	773	105	34	12	46	2	2	4	9%	4%

TABLE 6.2 Summary of the Q- and P-model parameters derived using the Chi-square minimization procedure. Symbol definitions are: N_0 [total number of optimum solutions], \bar{Q} [mean point-charge magnitudes], \bar{P} [mean point-dipole magnitudes], \bar{Z} [mean altitude of point charge (\bar{Z}_0) or point-dipole (\bar{Z}_p)], and $\bar{\theta}$ [mean polar angle of point-dipole vector]. Standard deviations appear in parentheses.

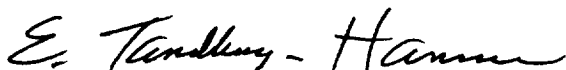
Date	N_0	N_{0q}	\bar{Q} (C)	\bar{Z}_0 (Km)	N_{0p}	\bar{P} (CKm)	\bar{Z}_p (Km)	$\bar{\theta}$ (Deg)	Altitude Interval (Km)
07-05-78	242	48	11.7 (5.2)	6.9 (1.6)	194	165.7 (103.4)	10.2 (3.1)	136.7 (47.0)	> 0
						194.5 (108.3)	11.8 (1.4)	157.0 (19.8)	> 10
						110.6 (52.8)	8.9 (1.1)	136.8 (28.5)	6 - 10
				29	97.0 (56.7)	4.0 (1.1)	44.1 (40.6)	0 - 6	
07-06-78	157	67	19.7 (12.0)	8.4 (1.1)	90	353.1 (250.3)	10.4 (4.4)	111.2 (52.0)	> 0
						510.0 (250.6)	14.0 (2.2)	146.4 (18.0)	> 11
						196.0 (114.1)	8.9 (1.5)	113.6 (26.0)	6 - 11
				18	196.2 (123.2)	3.7 (0.9)	19.5 (10.5)	0 - 6	
07-11-78	43	11	12.1 (4.9)	7.6 (1.0)	32	60.8 (40.0)	9.2 (2.2)	157.2 (28.8)	> 0
						64.1 (41.4)	9.7 (1.7)	164.7 (9.2)	> 8
						39.2 (5.2)	7.0 (0.8)	138.2 (50.5)	6 - 8
				2	36.4 (29.7)	4.4 (1.5)	72.2 (64.8)	0 - 6	
07-17-78	12	6	3.7 (12.1)	5.9 (2.2)	6	109.1 (71.2)	8.7 (1.6)	145.9 (19.4)	> 0
						131.3 (75.2)	9.4 (1.4)	151.4 (22.3)	> 8
						64.8 (49.5)	7.3 (0.6)	134.8 (4.7)	6 - 8
				0				0 - 6	
07-19-78	36	4	7.9 (5.7)	5.6 (2.0)	32	149.7 (118.1)	9.0 (2.1)	139.8 (33.7)	> 0
						148.8 (117.2)	9.7 (1.1)	149.1 (19.9)	> 8
						151.6 (40.9)	7.4 (0.3)	137.6 (20.5)	6 - 8
				3	155.0 (206.8)	4.0 (1.4)	61.0 (41.9)	0 - 6	
07-31-78	100	24	18.9 (15.6)	7.7 (2.0)	76	120.0 (76.8)	8.9 (2.7)	141.2 (43.9)	> 0
						132.4 (63.7)	10.3 (1.0)	159.6 (12.5)	> 8.5
						45.1 (15.4)	7.6 (0.7)	140.0 (35.0)	6 - 8.5
				11	134.3 (123.3)	3.2 (1.7)	52.3 (43.5)	0 - 6	

APPROVAL

ANALYSIS OF LIGHTNING FIELD CHANGES
PRODUCED BY FLORIDA THUNDERSTORMS

By William John Koshak

The information in this report has been reviewed for technical content. Review of any information concerning Department of Defense or nuclear energy activities or programs has been made by the MSFC Security Classification Officer. This report, in its entirety, has been determined to be unclassified.



E. TANDBERG-HANSEN

Director

Space Science Laboratory



